MBE GROWTH OF HIGH PERFORMANCE NITRIDE DEVICES FOR ENERGY, COMMUNICATIONS, AND DEFENSE APPLICATIONS

A Dissertation

Presented to the Faculty of the Graduate School

of Cornell University

in Partial Fulfillment of the Requirements for the Degree of

Doctor of Philosophy

By

Kristopher Dan Matthews

January 2011

MBE GROWTH OF HIGH PERFORMANCE NITRIDE DEVICES FOR ENERGY, COMMUNICATIONS, AND DEFENSE APPLICATIONS

Kristopher Dan Matthews, Ph.D.

Cornell University 2011

This thesis work features the exploration of the capabilities and limitations of devices based on MBE (Molecular Beam Epitaxy) grown III-nitride materials under three principal applications: photovoltaics, high electron mobility transistors (HEMTs), and terahertz emitters. InGaN solar cells covering the deep UV to the red ranges of the solar spectrum were fabricated. The increase in indium composition in the alloys to absorb longer wavelengths resulted in considerable leakage and series resistance caused by a combination of surface electron accumulation and electrically active line defects. A combination of thermal annealing, improved ohmic contact metal selection, electrochemical anodization, and grain coarsening resulted in improved performance. Higher sheet densities and sheet current with minimal leakage was obtained in an AlGaN/GaN HEMT by optimizing the design to include a GaN cap as a tunneling barrier and an AlN interbarrier to increase 2DEG confinement. Furthermore, a novel technique using a 325 nm, surface sensitive laser to perform micro-Raman thermal mapping on HEMTs was developed. The technique utilized higher order A_1(LO) phonons for higher thermal sensitivity. Lastly, progress was made toward GaN THz emitter development by achieving low series resistance operation through improved metal contact selection and ultra high Ge donor doping via MBE.

BIOGRAPHICAL SKETCH

I was born in Southern California in 1985 to a Thai mother and an American father. My father's sense of adventure while working for the U.S. government as a communications engineer led to my upbringing in multiple countries. Throughout my childhood I had the opportunity to live in Saudi Arabia, Thailand, Germany, and Japan. The frequent travels taught me a lot about making spontaneous decisions and learning to appreciate change, as well as learning several languages. Finally, I settled at the University of California at Berkeley for four years to pursue my bachelor's degree. Because of my fascination with planes and trains during my upbringing in Berlin and Tokyo, I studied mechanical engineering.

Throughout my studies, I developed an interest in electronic materials. I knew that understanding materials—their nature, how they're made, and what they can do—was paramount to innovating new technologies to address pressing needs related to energy and security. Thus I enrolled at Cornell University to pursue a PhD degree in materials science.

Throughout my time at Cornell I balanced my time between research, taking classes, Nordic skiing, and entrepreneurship. The experience of my first cold, long winter in Ithaca, NY taught me the value of staying active and I soon trained for and raced on the Cornell Nordic Ski Team. Although I had never skied Nordic before, the experience taught me a lot about endurance, which I needed for the PhD program. Another way I occupied my time was by starting a business. I had always had an extreme drive for finding ideas and commercializing them. Due to some side interests in finance, I decided to form a business that sold trading and risk management strategies to investors and

businesses. Because I had no prior experience in business, the experience was a tough, but educational one. However, because I had the fortunate opportunity to be around some talented and motivational people, I was able to exit the business for a profit in under two years. I hope to draw upon this experience as well as my knowledge and training as a PhD student to continue as an entrepreneur for a living.

To my two younger sisters, Kamila and Kate,

who have always looked up to me and given me

a reason to keep going.

ACKNOWLEDGEMENTS

“Whatever you can do or dream you can, begin it. Boldness has genius, power, and magic in it. Begin it now.”

-Johann Wolfgang von Goethe

I would first like to acknowledge the members of the Eastman research group at Cornell. Les Eastman’s and Bill Schaff’s willingness to mentor me on such a complex of subject as nitride semiconductors and their patience despite my endless visits to their office for questions is much appreciated. I further value Xiaodong’s expertise and willingness to teach me MBE technology, as well as Quentin Diduck’s and Jonathan Felbinger’s instruction on device physics, an area previously unfamiliar to me. I am also grateful for discussions and joint efforts in characterization and processing, respectively, with Dong Hao and Junxia Shi. Lastly, I found my discussions with Prof. Mike Spencer, Maura Weathers from CCMR, and the CNF staff to be particularly helpful.

A great deal of my research would not have been possible had a few institutions not have been open to collaborations. I’d like to thus acknowledge the Fraunhofer Institute for Solar Energy Systems in Freiburg, Germany, led by Eicke Weber, and the people I worked with and received much assistance from, including Gerald Siefer, Frank Dimroth, Jan Schöne, and Andreas Bett. I would also like to thank the microelectronics research group at Northrop Grumman (AS) at Redondo Beach, CA. In particular I would like to thank Claire Petite-Hall, Vincent Gambin, Ben Heying, Benjamin Poust, Y.C. Chen and Dwight Streit.

In addition, my research projects would not have been possible without funding sources such as the Office of Naval Research, Rose Street Labs, Structured Materials Inc., and UCSB MURI.

Lastly, I must express my deepest gratitude for the closest people to me. I thank my parents for their moral support, my life mentors Mike Faber and Kabral Sharpe for pushing me outside of my comfort zone and motivating me to go forward, and my good friends Oliver and Kunal whose humor gave me a refreshed perspective when things became difficult throughout my PhD research.

A special tribute to Lester F. Eastman

In this section I wanted to specifically acknowledge Professor Lester Fuess Eastman for his extreme willingness to help me throughout my time at Cornell and his confidence in me as a student and as a person. His keenness to do whatever it took for me to generate a firm understanding of Gallium Nitride-related physics and his praise for my work and for my aspirations to travel and be an entrepreneur is something I valued tremendously. I would secondly like to congratulate him for graduating 124 PhD students since he began his professorship at Cornell over sixty years ago. His students have become world renowned professors, government leaders, highly successful founders of large companies, and more. Les has traveled the world organizing conferences featuring cutting edge compound semiconductor technology and has worked with his students and extensive global network of colleagues to discover disruptive innovations in power electronics and microwave amplifiers. It is an honor to be part of this family and I give my sincere thanks for having the fortunate opportunity to work with him for over four years at Cornell.

TABLE OF CONTENTS

LIST OF FIGURES

LIST OF TABLES

LIST OF ABBREVIATIONS

2DEG	Two dimensional electron gas
AFM	Atomic force microscopy
AlGaN	Aluminum Gallium Nitride
CB	Conduction band
CV	Capacitance-voltage
CVD	Chemical Vapor Deposition
EHP	Electron-hole pair
EL	Electroluminescence
FF	Fill factor
GaN	Gallium Nitride
HEMT	High Electron Mobility Transistor
HFET	Heterojunction Field Effect Transistor
INDR	Inflection-point Negative Differential Resistance
InGaN	Indium Gallium Nitride
IV	Current-voltage
MBE	Molecular Beam Epitaxy
MOCVD	Metal Organic Chemical Vapor Deposition
PL	Photoluminescence

PV	Photovoltaic
RHEED	Reflective High Energy Electron Diffraction
RMS	Root-mean-squared
RTA	Rapid thermal annealing
SIMS	Secondary Ion Mass Spectrometry
THz	Terahertz
TLM	Transmission Line Measurement or Transfer Length Measurement
VB	Valence band
Wz	Würtzite structure

LIST OF SYMBOLS

(listed in order of appearance)

Γ zone center

E_0 built-in voltage

V_{OC} open circuit voltage

i_{SC} short circuit current

λ wavelength

L_e electron minority carrier diffusion length

L_h hole minority carrier diffusion length

W width

E_f Fermi level

α absorption coefficient, c-plane direction, or thermal coefficient of expansion

I_{ph} photocurrent

I_{max} current at which maximum IV product occurs under illumination

V_{max} voltage at which maximum IV product occurs under illumination

η fill factor

V_{po} pinch off voltage

P_{SP} spontaneous polarization

P_{PZ} piezoelectric polarization

C_{xy} elastic constant

e_{xy} piezoelectric constant

t_{crit} (h_c) critical thickness

ω phonon frequency

n- lightly doped

n++ heavily doped

E_g band gap energy

E_{br} break down field

m_e electron effective mass

κ thermal conductivity

R_S sheet resistance

Y_0 y intercept

R_C contact transfer resistance

ρ_C specific contact resistance

a epitaxial layer lattice constant

a_0 substrate lattice constant

ν_{PR} poisson ratio

f lattice mismatch

INTRODUCTION

History and applications of III-Nitride alloys

III-Nitride semiconductors have only occupied a short duration on the timeline of semiconductor history compared to other materials such as silicon and germanium. While the discovery of germanium and silicon had taken place in the 1800s and their implementation into society has spanned all the way to the present-day information age, the exploration of gallium nitride (GaN) and its alloys have taken place only seventy years from the time of writing. The actual implementation of the material into production-level technologies has spanned far less of a duration, however, the pace of growth in GaN and the potential it holds for electronics applications is staggering.

The first notable papers exploring GaN originated from Germany and the United States in the 1930s [1,2]. In the 1950s, a general industrial push for development of light emitting diodes (LEDs) supported an intense research effort by large scientific centers such as RCA and Bell Laboratories into compound semiconductor materials (such as GaAs) and thin film growth techniques to form the materials. By 1968, Maruska *et al.* realized that GaN would be a suitable material for making blue LEDs, since red and green had already been achieved and exploration to grow crystalline GaN commenced. By 1972, Maruska and Pankove were able to achieve single crystalline, p-type GaN material, which led to violet luminescence. It wasn't until 1995, however, that Shuji Nakamura developed the blue heterostructure LED to complement the other primary colors in the visual spectrum as well as provide better resolution for reading high density data storage media. As the race to develop the blue LED through the exploration of III-nitride materials continued, several

other alloys in addition to GaN began to surface in research: AlN, InN, InGaN, and AlGaN.

In addition to the unique optoelectronic properties that the nitrides held for photovoltaic, LED, laser, and photodetector applications, the nitrides also offered valuable properties for transistor applications. As government interest in the potential of the material to serve defense and communications applications rose, a patent detailing the “high electron mobility transistor” (HEMT, a.k.a. “HFET”) for high power, high frequency operations was filed in 1979. It was soon recognized that GaN would be an ideal material for this application because of its high electronic band gap, mobility, and break down field. By 2000, AlGaN/GaN polarization-HEMTs had been developed by Cornell University [3]. Around this time, a number of research labs, including those at Cornell, UC Santa Barbara, Cree, and HRL led the research effort to produce higher power, higher frequency GaN transistors [4]. Since 2006, considerable commercial production of GaN based transistors and optoelectronic devices ensued, and the industry continues to expand.

Properties and advantages of the III-Nitride material class

Gallium nitride has attracted much attention in materials and device research due to its electronic, optical, and mechanical properties. In particular, the high electronic band gap, breakdown field, and mobility facilitate exceptional performance for power switching and microwave amplifier applications, where high power and high frequency operation is required. The large band gap of 3.47 eV allows devices to operate at high voltages, and the high field mobilities of up to 2,000 $cm^2V^{-1}s^{-1}$ and saturation velocities of 3×10^7

$cm \cdot s^{-1}$ allow for high frequency and high current operation [5]. Furthermore, as will be explored later, the polarization properties of GaN and its alloy, AlGaN, allow the two materials, when put together, to confine electrons at their interface to form a high mobility current channel for transistors.

Figure 1 displays the electronic band structure of GaN. One notable feature of the figure is that the conduction band minimum at Γ indicates that GaN is a direct band gap material, making it ideal for optoelectronic applications such as lasers and LEDs, where carriers can gain enough energy to make a direct vertical (optical) transition in energy to emit photons. The latest lasers and LEDs using GaN material often combine other III-nitride materials along with GaN to take advantage of their optoelectronic properties. Another unique feature of the GaN band structure is the inflection point in the

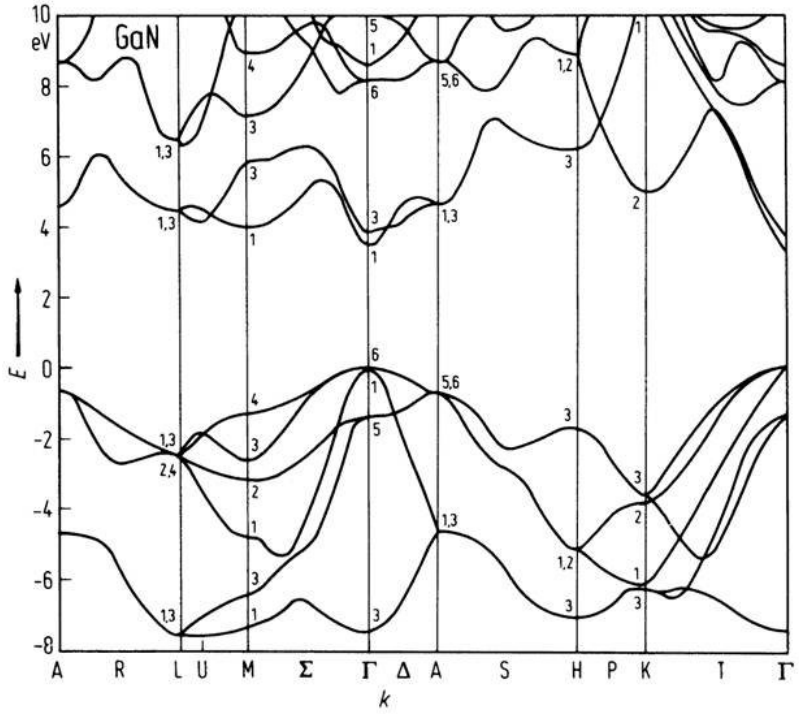

Figure 1. Electronic band structure of Würtzite GaN [6].

conduction band away from zone center (Γ), which leads to a negative effective mass of electrons, when enough momentum is gained. The negative effective mass allows for electrons to accelerate ballistically and reach their saturation velocities. Such properties are useful for terahertz radiation emitters, which become useful for security, climate and medical imaging, and communications applications. GaN terahertz emitters, although not yet realized at the time of writing, will rely on the negative differential resistance effect due to the unique GaN band structure to transport accumulation layers of electrons, which release pulses of terahertz wave radiation when dropping in energy.

The mechanical properties make GaN desirable for several device applications as well. For applications such as power transistors, where heat dissipation poses a large threat to device reliability, GaN offers a thermal conductivity of 130 $WK^{-1}m^{-1}$ (measured at room temperature), which is close to that of silicon, but much higher than GaAs, a traditional material for HEMTs. In addition, the high mechanical hardness and radiation resistance of the material offer unique suitability for intense environments such as space.

Although this introduction has focused primarily on GaN, its alloys share similarly impressive properties (see Appendix 1 for other III-nitride material properties). The ability to finely tune the alloy compositions and layer combinations of III-nitrides allows for fine control of the band gaps and band structure of devices, taking advantage of both the optical properties, electronic transport, and polarization properties that the III-nitride material system has to offer.

MBE growth of III-Nitrides

Molecular beam epitaxy (MBE) involves atomic layer growth of films via atomic, molecular, and ionized beams of matter on a heated substrate in a high vacuum environment. MBE is particularly advantageous for compound-semiconductor based devices such as lasers, light emitting diodes (LEDs), and high electron mobility transistors (HEMTs), in which very accurate control of growth rates and formation of abrupt junctions with ultra thin layers is required. Further advantages include the ability to monitor crystal quality and film growth *in situ* with reflective high energy electron diffraction (RHEED), as well as the ability to grow high purity materials because of the high vacuum present in the main chamber (typical base pressures are on the order of 10^{-10} Torr). The advantages, however, do not come without drawbacks. The ultra high vacuum system required for MBE raises system costs considerably, for example. Furthermore, the molecular beams cause very slow growth rates, often making it impractical and uneconomical to use MBE for applications that require high yield, large area, and high throughput production.

Figure 2 illustrates the main chamber of a III-Nitride MBE reactor. The chamber is constructed of thick stainless steel for ultra high vacuum operation. The chamber fits many modules, such as effusion cells for providing source material for film growth, characterization tools such as RHEED and quadrapole mass spectrometers, and other components. Effusion cells for each alloy and dopant source are included. Ga, In, and Al are heated in the effusion cells and allowed to evaporate through small orifices in a “molecular beam” toward the substrate. The nitrogen (or RF) source creates a plasma source of nitrogen that travels to the substrate as well, in the form of an

ionized beam. When the ionized nitrogen and the source metals combine at the surface of the heated substrate at the right thermal conditions, they typically form III-nitride compounds. The prime determinant of whether compounds will form or not is the substrate temperature and source metals such as In, Ga, and Al are more likely to condense on to the substrate at lower temperatures. The temperature must not be lowered excessively, however, to prevent growth the film stoichiometry from becoming imbalanced. Three additional heated effusion cells, Mg, and Si and Ge, serve as acceptor and donor dopant sources, respectively. Shutters are located in front of each cell to

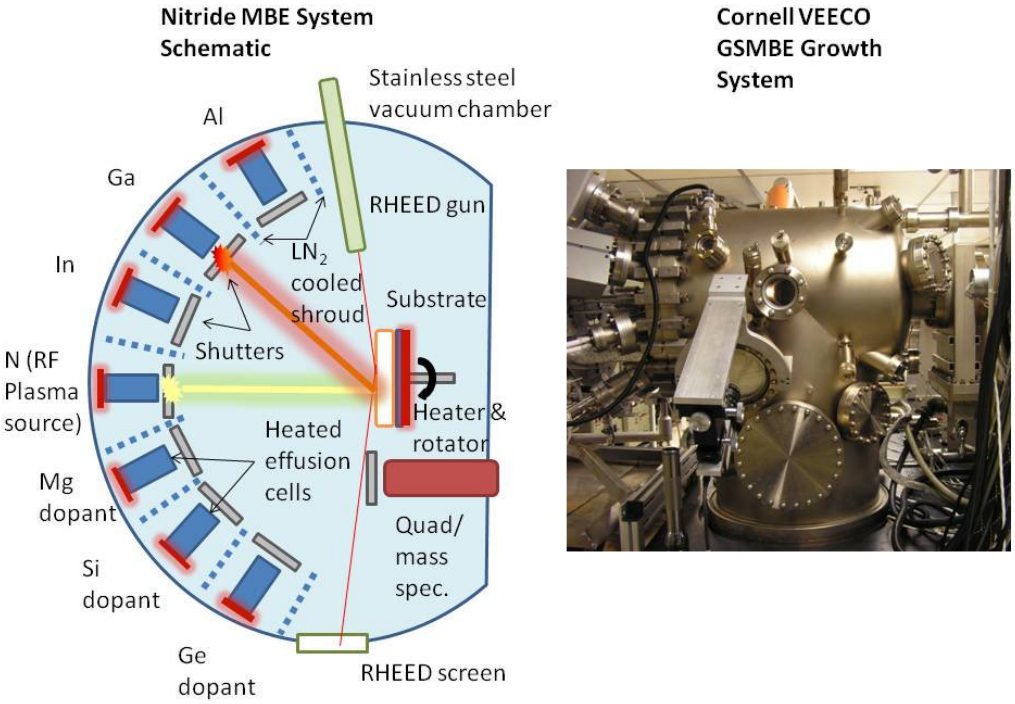

Figure 2. Schematic of components of a III-Nitride MBE growth chamber (left) and a photograph of the MBE growth reactor at Cornell used for this study (right).

allow precise control of material selection, film thickness, and doping profiles during growth. A metallic shroud with convection cooling via liquid nitrogen surrounds each of the cells and the lines the main reactor chamber in order to maintain low enough chamber temperatures for ultra high vacuum. The RHEED gun accelerates electrons that impinge upon the growing film at a very shallow angle to produce diffraction patterns of the very thin film being grown.The substrate is heated to ensure smooth films by allowing sufficient mobility of atoms arriving at the surface. And lastly, the quadrapole/mass spectrometer provides information regarding the pressures of various molecules/atoms present in the main chamber. The information is useful for determining if impurities are present in the chamber, as well as whether source metals are condensing upon the substrate to form the desired compounds or not at a given temperature.

Important parameters during film growth include substrate temperature and effusion cell temperatures. Although a variety of other parameters can be altered, these have been found to have the largest effect on film quality and electrical properties. As mentioned earlier, the substrate temperature influences the ability for certain constituents to stick to the substrate, as well as the III:V ratio. Typically, higher substrate temperatures result in nitrogen-rich (V-rich) material, whereas lower temperatures encourage metal-rich (or III-rich) material. Nitrogen rich materials have demonstrated semi-insulating electrical properties and rough surface morphologies. Metal rich layers display higher conductivity, however, metal droplets form and mobility decreases significantly [7]. This change in the III:V ratio can be monitored by looking for patterns and changes in light intensity in RHEED patterns during growth. All

else equal, brighter, spottier patterns tend to signify rough, N-rich film growth, whereas dark, streaky lines tend to indicate smooth, metal-rich growth. Since the film growth continuously shifts back and forth through this continuum, constant monitoring of the growth is required so that appropriate adjustments can be made. In addition to substrate temperatures, effusion cell temperatures greatly influence the film properties. Increasing the temperature of source metals will create a corresponding increase in flux. If an alloy is being grown, such as $In_xGa_{1-x}N$, the relative change in temperatures of In and Ga will directly influence the alloy composition. The last critical process step that determines film quality is the preparation preceding growth. In MBE systems it is imperative to keep vacuum parts clean and free from contamination (especially organic material). When the sample enters the reactor it undergoes a low temperature outgas (400 ℃) and a high temper ature outgas (1000 ℃) procedure to evaporate any material covering the substrate so that a clean, bare surface is available for film nucleation and growth.

The studies in this thesis cover MBE growth of III-nitrides for three principal applications: solar cells, high electron mobility transistors (HEMTs), and terahertz emitters. The interplay between several material and electronic issues such as MBE film quality, doping levels, alloy compositions, carrier mobility, and leakage will be explored in the next three chapters.

I. NITRIDE SOLAR CELLS

Background

The group III nitride materials class offers a unique set of advantages for photovoltaic (PV) electricity generation. Firstly, the direct energy gap of nitride alloys covers nearly the entire terrestrial solar spectrum (see Figure 3). By changing the composition of InGaN or InAlN alloys, the electronic band gap can be tuned to absorb different wavelengths of light. With a multi-junction solar cell based on these tuned InGaN or AlInN alloys it's possible to achieve higher efficiency than current photovoltaic cells made with the GaInP/GaAs/Ge stack [8,9]. Secondly, the high degree of radiation hardness [10] makes nitride

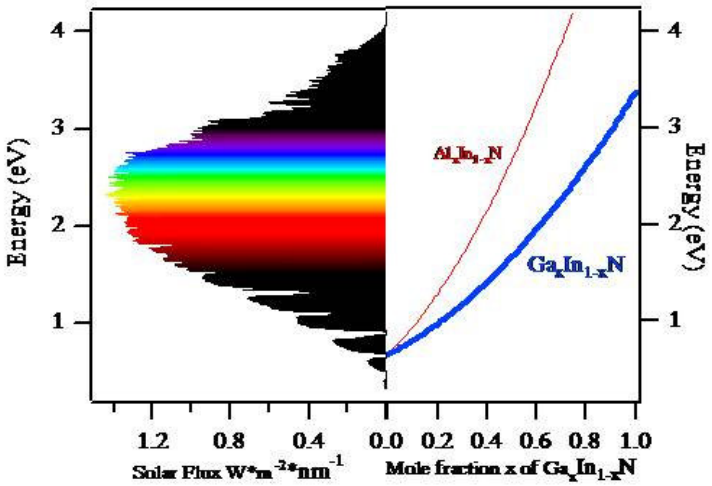

Figure 3. A plot comparing the range of band gaps of InGaN and InAlN alloys as a function of alloy composition to the solar spectrum on earth (image courtesy of W.J. Schaff).

based cells ideal for concentrator modules, which receive more sunlight and heat per unit area than traditional silicon panels. This is potentially advantageous because the smaller physical footprint, simplified installation, and longer lifetimes associated with concentrator PV systems can lead to

large cost savings. Furthermore, the increased economies of scale of using a centralized model of power generation (typical of concentrator PV systems) as opposed to customized residential rooftop installations of silicon based solar panels could prove to be much more financially viable.

Despite the unique advantages of the nitrides, certain challenges must be overcome to achieve device performance for wide scale usage. Physical defects, for example, lead to considerable electrical leakage, thus decreasing the performance of PV cells. One type of defect includes grain boundaries in the epitaxial layers of the cells which contribute to short conduction paths of minority carriers [11]. Another type of defect is the surface of the nitride material itself. Because of the ionic bonds in the material, a strong polarization field exists that pushes carriers to the surface. This is particularly destructive to performance in p-type InGaN, in which the higher indium concentration pulls the conduction band below the Fermi level and causes electrons to accumulate at the surface, shorting out minority carrier holes at the surface in the process. Lastly, the large activation energy of acceptors in the nitride material class makes it difficult to achieve high levels of activated hole density required for minority carrier-based devices such as PV cells [12].

Solar cell operation

The operating principle of a photovoltaic cell is depicted in Figure 4a. Photons enter at the p-type side of the cell and penetrate the cell to a depth that is characterized by the absorption length, which increases with the wavelength of the photon. The energy of the photon, if larger than the band gap of the material, excites electrons from the valence band and holes from the conduction band. Because of the built in field, E_0, due to the presence of a

p-n junction, electrons formed by the irradiating photons drift toward the N side of the junction, and holes drift toward the P side of the junction. The buildup of positive charge on the P side and negative charge on the N side leads to the presence of an open circuit voltage, V_{oc}. If an electrical connection were to be made between the P and N side, the charges would flow, leading to a short circuit current, i_{sc}.

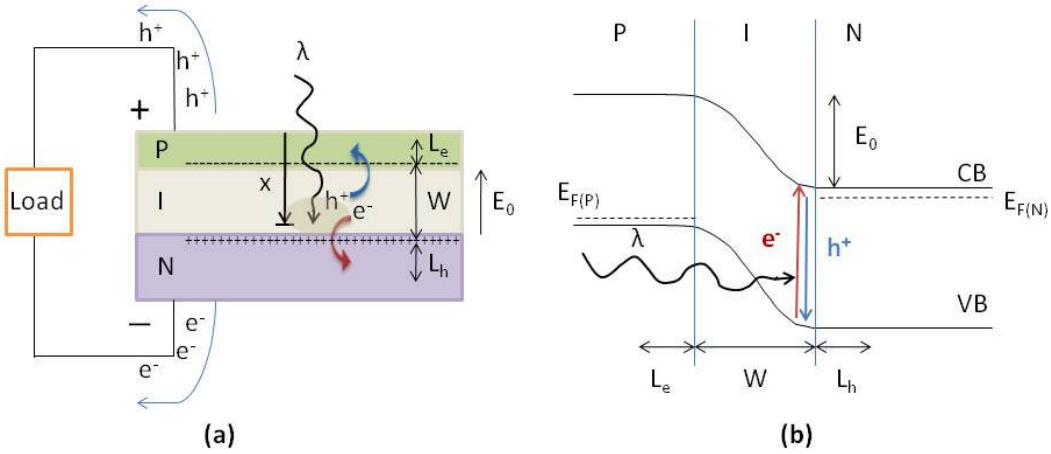

Figure 4. a) A diagram depicting the photovoltaic defect in a P-I-N junction connected to a load. b) The photovoltaic effect illustrated in terms of the electronic band diagram in a P-I-N junction.

Figure 4b depicts the photovoltaic effect again, except from the perspective of a band diagram. When electron-hole pairs (EHP) form due to light absorption in the I-layer, electrons readily drift down the negative slope (formed by the electric field caused by the P-N junction) to the N side. Likewise, holes readily float up the gradient from the I side to the P side, where they can be collected as current. If electrons are generated from the absorbed light on the P side, they are known to be *minority carriers.* Minority carriers have a finite lifetime and *diffusion length, L,* before they recombine

with majority carriers and are unable to contribute to photocurrent. Likewise, EHPs generated on the N side due to long wavelength radiation will produce minority carrier holes, which must diffuse to within the I layer (or depletion width, W), where they can readily drift to the P side and be collected as current. In order for this to happen, the absorption length of a photon must take place within an approximate distance of L_h from the I layer (L_e for electrons).

The absorption length of light for a given wavelength of radiation, λ, can be found by the following formula describing the relationship between light intensity and depth:

$$\frac{I}{I_0} = \exp(-\alpha x)$$

where I is the photon flux at a depth x, I_0 is the photon flux impinging on a wafer of a semiconductor with parallel faces, and α is the linear absorption coefficient. By assuming that photons are absorbed when intensity decreases by a factor of 1/e, the absorption length x is equal to 1/α.

The unintentionally doped I-layer is included to provide a carrier-free region for generated electrons and holes to drift uninhibited to the N and P sides, respectively, and contribute to the generated current output of the cell. Unfortunately, rather than a single wavelength of photon being irradiated upon the cell, an entire spectrum of photon wavelengths is typically present, leading to different absorption depths at which the electron-hole-pair (EHP) generation takes place. If the EHP generation occurs outside the depletion width, W, no electric field is present to drift the minority carriers to their respective majority regions to be collected as current. Instead, the carriers must rely on diffusion

caused by concentration gradients to return to the depletion region so that they can drift back. Unfortunately, the diffusion lengths of the electron and hole minority carriers (L_e and L_h, respectively) are finite and limited by the rate of compensation by oppositely charged carriers. If EHPs are produced at a depth greater than L_h in the N region, holes will be recombined with electrons before reaching the depletion width and contributing to the cell current, thus reducing the efficiency of the PV cell.

For these reasons, the doping density and thicknesses of each of the doped and undoped layers must be carefully controlled to ensure a balance between efficient light absorption and transport of generated carriers. The P layer is grown thin (usually 80 nm) so that light can pass through and to minimize the diffusion distance of minority electrons produced by short wavelength radiation. The I layer is typically 200-300nm in thickness to supply a neutral charge region in which light can be absorbed and in which electrons and holes can travel without being annihilated due to recombination. Although it is advantageous to make the I layer thicker in order to capture EHP generation due to light consisting of a broad spectrum of absorption depths, making the layer too thick would reduce the electric field between the p and n layers so much that carriers would not have a strong driving force to drift to their respective sides of the junction. The N layer is typically 1 μm in thickness to strike a balance between growing a layer thick enough to reduce dislocation density, yet thin enough to reduce growth time.

The high doping levels of Mg acceptors (2×10^{20} cm^{-3}) and Si donors in InGaN help increase the electric field in the I layer so that minority carriers, which contribute to the photocurrent of the cell, can easily drift to their

respective sides of the junction. As with the case of the layer thicknesses, similar caution should be exercised to not over-dope the layers or else excess majority carriers could be generated, which would increase recombination rates and decrease photocurrent.

Because the PV cells investigated resemble PN junction diodes, the diode characteristic equation can be used to describe the current-voltage characteristics of the device (excluding series and parallel leakage characteristics, which will be elaborated upon later on):

$$I(V) = -I_{ph} + I_0 \left[exp\left(\frac{eV}{\eta kT}\right) - 1 \right]$$

where I_{ph} is the photocurrent given by the following equation:

$$I_{ph} = eG[L_e + L_h]$$

L_e and L_h are the electron and hole diffusion lengths, respectively, and G is the generation rate of carriers, which depends on the intensity of light irradiating the junction and the cell efficiency.

The relationship in the I(V) equation is plotted in Figure 5. The plot reveals relevant performance information of the cell. Under “dark” conditions, no photocurrent is generated and current should theoretically be at a near-negligible current until a sufficiently high voltage is reached in the diode such that it “turns on” and passes current (usually near the band gap voltage of the diode material). Unfortunately, the presence of parallel conduction paths often causes current to leak, producing a noticeable current at negative and slightly positive voltages, denoted by I_{pl} in the figure. Another undesirable effect of solar cell performance is series resistance. As current travels through the cell,

different features, such as the electrical contacts or interfaces between different layers can cause inefficient transmission of current, resulting in losses in the form of heat. The lower the slope of the I-V plot after the PV cell turns on at higher voltages, the more series resistance is present, which reduces the efficiency of the cell.

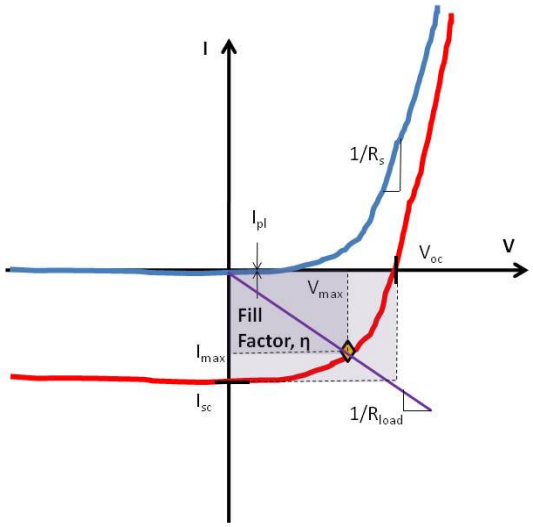

Figure 5. Current-voltage characteristics and relevant parameters of dark vs. illuminated PV cells.

Depicted in red is the I-V characteristic of the same cell under illumination. The photocurrent causes the I-V curve to get displaced vertically, producing a short circuit current, I_{sc}, and an open circuit voltage, V_{oc}, which increases with I_{sc}. A common measure of efficiency in the cell is the fill factor, . Assume the cell is connected to a load in a circuit of resistance, R_{load}, which intersects the IV curve at the point of maximum power, which is the product of I_{max} and V_{max} and is the point on the curve furthest from the origin in the fourth

quadrant of the IV plot. Since the maximum voltage the cell can produce is V_{oc} and the maximum current is I_{sc}, the product of these two quantities represent the maximum ideal operating range of the cell. From an efficiency standpoint, it is thus desirable to design a cell that covers as much of this range as possible. The fill factor quantifies this as a percentage:

$$\eta = \frac{I_{max}V_{max}}{I_{sc}V_{oc}}$$

Thus, a cell whose IV curve turns on at as close to a right angle (on a linear IV plot) as possible will have the highest fill factor. The curve shape can be improved by reducing series resistance and parallel leakage current.

InGaN solar cells

Molecular beam epitaxy (MBE) is used to grow $In_xGa_{1-x}N$ and $In_xAl_{1-x}N$ alloy films to form solar cell materials with high material quality, high doping levels, and good layer thickness control. As depicted in Figure 6, the growth process starts by growing AlN and GaN buffer layers on sapphire 6H (0001) orientation substrates at 800 ℃ to reduce atomic l attice mismatch between the active solar film alloys and the substrate. The buffer layer for AlN is typically 250 nm in thickness, while that of GaN is at least 1 μm to reduce defect density. The substrate temperature is then lowered to between 550-600 ℃ to grow the active layers, which consist of an N layer of InGaN, an intrinsic layer in which the InGaN is unintentionally doped, and finally, a P layer. The temperature of the indium is adjusted to control the indium content in the alloy and thus the band gap. Silicon or germanium is used as a donor dopant for the 1 micron-thick InGaN layer. Magnesium acts as an acceptor source for the p-type cap layer which is typically 80 nm thickness. Careful attention to the Mg

doping level ensures that it is high enough to provide a sufficient acceptor charge density for a strong electric field, yet at the same time, low enough to prevent excessive damage to the surface from bombardment of Mg atoms and an excessive hole density, which would annihilate many generated minority electrons.

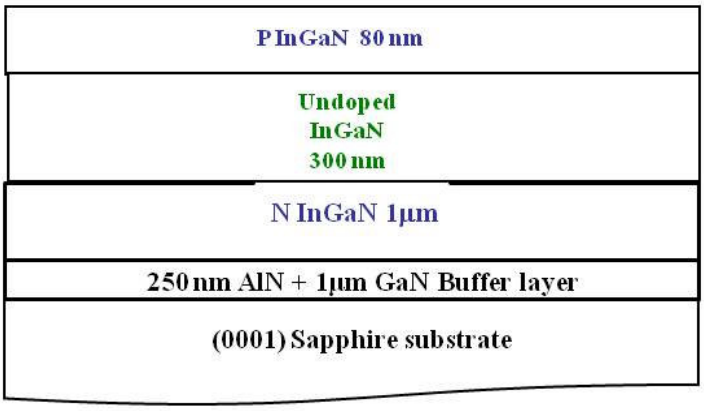

Figure 6. InGaN solar cell layer structure for MBE growths.

Epitaxial film layers grown on sapphire such as in the above condition then undergo a three step fabrication process for solar cell fabrication. A cross sectional schematic of an individual solar cell device is represented in Figure 7. The first step involves photolithography and liftoff of p-type ohmic metal contacts. Following photoresist coating of the samples, a G-line 5X stepper tool is used to expose the sample with UV radiation through a mask containing the patterns of the p-type layer. After developing the pattern, the exposed chip undergoes a descum process to remove any excess underdeveloped photoresist, as well as a buffered oxide etch solution (30:1) for 30 seconds to provide a clean surface for metal deposition.

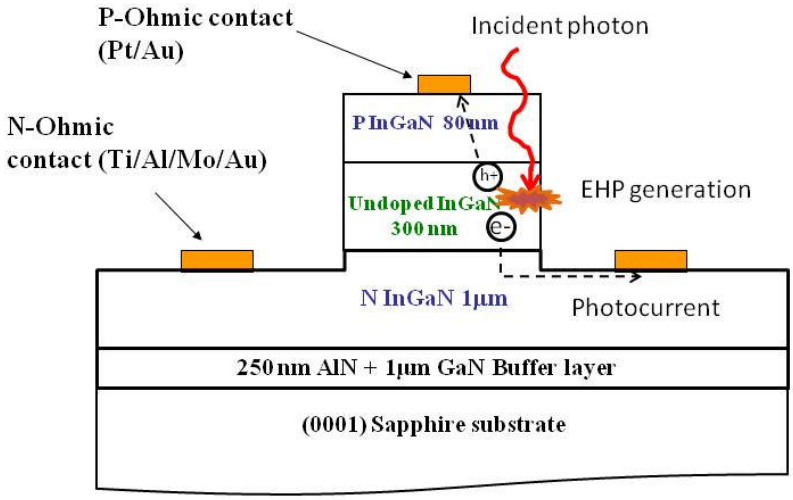

Figure 7. Schematic of completed solar cell device structure.

The sample is then immediately placed in a CVC evaporator to deposit ohmic contact metals. The second lithography step forms a mesa to electrically isolate the P and N regions, as shown in Figure 8. A Plasmatherm reactive-ion-etch tool is employed to etch patterned areas to a depth of at least 400 nm with a $Cl_2/BCl_3/Ar$ gas chemistry solution. The third and final step repeats the process for the P-layer, except a different set of contact metals with lower work functions are employed to form n-type ohmic contacts.

Because the hole diffusion length is low in InGaN, it is necessary to design the device architecture with maximum current collection efficiency. In order to allow a balance between exposed area for light collection and current collection (by reducing series resistance), the contact metals were deposited in high aspect ratio “finger” patterns.

Multiple cells in each process were patterned with different numbers and widths of fingers to find the most optimal conditions. Furthermore, circular diodes (with the same p-i-n structure as the solar cells) of varying size were included in the layout for diagnostic purposes, such as determining the source of parallel leakage. Each solar cell was roughly 1 mm^2 in area and included either standard or *interdigitated* finger geometries (see Figure 8). The interdigitated finger geometry was included to investigate if minimizing the distance that minority carriers had to travel to P and N contact fingers would increase collected current and decrease lateral series resistance.

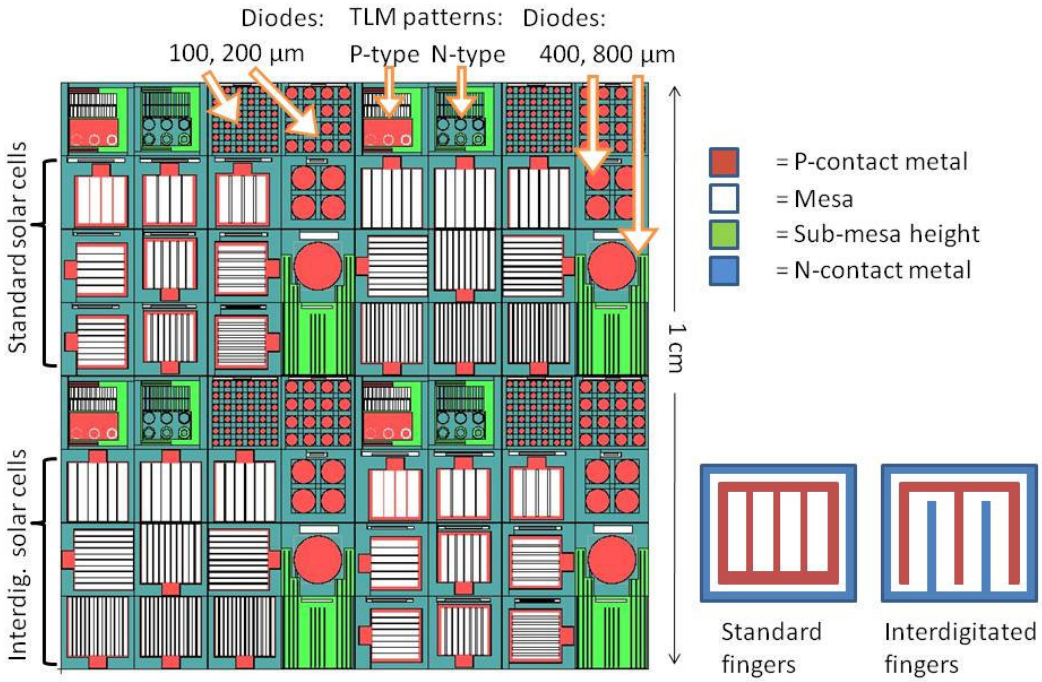

Figure 8. Solar cell process layout (left, color coded with respect to different layers of lithography process) and types of contact finger geometries for cells.

Performance of InGaN solar cells of various compositions is detailed in Figure 9. As the concentration of indium, x, in the $In_xGa_{1-x}N$ alloys increases, the devices turn on at much lower voltages. Although it is expected that this

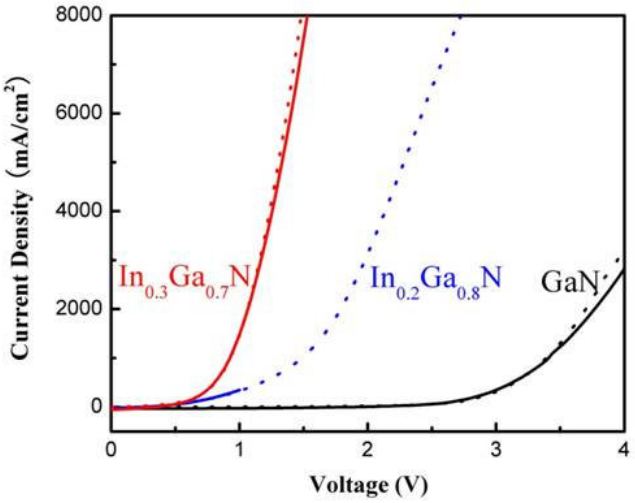

Figure 9. I-V characteristics of InGaN cells with indium compositions of 0, 20, and 30% under dark conditions

would happen since the additional indium decreases the band gap of the material, the parallel leakage current becomes quite pronounced, as can be seen by the gradual, as opposed to sudden increase in current at lower voltages. Furthermore, the large series resistance reveals itself through the shallow slope of each of the curves after the devices turn on. The problem is exacerbated for InGaN alloys because of the high work function metals required as well as the poorer material quality associated with ternary alloy growth. The finger geometries of the different solar cells had no correlation to device performance.

Completed $In_{0.2}Ga_{0.8}N$ and GaN cells underwent tests of IV performance under simulated, concentrated sunlight. Simulated sunlight originated from a pulsed AM 1.5 spectrum source manufactured by Spectrolabs in an experiment performed at the Fraunhofer Institute for Solar Energy Systems in Freiburg, Germany. Special 1 cm^2 area cells with interdigitated fingers were fabricated in lieu of the standard 1 mm^2 area cells in order to provide more area for light absorption and thus higher photocurrent, since the pulsed light setup measured current on a very short time scale and would produce a low signal to noise ratio. Figure 10 displays the current-voltage characteristics for an InGaN alloy based cell with 20% In composition under various degrees of concentration. At a maximum solar concentration of 900x, the cell produced a photocurrent of 4 mA and open circuit voltage 0f 0.2 V at a fill factor efficiency of 31%.

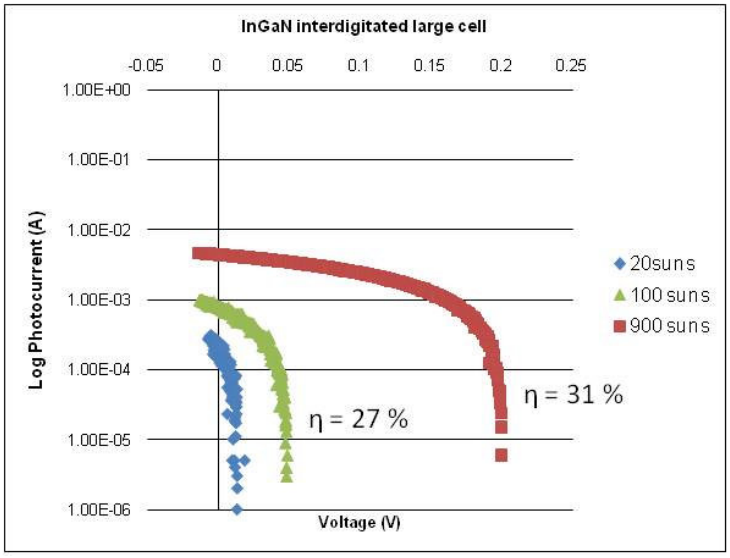

Figure 10. IV characteristics of an $In_{0.2}Ga_{0.8}N$ 1 cm^2 area solar cell with fill factor percentages for various concentrations of simulated sunlight.

Although the data taken at each concentration level seems to show an increase in efficiency (as noted by the fill factors) and an increase in short circuit current, the performance values are much lower than expected, considering that the large size of the cell should have yielded more photocurrent, and also that the band gap of 2.6 eV should have produced a higher open circuit voltage. Leakage caused by microstructural defects are likely responsible for the deviation in performance vs. expectations. To investigate this further, the large cell was biased to voltages well above the turn on voltage (up to 10 V) to observe any electroluminescence (EL). Green light was visually observed only in certain regions of the cell, suggesting that not the entire cell was functioning correctly and that some sort of electrical defects were indeed present. This measurement was repeated for multiple cells and similar effects were observed, indicating that it was not a device processing defect, but rather a material defect.

A GaN-based interdigitated device with identical device characteristics underwent the same test and produced a maximum open circuit voltage of 1 V and a photocurrent of 20 mA at a fill factor of 34% (see Figure 11). As expected, the fill factor, open circuit voltage, and photocurrent all increase with level of concentration, however the open circuit voltages are much lower than expected, considering that the band gap of GaN is 3.4 eV. The underperformance of the open circuit voltage is even more of a surprise in GaN since surface electron accumulation (a phenomenon believed to be responsible for current leakage in nitride based solar cells with higher indium compositions [13]) is nonexistent. The fill factor is not calculated for the lowest

concentration level because the low signal to noise ratio of the data cannot be trusted to deliver a reliable figure.

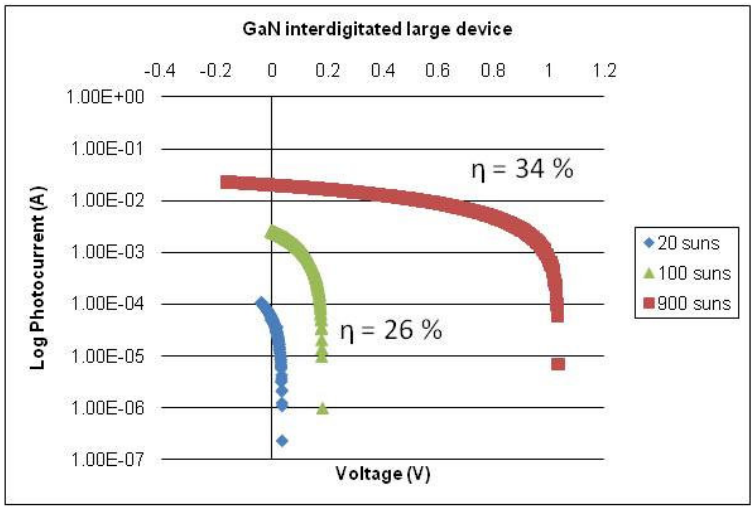

Figure 11. IV characteristics of a GaN 1cm^2 area solar cell with fill factor percentages for various concentrations of simulated sunlight.

Due to the poor spectral response of GaN to the broad spectrum of sunlight (due to the high energy gap of the material), it is expected that efficiency should not be stellar. As GaN more efficiently absorbs light at the UV end of the spectrum, a 1 mm2 cell was subjected to 325 nm laser light and produced the current voltage characteristic reflected in Figure 12. The cell produced current density and open circuit voltages of 30 mA·cm^{-2} and 2.5 V, respectively, at a fill factor of 61%, far exceeding values exhibited under broadband sunlight.

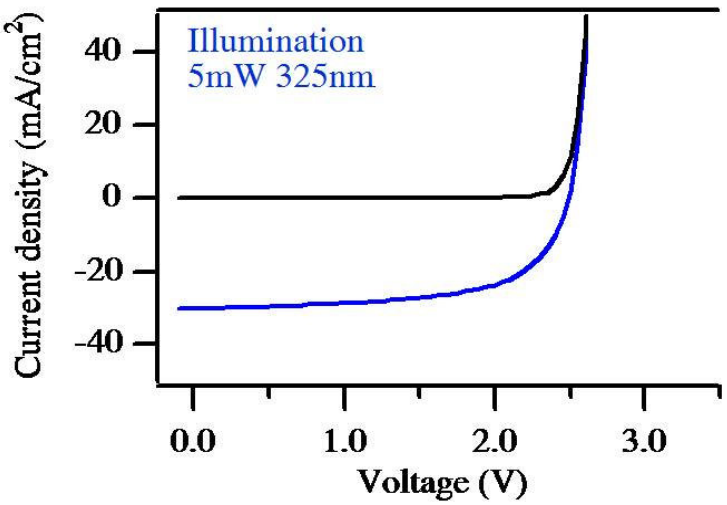

Figure 12. GaN solar cell IV performance under illumination by a 5mV 325 nm laser.

Solar cells based on GaN and InGaN material grown via MBE has been successfully demonstrated, although the performance of the cells has not yet met expectations based on device theory. Certain evidence suggests that electrically active material defects, including the surface of the film and extended defects, may be responsible for the leakage, which leads to poor performance. These initial results necessitated an increased theoretical understanding of the current-voltage performance in the InGaN cells, leading to the formation of a diode model for nitride P-I-N devices.

InGaN solar cell model

As the preliminary results show, InGaN and GaN PV cells behave far from ideally. A diode-resistor model was developed to understand and explain the reasons for performance in these cells. The non-ideal model for InGaN solar cells accounts for both series and parallel leakage. The model is illustrated in Figure 13. The diode circuit representing an InGaN cell is

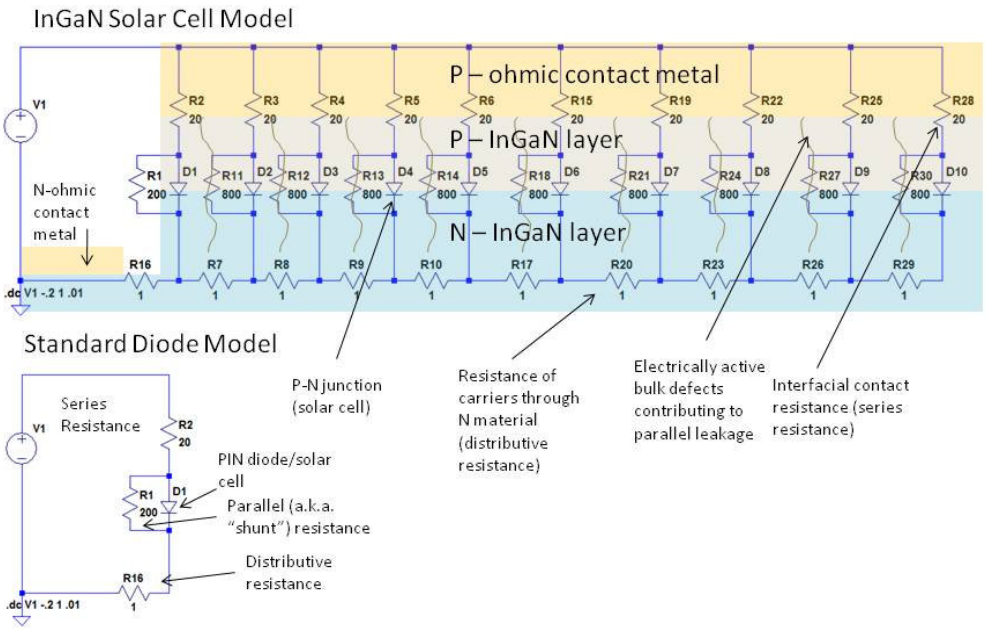

Figure 13. Top: A diode model for representing InGaN solar cell IV performance superimposed upon the layer structure of a standard InGaN cell. Bottom: A standard diode model (and simplified version of the InGaN solar cell model), consisting of a diode with series and parallel resistance.

superimposed upon a schematic of the P-I-N layer structure to relate the various circuit components to features of the materials. The circuit includes

several standard diode models in parallel to reflect a phenomenon known as distributive resistance. Distributive resistance is caused by the resistance of the material to carriers travelling through it to a contact. The resistance increases with distance travelled, which carriers injected further from the contact must face. In addition to distributive resistance, series resistance due to the interface between the ohmic metal contact and the doped semiconductor layer is reflected in the circuit model, and produces a voltage drop that causes the diode to produce less current at higher voltages. Finally, the P-N diodes are modeled in parallel to a *shunt* resistor, which provides an alternate conduction path and causes current to leak at lower voltages. This can be either caused by line defects traversing vertically through the layers, represented by R11, or conduction along the electron-rich surface (due to surface accumulation in InGaN alloys with an indium concentration larger than 30%, represented by R1 on the left edge of the diagram.

To better understand the effect of distributive resistance on performance, Figure 14 can be considered. Depicted on the right is the IV performance characteristic of an ideal diode: current remains near zero until the device reaches a voltage near the band gap and turns on. Illustrated on the left in solid, however, is the characteristic of a leaky diode, exhibiting both series resistance and parallel leakage. It should be noted that the current begins to creep up at low voltages (reflecting parallel leakage) and has a significantly shallower slope after turn-on (reflecting the presence of series resistance). The dashed curve represents a diode model with identical characteristics,

however, with the added feature of distributive resistance. The presence of distributive resistance further limits the current flow in the circuit, causing leakage at lower voltages to appear to decrease, although the current degrades considerably at higher voltages and produces a very rounded corner in the IV curve. The rounded corner, as opposed to a sharp corner at a particular voltage, arises from the fact that multiple diodes coexist in parallel, although they receive different voltages due to the distributive resistance (see the model in Figure 13). This reduces the potential fill factor (and consequently, the cell efficiency) for devices in which distributive resistance is present, when subject to irradiation.

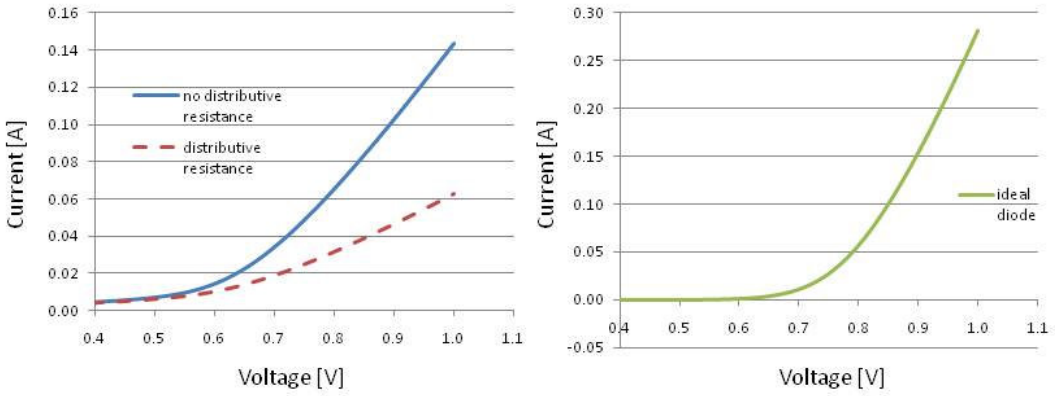

Figure 14. Simulated IV curves comparing models of a moderately leaky diode, a leaky diode with distributive resistance (both left), and an ideal diode (right).

A combination of initial results of GaN and InGaN PV performance, as well as clues from the solar cell device modeling above led to a series of material-level and device-level studies in an attempt to mitigate factors negatively affecting performance.

Device performance improvement studies

Since IV characteristics of InGaN and GaN solar cells revealed subpar performance, several device changes took place in an attempt to reduce current leakage and series resistance in the cells. To address the issue of leakage, experiments concerning the MBE growth recipes and surface chemistry of the epitaxial layers were performed. Following these studies, the effect of series resistance within the solar cell devices was investigated by exploring various contact metals and high temperature annealing conditions.

Layer architecture

Dislocations have long been known to cause problems in nitride based devices based on minority carrier conduction such as PV cells [14]. InGaN material grows with a considerable density of line defects, which form conduction paths. Line defects in nitride materials tend to form deep, broad, energy levels compared to most acceptors and donors and act as traps [15] because they form dangling bonds, that due to their close proximity, form broad energy bands. Figure 15 (left) depicts the energy transition a conducting electron makes from the conduction band to a defect level in thick n-type InGaN in a standard PIN solar structure. Because of the high n-type doping in the material, the local conduction band is typically narrow enough to allow the electron to tunnel through the depleted barrier formed by band bending at the dislocation interface. The leakage that results from defects is further exaggerated by the high density of defects, whose number increases as the indium concentration of the alloy rises. Figure 15 (right) also depicts the energy diagram for the case in which the defects traverse through a thick p-type InGaN layer in a reversed, “NIP” structure (the p-type layer is now in

contact with the buffer rather than being at the surface: see layer diagram in Figure 6), in which the charge state and the energy bands of the dislocation are reversed. It was anticipated that the reversed charge of the dislocations would prevent current leakage by not trapping carriers.

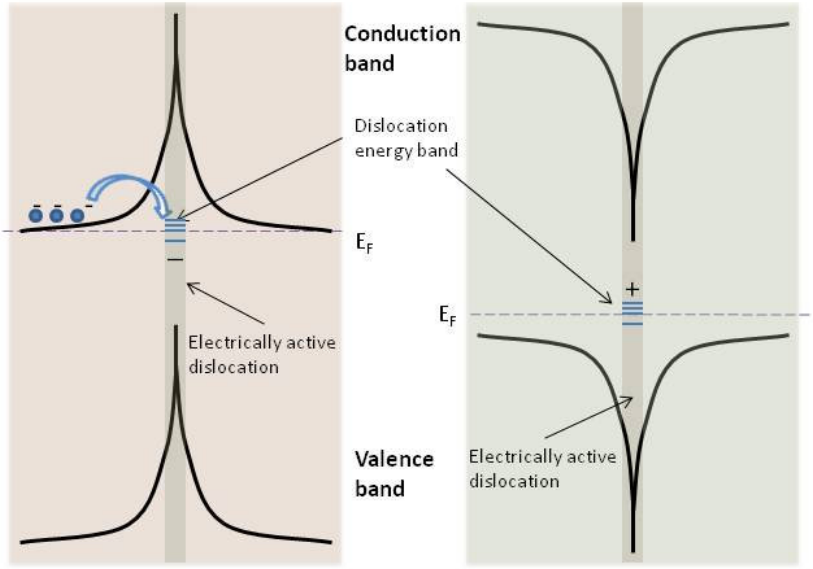

Figure 15. Local band diagrams of InGaN solar cells near a dislocation traversing a thick N layer (left) and a thick P layer (right).

This theory was applied to the fabrication of a solar cell with a reversed layer architecture (instead of a thin p-type layer at the surface and thick n-type layer in contact with the buffer, a thin n-type layer existed at the surface and thick p-type layer at the buffer). The log IV performance of 100 µm sized devices is exhibited in figure 16. The novel NIP architecture disappointed expectations by showing even worse leakage than standard PIN architecture

devices and showed no evidence of a distinct “turn on” characteristic in the IV curve. Although at first glance the NIP device appears to have a lower parallel

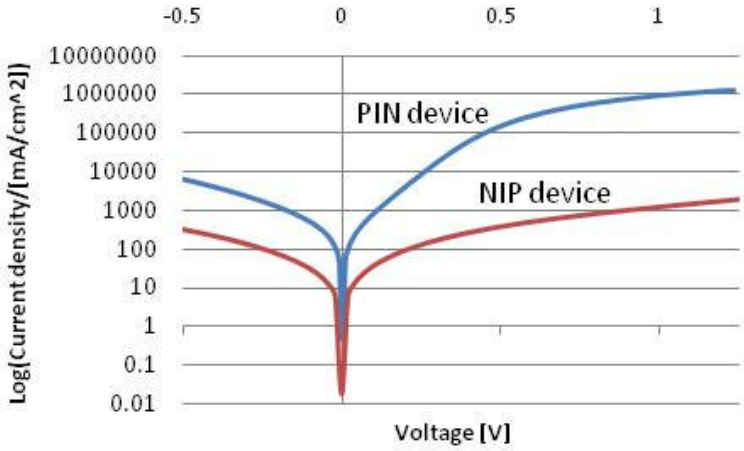

Figure 16. IV comparison of PIN vs. NIP layer structure in 100 μm-sized diode devices on InGaN material with 30% indium concentration.

leakage current as seen by the low current near 0 V, it is more likely caused by high resistance in the junction. The NIP device architecture performance failed to meet theoretical expectations, possibly due to the saturated defect density in InGaN. Since this was an attempt to change the electrical effect of an undesirable feature of the material, effort was then directed to a different area of device improvement: changing the material chemistry and microstructure, thus altering the electrical performance.

Contact metal selection

As mentioned previously, the interfacial resistance between the ohmic metal and the nitride semiconductor surface must be minimized to ensure efficient solar performance. The Ni/Au metal stack has been used as a

standard ohmic metal configuration on p-type GaN and InGaN based devices, yielding a specific contact resistance of 2.99 x 10^{-2} $\Omega \cdot cm^2$. A study was conducted to improve the specific contact resistance to p-type InGaN. InGaN produces a unique challenge for forming p-type ohmic contacts because of the high work function in p-InGaN [11].

Figure 17 exhibits the specific contact resistance as a function of anneal temperature for four different ohmic metal stacks (Pt/Au, Pd/Au, Ti/Pt/Au, and Re/Au) evaporated on to p-type InGaN of 5 and 20% indium concentration. The metal pads were deposited in the form of rectangular transfer length measurement (TLM) patterns to facilitate the measurement of contact resistance (see Appendix 2). Pt, Pd, and Re were chosen as base metals for contact with the InGaN semiconductor material because of their high work functions [16], while Ti was chosen due its adhesion properties, and Au is used to contact electrical probes for device measurement and testing and prevent metal flow during anneals. The metals were annealed using a rapid thermal annealer (RTA) at various temperatures for 30 seconds. The results show that a minimal contact resistance exists for almost all metals at an anneal temperature of 300 ℃, with a resistance as low as 6.9 x 10^{-4} $\Omega \cdot cm^{-2}$ for Pt/Au at a low indium concentration. The titanium layer, despite its superb adhesion properties, formed the highest resistance ohmic contact, possibly due to its lower electrical work function. Lastly, the addition of indium in the InGaN alloys increased the contact resistance in all cases. It is believed that this occurred due to an increased amount of downward band-bending at the surface of InGaN as more indium is added, which is created by increased surface accumulation of electrons.

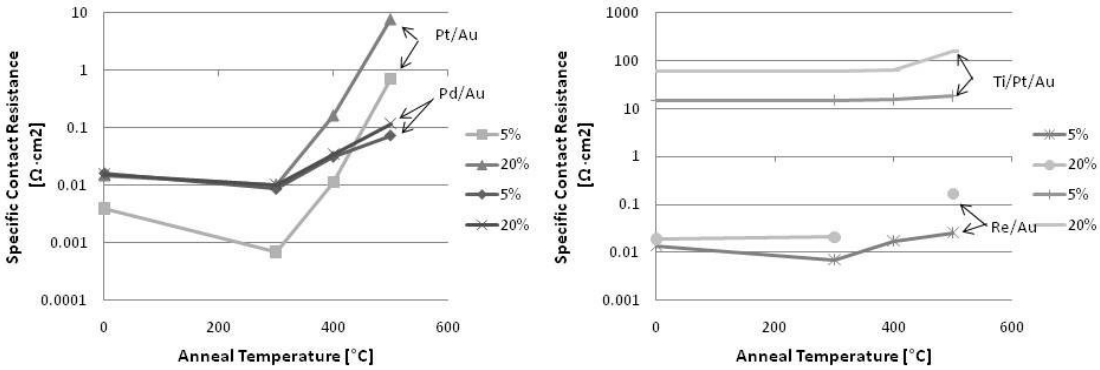

Figure 17. Specific contact resistance anneal profiles for various p-ohmic metal stacks and InGaN alloy compositions (percentage represents composition of indium in InGaN).

GaN photovoltaic cell IV performance for two different p-ohmic contact metallizations for solar cells fabricated on the same wafer is illustrated in Figure 18. The turn-on voltage near 3 V is consistent with the GaN band gap value in both cases, however the series resistance (as calculated by the inverse-gradient of the IV profile after turn-on) for the cell fabricated with non-annealed Pt/Au contacts is much lower (0.039 Ω cm^2 vs. 0.144 Ω cm^2 for Ni/Au contacts). Without annealing, a contact resistance of 4.91 x 10^{-4} Ω cm^2 and sheet resistivity of 62196 Ω /□ is obtained at a hole density of 2 x 10^{18} cm^{-3} in the p layer. As expected by the lower work function of Pt compared to Ni, the Pt/Au contacts lead a much lower resistance than the Ni/Au contacts and since no annealing is required to achieve such contact resistivity, concerns of contact or feature degradation during device operation (usually at high temperatures due to concentrated irradiation) are eliminated. TLM measurements confirm linear IV characteristics of the contacts.

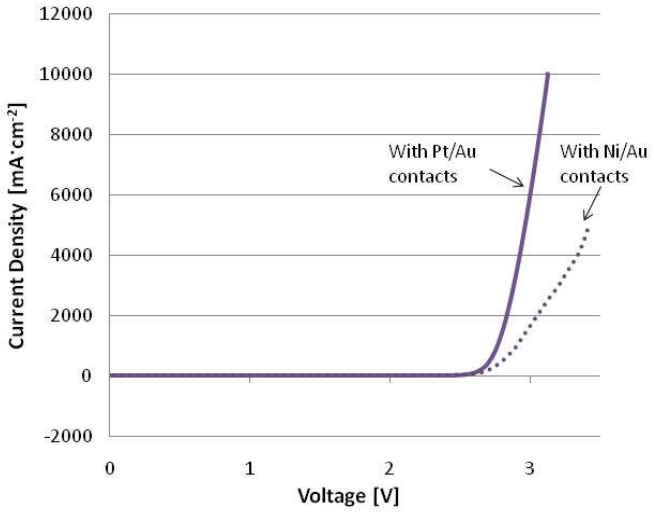

Figure 18. GaN 1 mm solar cell dark IV characteristics comparing Wafer 1 Process A with Ni/Au p-ohmic contacts (dashed line) and Process B on the same wafer with Pt/Au contacts (solid line).

Annealing

High temperature annealing is typically employed as a technique to improve contact resistance, improve the microstructure of the defect-littered nitride semiconductor material, or to activate Mg acceptors in nitrides that have been compensated by hydrogen [17]. In an attempt to reduce leakage effects in InGaN and GaN, fabricated cells were exposed to an RTA at various anneal temperatures from 450 to 600 ℃ for 30 secon ds. The results of the anneal in Figure 19a show a general decrease in parallel leakage current density (current density of 1 mm^2 cells measured at 0.05 V forward bias) from an initial anneal temperature of 450 ℃, indicating a possible improvement in the semiconductor material or the ohmic contact formation taking place. In contrast, the reason for the increase in leakage current with increase in

annealing temperature for the 31% InGaN cell is unknown. A general observation can be made that the low indium concentration cells (0, 14, and 24%) decrease consistently from no anneal to the highest anneal temperature. The higher indium content samples (26, 28, and 31%), however, seem to become worse initially at the starting anneal temperature. It is possible that the increased surface electron accumulation acting at higher indium concentrations is responsible for the increase in leakage (InGaN alloys begin to make a transition from having surface *depletion* of electrons to exhibiting surface *accumulation* after 25% In concentration). In fact, parallel leakage current density was used as the main parameter for characterizing performance here because it was believed that surface accumulation was the main culprit for poor performance in InGaN based cells. To investigate whether the decrease in current at lower voltages was indeed caused by a

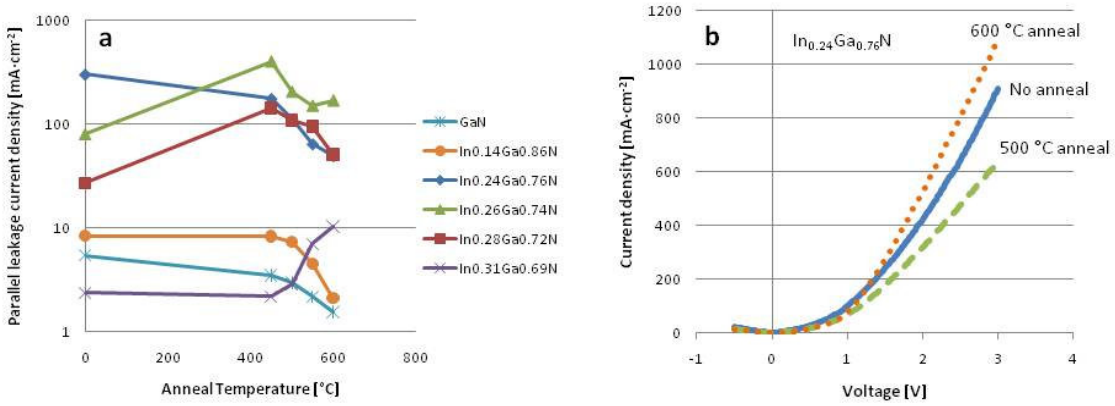

Figure 19. a) Leakage current densities of 1 x 1 mm InGaN solar cells recorded at 0.05 V forward bias across various anneal temperatures and indium compositions. b) IV profiles of a 24% In solar cell showing reduced parallel leakage (at 600 ℃) and increased series resistance (at 500 ℃) compared to non-annealed performance.

decrease in parallel leakage and not by a substantial increase in series resistance, IV characteristics similar to those in Figure 19b were analyzed.

As can be seen in the plot, a decrease indeed took place near 0V from the non-annealed to the 500 ℃ condition, however, the lower slope of the IV curve after turn-on at higher voltages indicates that the series resistance rose as well. The 600 ℃ anneal condition, however, prod uces an IV curve with a lower current near 0 V and a steeper slope after turn on, producing plausible evidence that the anneal resulted in an actual decrease in parallel leakage current in the cell.

To validate the theory proposed above regarding the interplay of series resistance and parallel leakage, two diode models were created and simulated: one for a “leaky” diode, consisting of a parallel leakage component in series with a 20 Ω resistor, and one for another leaky diode in series with an 80 Ω resistor (“resistive” diode). The results of the simulation in Figure 20 show that although a general decrease in parallel leakage current seems to have taken place with the resistive diode, a large series resistance can be observed by the shallower slope at higher voltages. Since the parallel resistance in the model was not changed between the two cases, it can be said that the larger series resistance was responsible for lowering the current at lower voltages as well, verifying conclusions made with experimental data above.

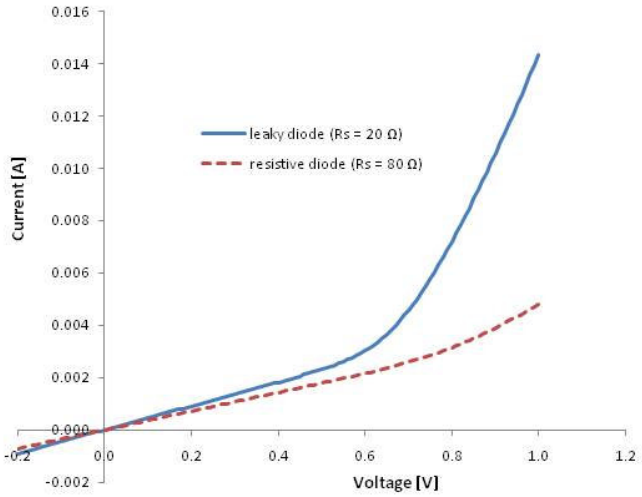

Figure 20. Simulated IV curves of modeled leaky diodes and diodes with increased series resistance, showing a decreased current even near zero bias.

The results from the anneal experiment show that although not all anneal conditions and cells showed a true decrease in parallel leakage (some actually displayed an increase in series resistance as well), the process seemed to have a positive effect on leakage, particularly for cells with lower indium concentrations which underwent anneals at 600 ℃. This has shown more promising results than other methods attempted whose experiments resulted in a failure to achieve any beneficial performance, including: rapid thermal annealing in an oxygen environment (inspired by [16]), local annealing by biasing up cells to high forward biases with probes to allow heating to occur, and boiling the cells in DD H_2O.

Passivation chemistry

Recognizing the possibility that surface electron accumulation produced many parallel leakage paths, experiments were conducted in an effort to electrically passivate the InGaN surface of solar devices. The first method involved employing chemical vapor deposition (CVD) to deposit insulating silicon nitride films on p-type InGaN. It was anticipated that dangling bonds at the InGaN surface would be capped by the SiN, preventing the surface accumulation of electrons. Samples of various indium concentrations (19, 38, and 39%) were coated with SiN while covering the metal contacts so that the devices could be measured post-process.

Figure 21 shows the leakage current density (current density measured at 0.05 V forward bias) vs. area to periphery ratio of different sized P-I-N diodes for samples containing the three indium concentrations. The area to periphery ratio (in μm) is calculated by dividing the area of the circular diodes by their circumference. This was calculated for 100, 200, 400, and 800 μm-diameter diodes.

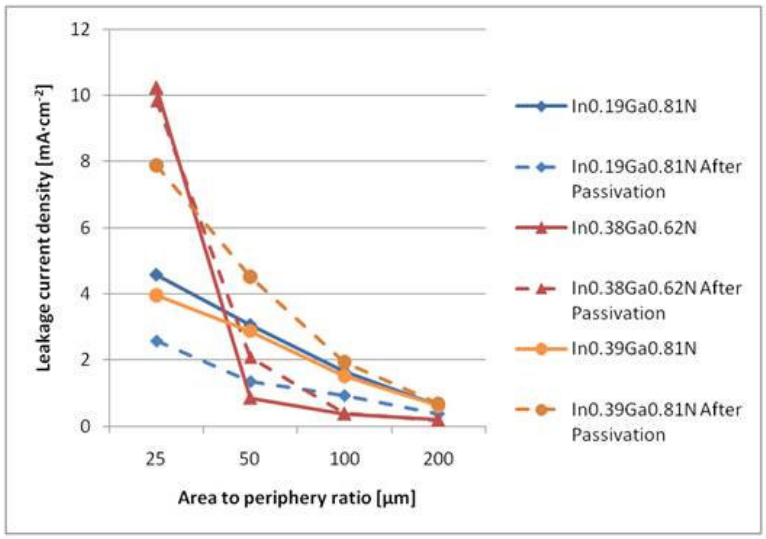

Figure 21. Leakage current of InGaN cells measured at 0.2 V forward bias for various indium concentrations, before and after passivation with a SiN film.

The downward trajectory of every curve suggests that more current travels per unit area, indicative of surface rather than bulk leakage, confirming the hypothesis that parallel current leakage originated from the electron-rich InGaN surface. Secondly, it seems that the passivation only had a positive effect for the low indium content diodes (19%), as the leakage current decreased by a factor of 50% after SiN deposition. The higher indium composition alloys actually showed an increase in leakage current after passivation. At least for smaller diodes, leakage tends to increase with Indium composition, further suggesting surface accumulation is decreasing InGaN PV device performance.

After experimenting with film-deposition-based passivation techniques, an idea arose to chemically passivate the surface of InGaN in solution, as

inspired by a study conducted by E. J. Miller *et al.,* which detailed a successful leakage current reduction through electrochemical surface treatment of MOCVD grown GaN [18]. The study indicated a blockage of leakage through line defects terminating at the surface through oxidation occurring at the GaN anode when the sample was biased in an electrochemical solution.

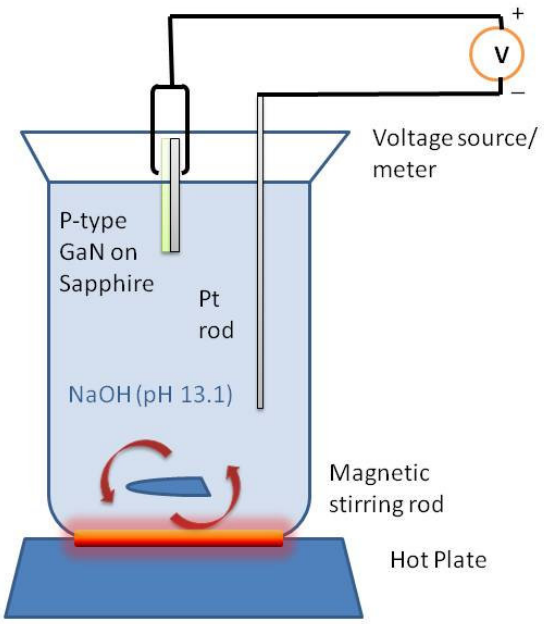

Figure 22. A schematic of the apparatus used for NaOH anodization of GaN films.

The following study attempted to show a similar reduction in leakage current for MBE-grown p-type GaN. Although most studies conducted in this thesis involve InGaN alloy-based cells, GaN was chosen because of the lack of surface electron accumulation, which would enable the ability to focus solely on parallel leakage caused by bulk defects such as dislocations. The experimental apparatus for the study is detailed in Figure 22.The p-type GaN on a sapphire substrate (with backside tungsten metal removed to prevent

shorting) was immersed into a heated and stirred NaOH solution of pH 13.1. The immersion depth of the GaN sample was controllable to a tenth of a millimeter via a precision probe controller. The GaN sample (cathode) was connected to a voltage source/meter and platinum anode. Although a full P-I-N solar structure was not present in solution, the basic electrochemical solution formed a Schottky contact with the p-type GaN, enabling a rectifying characteristic to be observed.

The results of the experiment are recorded in Figure 23. Figure 23a shows that some passivation can be observed through the IV plots from 0 to 40 min immersion time at a forward bias of 10 V. The turn on voltage actually increased after 20 and 40 minutes of immersion, without any degradation in series resistance (as evidenced by the constant slope after the turn-on voltage). However, after 60 minutes, the IV curve flattened considerably and hardly turned on.

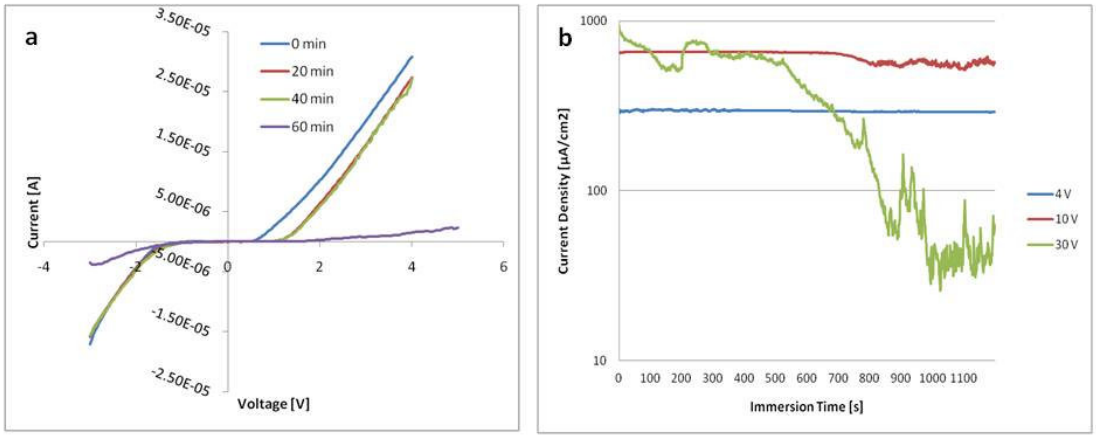

Figure 23. a) IV curves of a p-type GaN film immersed in NaOH at various submersion durations. b) Current density vs. time profiles of p-type GaN films immersed in NaOH at different voltages.

After examining the sample at multiple points in time, a notable discoloration was observed, indicating either an oxidation or removal of the material taking place. The current density through an identical Schottky diode as a function of submersion time at various constant voltages is plotted in Figure 23b. All plots show a decrease in current density over time, however, the effect is exacerbated at higher voltages. After comparing the surfaces of the submersed and non-submersed samples optically, it was found that the GaN material actually became eroded due to the aggressive electrochemistry. This explains the absence of a rectifying IV curve after an hour long submersion of the GaN material.

Although small, the electrochemical treatment of p-type GaN actually showed an improvement in IV characteristics, with less current leakage at lower voltages. The disadvantage of this method, however, is that the GaN is very sensitive to the highly basic solution and material can easily be eroded when subject to high voltages or long treatment times.

In summary, device studies involving experimentation with the epitaxial layer structure, annealing of samples with different metal stack and alloy compositions, and passivation techniques took place. The results of these experiments, compared with theoretical device model simulations, were able to explain the nature of the leakage and series resistance problems in GaN and InGaN photovoltaic devices, however, successful mitigation of these negative effects has not yet been demonstrated. Experiments in this device study nevertheless showed some evidence that it is possible to reduce some surface and bulk leakage phenomena for some cells.

Materials studies

The previous results made it apparent that understanding the InGaN material system more, rather than making improvements to the device, was necessary to recognize a path to higher efficiency cells. The following study encompasses experiments detailing the microstructural origin of leakage in nitride-based cells, as well as the effect of substrate choice on nitride PV performance.

Effect of grain structure on performance and consistency

This study focused on reporting improvements to GaN photovoltaics, and addressing the physical origins of leakage in an effort to develop better growth methods or processing treatments for higher performance nitride solar cells and other optoelectronic devices. Although an eventual merge between ternary alloys of different composition (such as InGaN) in a multi-junction cell is necessary to efficiently cover the solar spectrum, the high leakage within single, ternary-based cells still yields poor performance. The relative higher quality of binary nitride alloy growth makes for a clear case to first study GaN to elucidate a microstructural origin of leakage and later apply that approach to studying InGaN alloys.

A variety of wafers have been grown in an attempt to duplicate the performance of a GaN P-I-N material structure (Wafer 1). A significant variation in performance was discovered on the same wafer for the subsequent growths. A statistical study of GaN 100 μm diodes comparing the first and second growth attempt (Wafers 1 and 2) is depicted in Figure 24. Whereas devices processed under Wafer 1 mostly produced leakage currents

at low voltages with little statistical variation (Figure 24a), up to three orders of magnitude difference in leakage current density across 36 diodes existed for Wafer 2 (Figure 24b). Upon first examining relationships between the leakage current and device position, or leakage current and surface micro-defect density, no consistent correlation appears (micro-defects refer to circular, micron-sized defects observed via optical microscopy, which exist on the surface of the material and are usually separated by hundreds of microns).

This sample in particular exhibited the highest leakage current on average out of the different growths investigated. The nature of the IV curves reveals that there is a sub-bandgap, diode like behavior for large current densities. The change in slope of Log (I) vs. V while approaching lower voltages indicates that there may be lower energy levels in the band contributing to current flow in parallel.

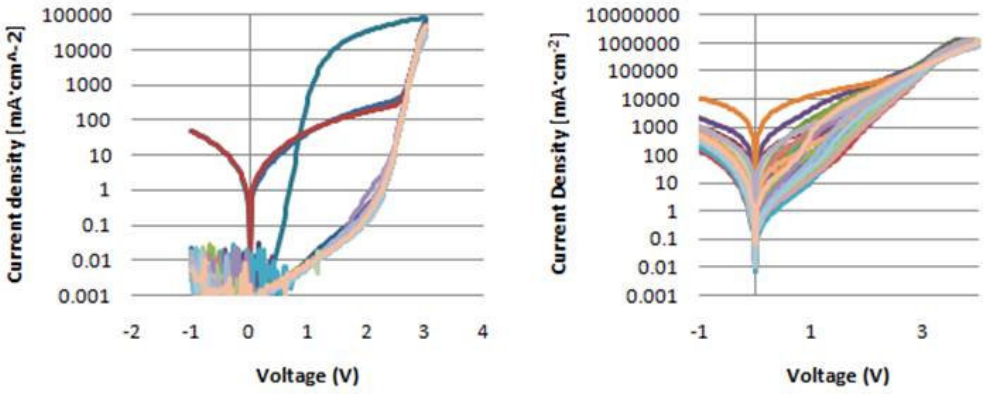

Figure 24. Variation in log IV curves for various GaN P-I-N structure diodes on Wafer 1 Process B (left) and Wafer 2 (right).

The three curves displaying abnormally high leakage in Figure 24 exhibit characteristics of devices which experience significant parallel leakage

(whether along the surface edge of the device or through dislocation cores traversing the lattice) and possibly some distributive resistance. To demonstrate this effect, a standard diode model was constructed, in which a diode existed in series with a resistor in a circuit. The model was then modified by adding a resistor in parallel to represent parallel leakage, as well as a resistor connecting the two to simulate distributed resistance (see Figure 13 (w/ diode model)). The results are plotted in Figure 25. As can be seen, the ideal diode turns on from negligible current to high current over a few tenths of a volt and then increases steadily. The leaky diode, modeled by the parallel resistor and distributive resistor, however, jumps immediately from zero to a high current before reaching any sort of turn on voltage.

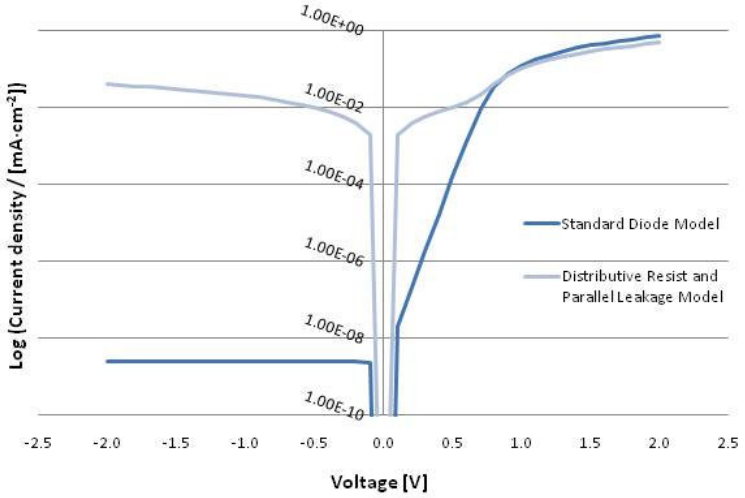

Figure 25. Modeled IV curves of ideal diode behavior vs. diodes with parallel leakage and distributive resistance components.

This result mirrors that of the statistical occurrences of leaky diodes in GaN (pictured in Figure 24, left). The variation can be more clearly observed when comparing the IV performance of various photovoltaic cells on the same wafer under both light and dark conditions (Figure 26). The cusps at multiple

voltages ranging from 2.5 V and below on seemingly identical devices suggests the presence of a range of diode-like components containing bandgaps lower than that expected for GaN.

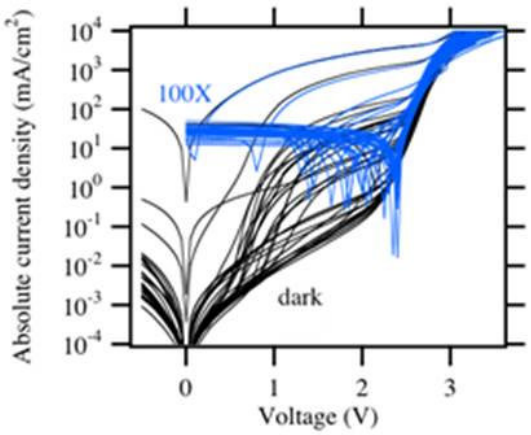

Figure 26. Variation in IV curves between several PV cells processed on the same device under both 100x concentrated sunlight and dark conditions.

To determine the dominant type of leakage in GaN solar cells, an array of circular diodes varying in size from 100 to 800 microns are fabricated on the material. Figure 27 presents the IV characteristics of each size diode near 0 V, where parallel leakage sources dominate. It is clear from the plot that leakage current density increases with diode size, or alternatively, the area to periphery ratio. This signifies more current traveling through a smaller periphery, indicative of bulk leakage taking place (the opposite of what was seen in InGaN structures). Consequently, surface leakage along the mesa sidewall of the cells does not contribute to the majority of leakage. Due to mismatch

between the GaN epilayers and c-plane sapphire substrate, threading dislocations are present and could provide a direct parallel leakage path. Although the leakage taking place may be due to a bulk phenomenon, examining the surface with AFM topography provides some clues about the underlying microstructure.

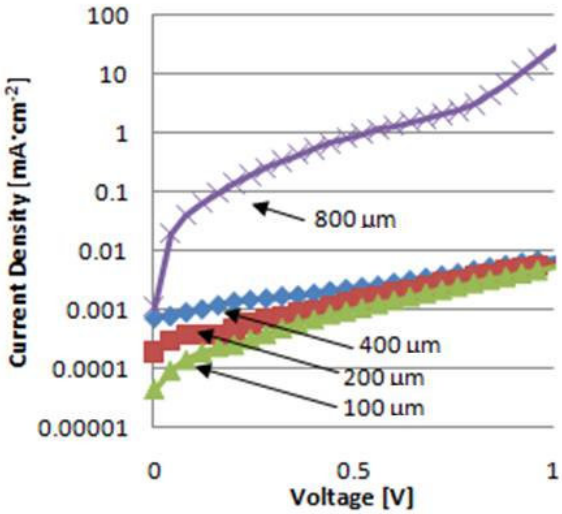

Figure 27. GaN P-I-N diode IV characteristics for Wafer 1, Process A. Each IV curve corresponds to a different sized diode.

Given that variation of growth on the surface is present between wafers and each set of the diodes measured reveal orders of magnitude leakage current, it's likely that material quality significantly affected leakage somehow. Upon examination of RMS surface roughness as measured by AFM, very weak to even negative correlations appears between roughness and leakage current density. Rather, leakage current correlated with grain size. Figure 28 (a-c) shows AFM images of three wafers with a nearly identical GaN p-i-n solar structure. The progression clockwise from the top left shows a

diminishing average grain size of the GaN epilayer. Figure 28d indicates an increasing leakage current density in the same order, suggesting that the decreasing grain size was responsible for the increase in leakage current. This is consistent with the interpretation that smaller grains contribute to larger interfacial areas between grains. As the interfaces were defects, they may

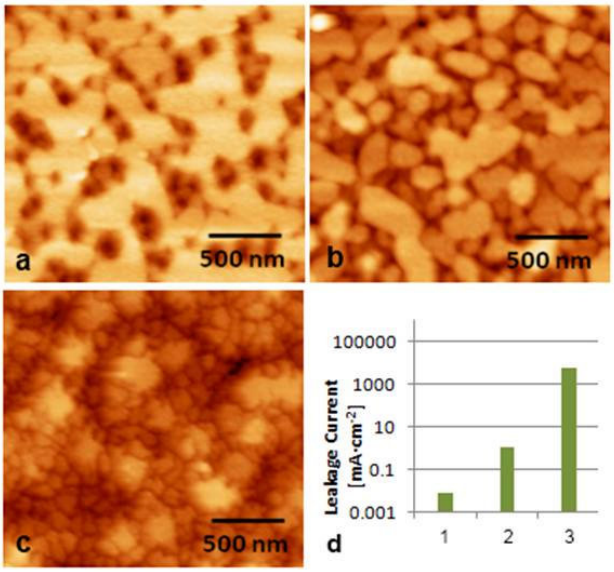

Figure 28. AFM images depicting GaN film grains of a) Wafer 1 Process B, b) Wafer 2, and c) Wafer 3, and d) corresponding average leakage currents

have attracted Ga-rich depositions, became donor-like in character, or otherwise provided a bulk parallel leakage path for carriers. It is important to note that the material was not annealed prior to the measurement, so the values recorded are representative of as-grown material (no smoothing or grain coarsening).

The data does not provide a conclusive indication that leakage correlates with roughness. The wafer with the largest average leakage of 5980 $mA \cdot cm^{-2}$ exhibited an average roughness of 52 Å, while wafers with relatively lower leakage current densities (1.09 and 0.01 $mA \cdot cm^{-2}$) recorded RMS roughness values between 9.9 and 10.9 nm, respectively. The average roughness remained the same before after etching for initially smooth-surface samples, whereas the roughness increased on average for an initially rough sample. The point that surface roughness could be viewed as defects leading to scattering or trapping of carriers and leading to leakage, suggests that a correlation between surface roughness and leakage current is plausible, although more evidence would be required to prove this. This observation indicates that roughness originates during the growth process and may be exacerbated by plasma processing.

Effect of substrate on performance

Due to the strong presence of defects in nitride semiconductors and their disastrous effects to PV performance, an investigation took place to see how performance varied across InGaN growths on different substrates. Substrates are important because they comprise different crystal structures, lattice constants, and thermal properties: all of which directly affect the formation of defects in thin films (see Appendix). InGaN lattice constants, as pictured in Figure 29, span from those of InN (3.525 Å) to GaN (3.189 Å) depending on the indium and gallium composition of the alloy.

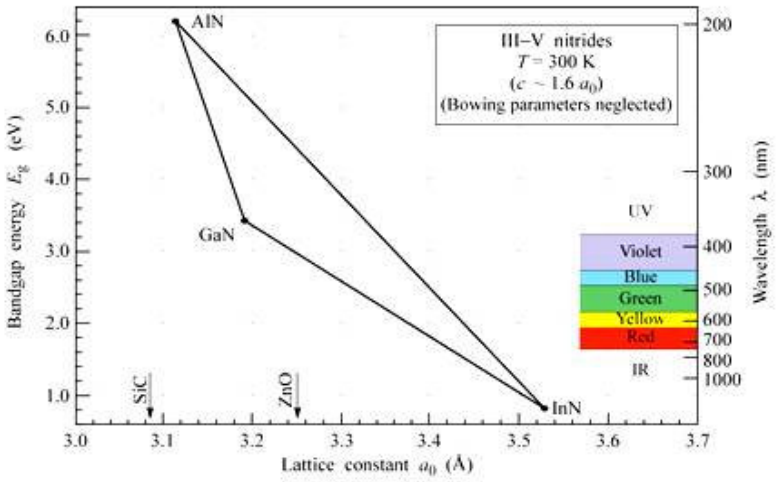

Figure 29. Band gap and lattice constant information for GaN, InN, AlN, and their alloys [19].

Table 1 presents the substrates explored in this solar study as well as some relevant parameters. Sapphire is most commonly used due to its lower cost relative to bulk GaN templates and SiC wafers as well as acceptable mismatch to InGaN. Some undesirable effects for solar cell production include the low thermal conductivity, which becomes an issue when the cell becomes subjected to highly concentrated sunlight, and the necessity to grow very thick buffer layers to achieve a low threading dislocation density. Bulk GaN templates both have high thermal conductivity and no mismatch (leading to lower dislocation densities), however, command a higher price. Silicon substrates have not achieved widespread use for solar cell production at the time of writing, because of the large lattice mismatch and difference in crystal structure. The high thermal conductivity, low cost, and ability to integrate with existing widespread silicon fabrication technology, however make it an attractive candidate for solar cell production.

Table 1. Important characteristics of commonly used substrates for InGaN PV film growth [20].

Substrate	**Crystal structure**	**Lattice Constant a [Å] / mismatch to GaN**	**Thermal conductivity at 300 K [$Wm^{-1}K^{-1}$]**
Sapphire	α (0001)	4.758 / $\sqrt{3}$ / 13%	42
Bulk GaN (template)	Würtzite (0001)	3.189 / 0%	130
Silicon	FCC (111)	5.4301 / 17%	148

Figure 30 presents IV profiles of InGaN (left) and GaN (right) solar cells for both bulk-GaN template- and sapphire-based substrate growth. It can be clearly observed that the InGaN IV performance on the GaN substrate exhibits a higher series resistance (as indicated by the shallow slope and lower magnitude than that of the sapphire substrate growth) and no turn-on characteristic, as indicated by the gradual, rounded increase in current (note that it is a log plot). The corresponding growth on the sapphire substrate, although exhibiting leakage as well, still displays somewhat of a turn on characteristic as can be seen by the change in slope at approximately 1 V. The GaN solar cell results indicate a degradation in performance for GaN-template based growths as well. The template-based growth produced a parallel leakage current three orders of magnitude higher than the cell grown on sapphire.

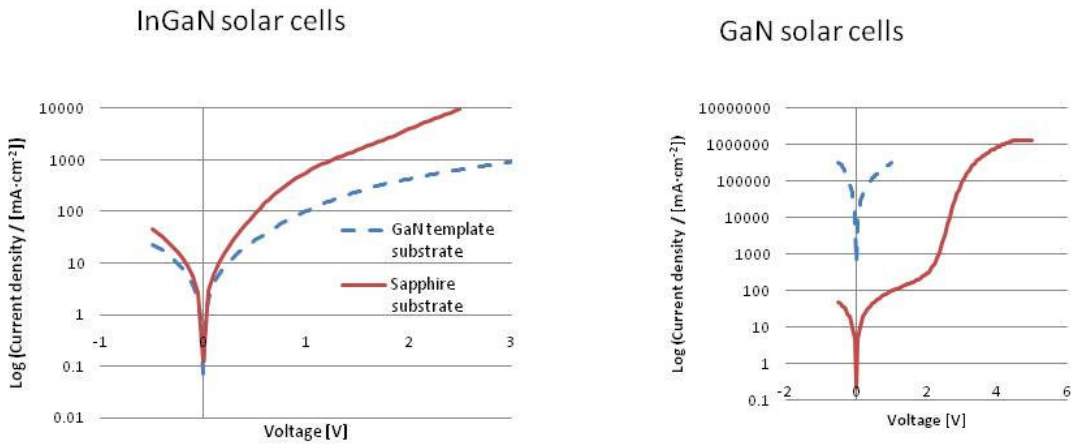

Figure 30. A comparison of IV performance of IV performance between GaN template substrate-based (dashed) and sapphire substrate-based cells (solid) for $In_{0.2}Ga_{0.8}N$ (left) and GaN solar cells (right).

The poorer performance on GaN compared to sapphire substrates is an unexpected result considering that the crystal structure and lattice constants of the bulk-GaN templates are much better matches for the solar cell films grown.

A similar comparison took place between p-type InGaN on n-type (111) silicon and the standard P-I-N structure in InGaN on a sapphire substrate, whose results are displayed in Figure 31 (left). The results show that the 20% In InGaN cell on silicon produced very small leakage and produced a very sharp turn on voltage, close to that of an ideal diode. This result came as a surprise when considered in the context of the performance of sapphire-based cell, as the crystal structure of the InGaN cell would be worse on silicon than sapphire. However, as can be seen, the sapphire-based cell displays much more leakage and an inferior turn-on characteristic.

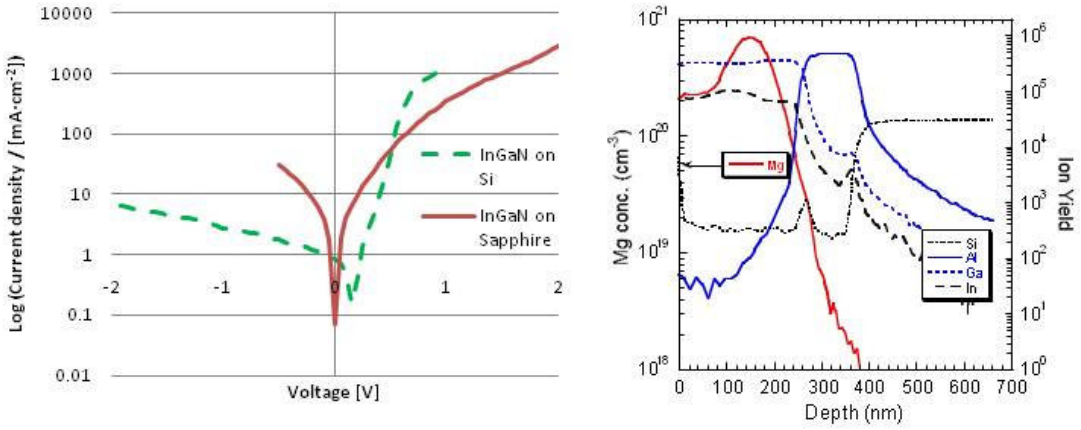

Figure 31. A comparison of IV performance between $In_{0.2}Ga_{0.8}N$ cells on sapphire vs. silicon (left), and a corresponding SIMS profile for an InGaN on Si solar cell layer structure (right).

The suspicion with regard to superior performance of InGaN on silicon vs. sapphire led to a deeper investigation into the layer structure. A secondary ion mass spectroscopy (SIMS) analysis featured on the right side of Figure 31 provided an interesting piece of information. It can be observed that the Al profile penetrates deeply into the silicon profile beginning at approximately 400 nm below the surface of the wafer. This profile, corresponding to the AlN buffer layer used to form a growth template for InGaN on highly mismatched silicon, seems to show a strong presence of aluminum right at the interface of the silicon substrate. Aluminum, being a group III element in the periodic table, is a known acceptor in silicon. Consequently, the silicon became unintentionally doped p-type, forming a P-N homojunction in silicon at the interface, rather than a p-InGaN-n-Si heterojunction expected. Thus the desirable IV characteristic observed arose from silicon and not InGaN. The short conduction path of electrons through the highly defective InGaN material effectively transformed the InGaN layer into a series resistor. Because AlN is an important buffer material to ensure acceptable InGaN crystal quality on

substrates such as silicon, and since it must be grown at high temperatures, the diffusion of aluminum into silicon to form a P-N homojunction is unavoidable. Although at this time few P-I-N InGaN structures have been made on n-Si substrates, perhaps future experiments can be conducted to observe if successful InGaN cell on Si performance can be observed.

Conclusion

Despite their promise of high efficiency and durability, growing and producing efficient InGaN and GaN based PV cells have proven to be a challenging endeavor. InGaN solar cells with absorbance properties at different wavelengths of the solar spectrum were grown and fabricated and tested under dark conditions and under concentrated sunlight. Although the results of GaN cells appear to be very promising, the addition of indium to form InGaN results in cells with significant parallel leakage, whose source has been identified to be among grain boundaries, dislocations, and short conduction paths caused by surface electron accumulation. A comparison of experimental results from InGaN cells to simulations from modeled diode systems revealed that distributive resistance experienced by carriers in InGaN as well as series resistance caused by interfacial contact resistance are also important detriments to performance.

Based on these findings, device and material experiments took place to explore methods to mitigate such detrimental effects. Experimental results from electrochemical, thermal, and CVD-based device treatments to nitride based material provided slight improvements to solar IV performance, however, not on the scale required to produce efficient solar cells. Furthermore, material studies investigated the microstructural origin of leakage

by comparing statistical leakage variation among several diodes on multiple GaN wafers. The study concluded that leakage current is inversely correlated with the size of grains in GaN films, indicating that grain boundaries are a large source of leakage in nitride cells. Lastly, an analysis of nitride-based PV cells on various substrates outlined the advantages and disadvantages of using each substrate as a solar cell material.

The author wishes to emphasize the difficulty in achieving satisfactory solar cell performance from nitride-based materials. The poor leakage and resistance characteristics of current cells cause the cells to not behave like standard devices, making it difficult to extract useful information from performance data, given current models. Currently leakage is only beginning to be understood, and its effect due to defects and surface phenomena must be investigated with greater depth, to the point where a physical understanding of the chemical and electrical effects of these elements, and methods to passivate or eliminate their formation, is achieved. Moreover, p-type conduction in InGaN at higher compositions of InGaN has not yet been realized and is critical to successful IV performance. The formation and measurement of p-type InGaN with larger hole densities and mobilities, particularly at higher indium concentrations, must be realized. Currently these are the major challenges that stand in place of this otherwise ideal material for terrestrial solar power generation. Before this technology even nears commercialization the two problems of leakage and truly p-type InGaN production must be achieved.

II. GALLIUM NITRIDE HEMTS

Background

High electron mobility transistors (HEMTs, a.k.a. “HFETs”) work as switches and signal amplifiers for high voltage and high frequency applications. The unique layer combination of different materials allows for the formation of a highly conductive electronic channel called a two dimensional electron gas (2DEG). Because of the high breakdown voltage, high band gap, and the polarization properties of GaN, a combination of GaN and AlGaN layers are typically used to produce high performance HEMT devices such as the one pictured in Figure 32. In a HEMT, electrons flow from a source contact (S) to a drain contact (D) when a voltage is applied between the two, through a very low resistance 2DEG that forms at the interface between the AlGaN and GaN layers. The amount of current flowing through the channel is modulated

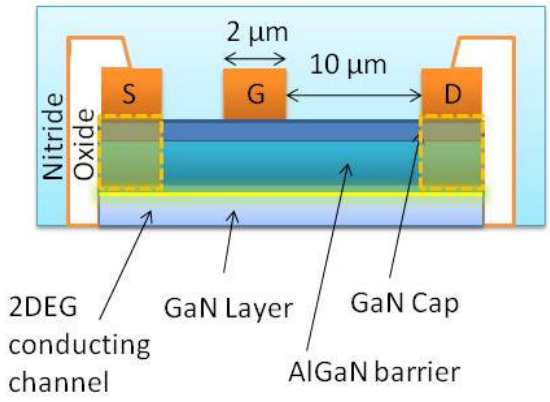

Figure 32. Cross-sectional diagram of a typical AlGaN/GaN HEMT device, with bright-yellow areas indicating regions of current flow.

by the gate (G) voltage. In a “normally-on” device such as the one pictured, current will flow between the source and drain as long as a voltage is applied between the source and drain contacts, even if no voltage is applied at the gate. Biasing the gate to a negative voltage that is less than the “pinch-off voltage,” V_{PO}, will close the 2DEG channel, effectively switching off the device.

Alternatively, the gate voltage can be raised to increase the amount of current traveling between the source and drain by increasing the density of carriers in the 2DEG. The unique properties of the HEMT materials and layer structure detailed above allow it to act as both a high power switch and a microwave power amplifier.

Equally important as the high breakdown voltage and band gap of GaN and its alloys are their electric polarization properties. The unique electric polarization characteristics of these materials alter the band diagram in such a way to produce the very important 2DEG (this will be covered in more detail in subsequent sections). As the inset in Figure 33a shows, GaN is an ionically bonded solid with a net dipole moment pointing in the direction of spontaneous polarization, P_{SP}. Since most high quality growth (via both MBE and MOCVD) is oriented in a “Ga-face” orientation (as illustrated in Figure 33a), the vector of spontaneous polarization points upward (away from the surface). The formula for calculating the magnitude of spontaneous polarization in $Al_xGa_{1-x}N$/GaN heterostructures is as follows [21]:

$$P_{SP,Al_xGa_{1-x}N/GaN}(x) = (-0.052x - 0.029)\ [Cm^{-2}]$$

where *x* is the concentration of Al in AlGaN.

In addition to spontaneous polarization, piezoelectric polarization occurs due to the displacement of the GaN and AlGaN lattices when epitaxial growth of the latter material on the former material occurs. Since a lattice mismatch between the two materials exists, the cation and anion sublattices become displaced, producing an electric dipole moment due to the change in charge separation, denoted as P_{PZ}. The equation for the piezoelectric polarization is presented below [22]:

$$P_{PZ} = 2\frac{a-a_0}{a_0}\left(e_{31} - e_{33}\frac{C_{13}}{C_{33}}\right)$$

where a and a_0 are the lattice constants of GaN and $Al_xGa_{1-x}N$, respectively, and C_{13} and C_{33} are the elastic constants, and e_{31} and e_{33} are the piezoelectric constants, all of which are given by the following equations [23,22,24,25,26]:

$$a(x) = (-0.077x + 3.189) \cdot 10^{-10}\ [m]$$

$$C_{13}(x) = (5x + 103)\ [GPa]$$

$$C_{33}(x) = (-32x + 405)\ [GPa]$$

$$e_{33}(x) = 0.73x + 0.73\ [Cm^{-2}]$$

$$e_{31}(x) = -0.11x - 0.49\ [Cm^{-2}]$$

Once the piezoelectric polarization vector, P_{PZ}, is determined, it can be added to the spontaneous polarization vector, P_{SP}, to determine the net polarization, P. Notice in Figure 33a, that for AlGaN/GaN

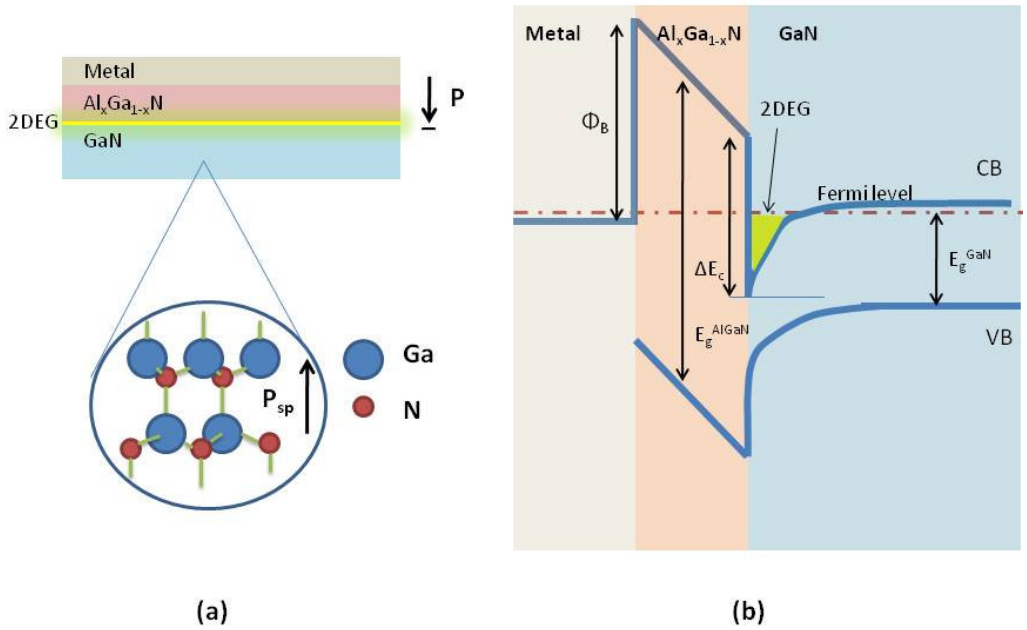

Figure 33. a) Layer structure of an AlGaN/GaN HEMT depicting net polarization vector P and an inset showing a Ga face GaN lattice and spontaneous polarization vector. b) Electronic band diagram for an AlGaN/GaN heterostructure at zero bias (not to scale).

heterostructures with Ga face epitaxial growth, the polarization vector points downward (according to the convention used in this study), causing free electrons to become confined below the surface at the AlGaN/GaN interface. Figure 33b depicts the band diagram of the same heterojunction. Proceeding from left to right, it can be seen that a Schottky barrier creates an instantaneous jump in the conduction band (which is a function of the difference between the metal and AlGaN work functions). The net polarization

as described above exerts an electric field that causes the bands to bend down such that the conduction band is close to the Fermi level, E_F at the heterojunction. The energy band offsets and differing band gaps between the two materials causes the conduction band to instantaneously drop below and then gradually rise toward the Fermi level. Consequently, a small triangular quantum well forms at the interface and allows electrons to accumulate at the interface, forming a thin conducting sheet also known as a 2DEG, and is typically 25 Å in thickness.

Having electrons conduct through a confined channel is advantageous because it eliminates the need for carriers to travel through the lattice (as they do in other transistors such as MOSFETs), in which they can easily become scattered by lattice atoms. Furthermore, it eliminates the need for doping [3], in which precise doping profiles are difficult to achieve, and ionized impurities can contribute significantly to scattering, thereby reducing mobility and current density.

The quantum well/2DEG characteristics can be greatly controlled by altering the gate voltage. Since the HEMT gate structure featured in Figure 33b forms a “normally-on” or “depletion-mode” device, a 2DEG exists without an applied voltage at the gate. As the gate is biased to an increasingly negative voltage, the electric field through AlGaN decreases in magnitude, causing the depth of penetration of the triangular well to lessen until the pinch off voltage, V_{PO}, is reached, at which point a 2DEG no longer forms and the channel no longer passes current. If the gate voltage is instead made more positive, the electric field steepens, deepening the triangular energy well. This in turn raises the number of available energy states for carriers traveling

through the 2DEG and increases the carrier sheet density, which contributes to an increased current for a given drain-source voltage.

As can be observed by the above discussion, HEMT performance is largely influenced by engineering the conduction band through layer structure optimization. The key to producing large current for high power operation is providing a high polarization field such that the triangular quantum well is highly confined at the interface while providing a high sheet charge. This design feature must be considered along with other parameters: Firstly, the lattice mismatch between AlGaN and GaN allows for a limited growth thickness of AlGaN before the lattice grown on top relaxes, forming cracks which prevent current flow. Secondly, a steep conduction band profile through the AlGaN layer could encourage electron tunneling through the thin Schottky barrier, producing unwanted gate leakage current. The necessary balance between these parameters causes HEMT design to become an optimization problem.

Optimization of power switching transistor design

Design

High-electron-mobility-transistors (HEMTs) are very important for high power switching applications such as switching mode power supplies and inverters [27,28]. To enhance these applications however, certain characteristics must be optimized. For power switching, a high breakdown voltage is desirable to allow the device to work at higher power without failing [29]. To do this it is necessary to suppress buffer leakage and maintain a low on-resistance, which also provides faster switching and lower losses [30].

AlGaN/GaN heterostructures are very attractive because of the high electron mobility in the 2D electron gas as well as the large critical electric field that they provide. In this study, molecular beam epitaxy (MBE) is employed to grow HEMT material because of the ability to grow abrupt junctions of precise thickness, with low dislocation densities, and high purity material (eliminating the necessity to back-dope GaN buffer layers to prevent buffer leakage during device operation [31]).

Several strategies were employed in the HEMT layer design to increase performance. The first goal was to achieve higher current in the 2DEG, which involved two factors: better confinement of the 2DEG to the heterojunction interface to decrease scattering and increase mobility, as well as increasing electron sheet density in the 2DEG. To realize these factors, a high

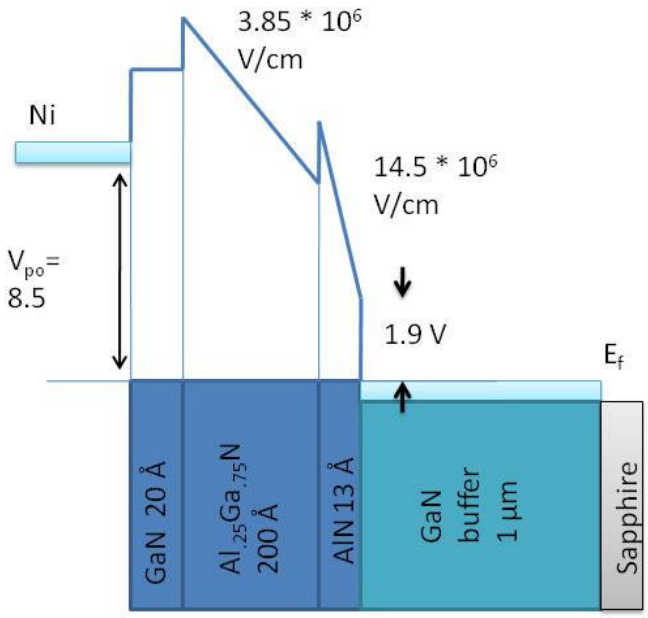

Figure 34. Band structure of optimized design of AlGaN/GaN HEMT with GaN cap and AlN interbarrier layer.

polarization field to bend down the conduction band and form a deeper and narrower triangular well would be required. Figure 34 shows the layer structure and conduction band (at pinch off conditions) of the optimized HEMT in this study. The initial composition of AlGaN on top of GaN was chosen to be 100% Al, because of the strong polarization field of AlN (14.5 x 10^6 V·cm^{-1}) which contributes to a higher sheet density [32].

However, because of the large lattice mismatch between AlN and GaN, the critical thickness of the AlN layer was very small. To avoid cracking and threading dislocation formation, the AlN layer thickness was set to only 13 Å. It is desirable to grow thicker barrier layers to increase the sheet charge density [33], however, the fact that thickness is limited by critical thickness and that the threshold switching frequency decreases due to the increased capacitance of the larger thickness, a balance must be struck for these two competing factors. Because of the low critical thickness of AlN, the barrier was extended by including a 25 % AlGaN layer of 200 Å thickness in the design. Although the polarization field of 3.85 V·cm^{-1} was shallower than that of AlN, it allowed extension of the barrier thickness, resulting in a higher carrier density. Experimental and modeled data of the critical thickness of AlGaN alloys in AlGaN/GaN heterostructures is detailed in Figure 35. The critical thickness decreases with increasing Al concentration, as the lattice mismatch becomes greater, causing larger amounts of stress.

An empirical equation was fitted to the data by the author in Figure 35 by employing a hyperbolic fit:

$$t_{crit} = \frac{6.3679}{-0.0309 + x} \quad [nm]$$

where *x* is the Al concentration of the AlGaN layer on top of GaN as a decimal value between 0 and 1. The equation is only valid for AlGaN alloys with Al concentrations between 3% and 50%, outside of which the fit no longer applies.

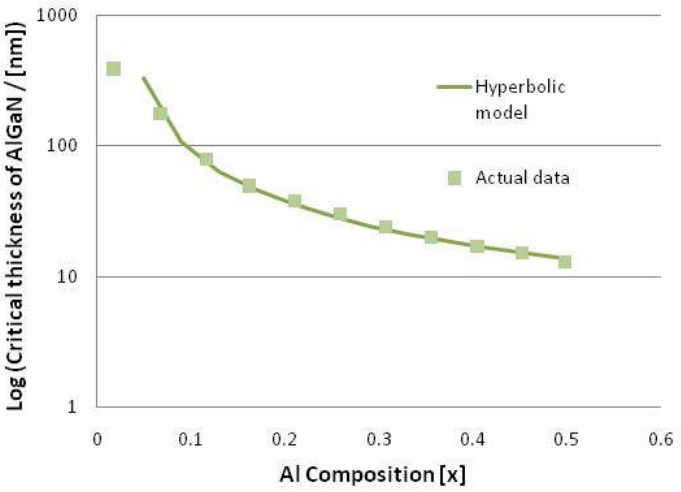

Figure 35. Critical thickness of $Al_xGa_{1-x}N$ layer grown on top of a GaN lattice as a function of Al composition, x. The squares representing actual data (courtesy of O. Ambacher and L.F. Eastman) are superimposed by a hyperbolic fit represented by a solid line.

The last design feature was the addition of a 20 Å GaN cap atop the AlGaN layer in order to reduce tunneling leakage through the Schottky barrier. By increasing the width of a barrier, the probability of tunneling will decrease, all other things equal [34].

Experiment

Once the design was completed, the HEMT layer structure was grown and processed into devices as per the following procedure: HEMT layers were grown on 2” 6H Sapphire substrates using plasma-assisted molecular beam epitaxy (MBE). The wafers were outgassed and then an AlN nucleation layer was grown to form a template for a 0.3 µm AlN buffer layer, followed by a 1 µm GaN channel/buffer. The barrier layers were then grown, with intended parameters of AlN (13 Å), $Al_{0.25}Ga_{0.75}N$ (200 Å), and GaN (20 Å). The layers were grown at a substrate temperature of 800 ℃ as measured by a pyrometer. The Ga effusion cell was at a temperature of 970 ℃ and Al was at a temperature of 1455 ℃. *In situ* RHEED instrumentation revealed high crystalline quality during the entire growth. Following the growth, CV measurements revealed such characteristics as carrier density, barrier thickness, and pinch off voltage.

The as-grown materials were then processed to form devices. Ti/Al/Mo/Au was evaporated to form source and drain ohmic contacts. A rapid thermal annealing (RTA) process followed, at 800 ℃ in N_2 for half a minute. Then, a mesa etching step occurred in an ICP-RIE etcher using a chlorine based gas mixture ($Cl_2/BCl_3/Ar$). Transfer length measurement (TLM) features were fabricated on the chip during process to assess the quality of ohmic contacts. Measurements indicated an ohmic contact transfer resistance of 0.5 Ω-mm and a sheet resistance, R_s,of 365 Ω/□. Next, a silicon oxide layer of 400 nm thick was deposited by plasma enhanced chemical vapor deposition and then wet etched to open the device active area. The oxide layer on the mesa etched area assisted in eliminating pad-to-pad current leakage. Afterward, a

Ni/Au metal stack was evaporated and lifted off to form the Schottky gate contact. Before the SiN passivation, the device underwent annealing in N_2 at 500 ℃ for 10 minutes to stabilize the surface. Fin ally, a SiN layer of 60 nm thickness was deposited by PECVD at 300 ℃. The sou rce-gate spacing L_{SG} and gate length L_G of all the fabricated devices were 2 µm for each. The gate width W_G is (500 × 2) µm. The gate drain spacing L_{GD} is 10 µm was designed to enhance the device drain-source breakdown performance. The source and drain contact lengths were both 7 µm.

Material and electronic properties

The key electronic properties of the as grown wafer (attempting to replicate the designed HEMT structure from earlier) along with the associated layer structure is presented alongside with the corresponding elements of a non-optimized, MOCVD-grown HEMT structure in Figure 36. Although the AlGaN composition was overshot (29% grown vs. 25% expected, measured by HRXRD) the important differentiating parameters of the GaN cap, the AlN interbarrier, and the lack of C-doped GaN buffer on MBE material were present for comparison. The combination of these characteristics yielded a better mobility, sheet density, and sheet resistivity for the optimized, MBE-grown structure.

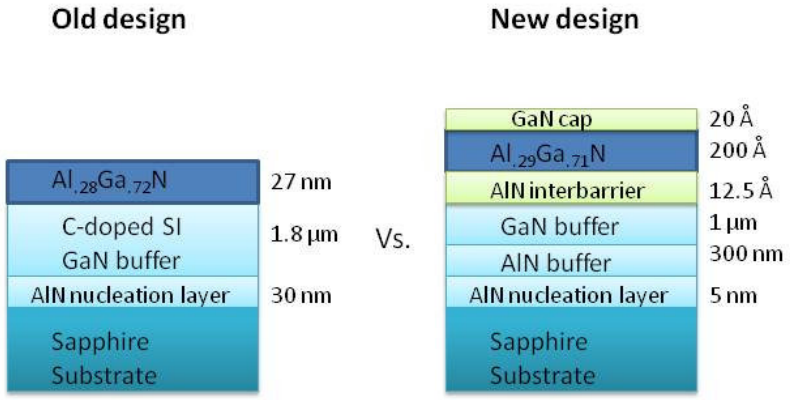

Performance metric	Old design (MOCVD)	New design (undoped, MBE)
Mobility [$cm^2V^{-1}s^{-1}$]	1448	1557
Sheet density [cm^{-2}]	$8 * 10^{12}$	$1.1 * 10^{13}$
Sheet resistivity [Ω/□]	540	357

Figure 36. A comparison of the layer structures and electrical properties of a typical (left) vs. an optimized (right) AlGaN HEMT design.

The presence of the AlN barrier with the steep polarization field allowed for better carrier confinement in the 2DEG, allowing the carriers to experience less collisions with atoms in the GaN lattice, and hence, a higher mobility. Despite the lower total barrier thickness of the new design (23 vs 27 nm), a higher carrier density of 1.1×10^{13} cm^{-2} was achieved. Lastly, the same reasons for high mobility allowed a low sheet resistivity in the 2DEG of 357 Ω/□ to be experienced.

Figure 37 shows RHEED screen images earlier (left) and several hours later (right) during growth. Initially, the bright, spotty appearance of the horizontal lines representing reflections of different crystal faces in the grown

film, indicate that the material quality was somewhat poor earlier on in the growth, likely consisting of nitrogen-rich stoichiometry and a rough surface (due to excessive etching by the ionized nitrogen). The relatively long, continuous lines on the right, however, indicate that film quality improved throughout the growth. The lines maintained their brightness, indicating that the stoichiometry was balanced rather than becoming metal-rich. A metal-rich film would have produced a much darker RHEED pattern, indicative of metal precipitation formation, which would make HEMT device fabrication more difficult and would reduce electrical performance.

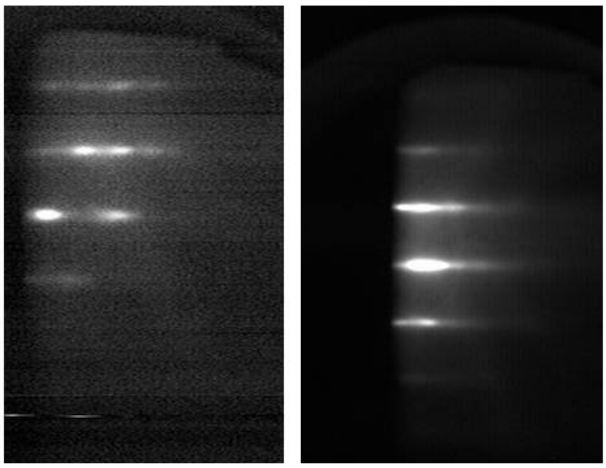

Figure 37. *In situ* RHEED images of GaN layer growth via MBE in the beginning (left) and at the end of growth (right).

The results of the capacitance-voltage (CV) measurement on the as-grown wafer (identified as GS2543) are depicted in Figure 38. Unfortunately the capacitance in Figure 38a did not drop instantaneously when the 2DEG was depleted by biasing the wafer with increasingly negative voltages. While CV data shows a final depletion of capacitance nearby at -10 V, it's difficult to

ascertain a precise pinch-off voltage. Rather, the broad (rather than vertical) decrease of the profile with negative bias indicates that the HEMT layers were of poor electrical quality and causing considerable leakage. The electron density vs. depth plot in Figure 38b shows a steep increase in electron concentration at 300 Å below the surface, indicating that the barrier width was higher than the expected value of 233 Å (calculated by summing the thicknesses of the GaN cap, AlGaN barrier, and AlN interbarrier in Figure 36).

It is difficult to explain the exact reasons for the poor performance of this material, especially considering the excellent crystal quality during growth. Besides the small deviation from the intended composition of the AlGaN alloy barrier, the only other deviation from design parameters was the overshoot of the total barrier thickness and could have been a reason for the unusual behavior of capacitance at negative voltages.

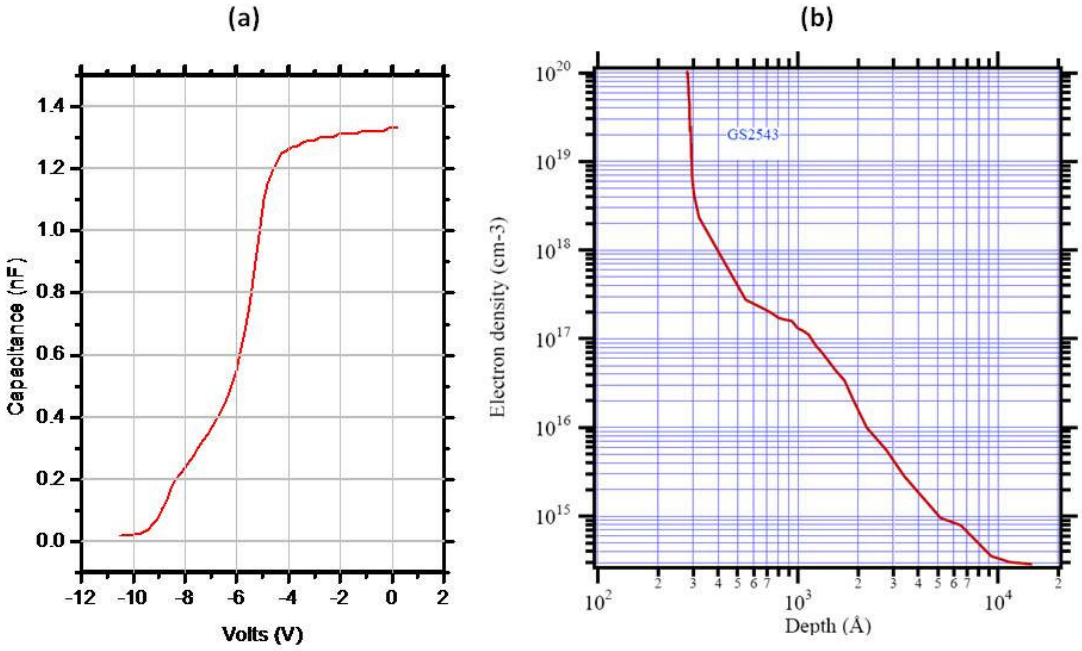

Figure 38. CV data of an as-grown $Al_{0.29}Ga_{0.71}N$/GaN HEMT wafer ("GS2543") detailing a) a CV profile, and b) an electron concentration vs. depth profile.

Thus, another wafer (identified as "GS2544") was grown in an attempt to duplicate growth conditions of the wafer discussed above, however the aim was to decrease the thicknesses of each of the layers in hopes of achieving those detailed in the optimized HEMT design.

The CV measurement of the new wafer, in Figure 39a, shows the measured characteristics of an AlGaN HEMT structure at an Al composition of 0.29. A pinch off voltage of -4 V was measured, nearly coinciding with simulated results from conduction band modelling. Figure 39b shows that the barrier thickness was 20 nm and the sheet density is 1.1 x 10^{13} cm^{-2}. Using these data along with the sheet resistivity, the high field drift mobility was calculated to be 1557 $cm^2V^{-1}s^{-1}$.

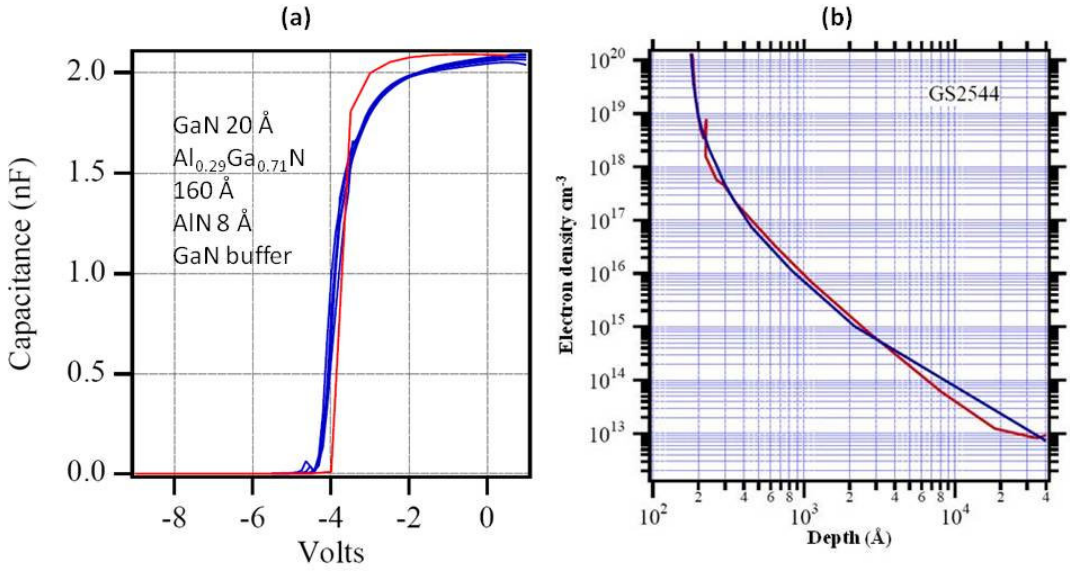

Figure 39. CV data of an as-grown $Al_{0.29}Ga_{0.71}N$/GaN HEMT wafer ("GS2544") detailing a) a CV profile, and b) a concentration vs. depth profile.

The CV data supported suggestions that buffer leakage was small, since the carrier concentration was on the order of 7 x 10^{13} cm^{-3} in the bulk, over a buffer thickness of approximately 1 µm. This translates to an equivalent sheet density of 7 x 10^{9} cm^{-2}, which is minimal compared to the 1.1 x 10^{13} cm^{-2} of the 2D electron gas. Once again, the low buffer leakage was achieved without back doping the buffer with acceptors during growth.

Device performance

The I_D-V_{DS} curves of fabricated devices are presented in Figure 40a. The current saturates at approximately 0.3 A/mm for a gate voltage of 2V. The knee current is approximately 0.3 A/mm at just over 6 V V_{DS}. Although the expected saturation current is approximately 1 A/mm for a carrier density on

the order of 10^{13} cm^{-2}, the large gate width (1 mm) induces negative feedback voltages between the gate and the source, thus leading to lower drain currents. After saturation, the drain currents drift gradually lower due to poor thermal conduction of sapphire substrates and negative voltage drops along the channel. Figure 40b displays the gate current as a function of the source-drain voltage. At a large negative gate bias of -6 V the maximum gate leakage is 1 X 10^{-3} mA/mm. This indicates that gate leakage, though present, is minimal.

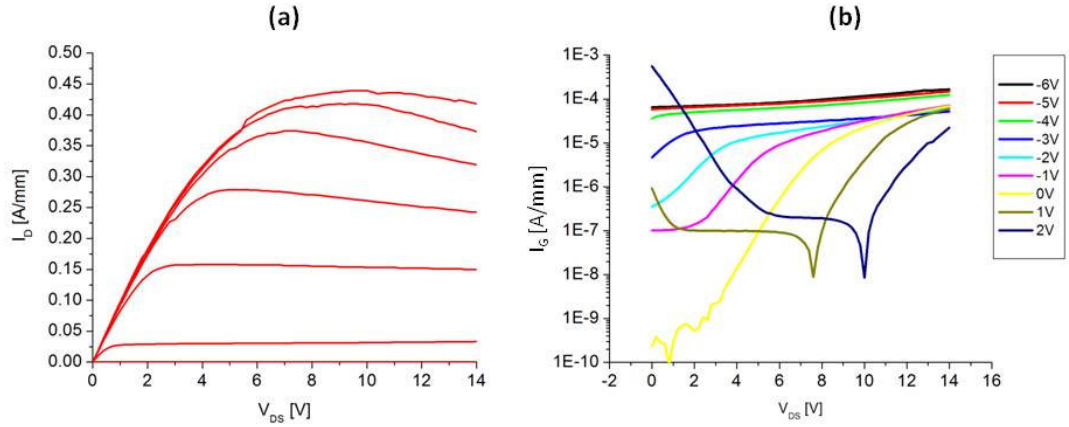

Figure 40. a) IV curves of the optimized $Al_{0.29}Ga_{0.71}N$/GaN HEMT device at various gate voltages, and b) gate leakage vs. drain-source voltage for various gate voltages (data courtesy of J. Shi).

To summarize, MBE growth of AlGaN on GaN normally-on HEMTs with an AlN interbarrier and GaN cap is demonstrated. The as-grown wafers with the optimized HEMT structure sheet yielded a sheet charge density of 1.1x 10^{13} cm^{-2} along with a mobility of 1557 $cm^2V^{-1}s^{-1}$. The addition of the AlN interbarrier assisted in increasing the sheet density as well as confining the 2DEG to the heterojunction interface. The GaN cap provided a barrier to lower tunnelling leakage through the gate. Measurements confirm that gate leakage,

although present, was minimal. Furthermore, buffer leakage seemed to be minimal within the range of measurement. The results of this study show a successful application of an optimized HEMT structure on MBE material.

Thermal characterization of RF HEMTs with RAMAN spectroscopy

Background

One significant challenge with GaN HEMTs is that the junction temperature and temperature distribution in the devices as a function of bias must be better understood to ensure higher reliability.

Common methods for identifying the temperature in HEMT devices include infrared [35], micro-Raman [36], scanning thermal microscopy [37], and liquid crystal measurements [38]. Despite the utility of infrared, thermal microscopy, and liquid crystal methods, they may not be suitable for this type of measurement due to the measurement's low resolution or tendency to change the thermal impedance of the material. The Raman technique offers submicron accuracy and does not physically interfere with the sample.

Micro-Raman thermal mapping has previously been demonstrated in GaN HEMTs [35,36,39]. Spectra taken from micro Raman thermometry reveal features associated with observable phonon modes as well as photoluminescence peaks. Phonon shifted peaks are modified with multiple parameters, including temperature, strain, and electric field [40]. The micro-Raman measurement allows for highly localized determination of temperature as the temperature distribution over the whole device can be mapped and

compared to simulated results from finite element models to validate their results. Probing the devices with shorter wavelength lasers such as a 325 nm laser can provide more surface sensitive measurement of temperature. This is ideal for probing polarization induced HEMTs, where the majority of the electron current travels through an electron sheet just below the surface.

Raman spectroscopy

Raman spectroscopy involves viewing of the spectra of scattered light from a sample subject to Raman scattering. Raman Scattering is the *inelastic* scattering of photons by phonons. Although most light irradiated upon a material is *elastically* scattered (meaning that the energy of the incident light is equivalent to that of the light scattered from the sample), approximately 1 out of 1 million photons is scattered *inelastically*. In this scenario, incident light is scattered by an excitation within the lattice due to some light absorption, causing the scattered light to change frequency. Two types of Raman scattering events are possible: Stokes and *anti*-Stokes scattering. In Stokes scattering events, the crystal lattice absorbs energy, resulting in the emission of photons of lower energy than the incident light (see Figure 41).

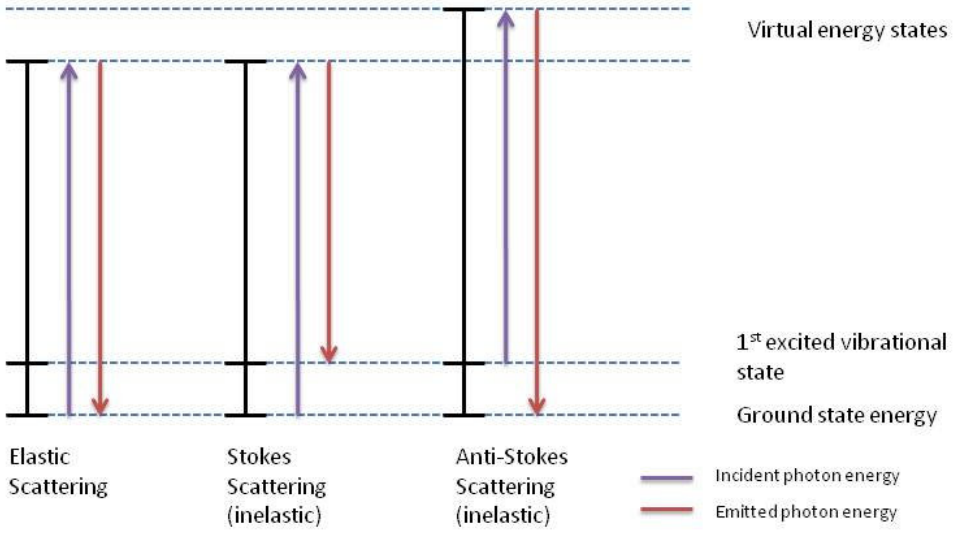

Figure 41. Diagram depicting energy transitions in elastic, Stokes, and anti-Stokes scattering events.

In anti-Stokes scattering events, the crystal lattice actually loses phonon energy due to the excitation of the lattice by incident light and higher energy photons are emitted. The energy differences associated with the changes in frequency of the scattered light are directly attributed to the energy levels of vibrational and rotational energy levels in the crystal (i.e. the various phonon modes).

Figure 42 displays the phonon dispersion curve for würtzite GaN [41]. Since the unit cell of GaN contains 4 atoms, the solid produces 12 phonon branches, each corresponding to a particular type of vibrational or rotational mode in the crystal. Two primary types of phonons exist in crystals: a*coustic* phonons (essentially *sound* waves), which have a lower kinetic energy and go to zero at zone center in the figure, and *optical* phonons, which are excited by *light*, have higher kinetic energy and are non-zero at zone center. The phonon modes observed via Raman scattering are viewable only when the incident

light geometry meet selection rules governed by crystal symmetry and scattered light polarization is in the correct orientation.

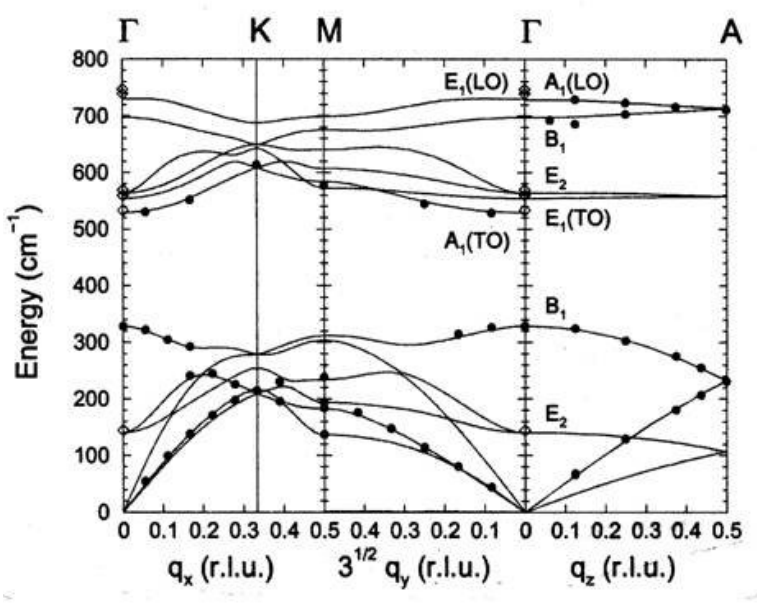

Figure 42. Phonon dispersion curves of GaN [41].

Furthermore, the measurement requires a laser notch filter to block the laser line wavelength photons from elastically scattered light and pass Raman inelastic scattering, as well as a very sensitive, cooled detector to detect the relatively small number of inelastically scattered photons.

This study focuses on the A_1(LO) photon mode and its associated resonant modes. This longitudinal optical phonon was observed at zone center (Γ) since the incident light impinges the sample at a perpendicular angle, and was expected to be observed at a peak position of 735 cm^{-1} in the observable Raman spectrum.

Because Raman scattering wavelengths depend on the vibrational energy of the lattice, a change in temperature of the crystal influences the

Raman scattered wavelength. The strain due to thermal expansion shifts the phonon modes such that the peak (in wavenumbers) of the scattered photons decreases and broadens. The equation below expresses the relationship between Raman scattered light wavenumber (ω) and temperature.

$$\omega(T) = \omega_0 - \Delta_1(\mathrm{T}) - \Delta_2(\mathrm{T})$$

where ω_0 is the wavenumber of the observed phonon mode at T=0, Δ_1 is the thermal expansion contribution to the change in scattered light, and Δ_2 accounts for the anharmonic interaction between phonons. An accurate measurement of peak shift and broadening due to changes in temperature requires maximum precision and extensive calibration, which is the focus of this study.

A particularly unique aspect of this study is the observation of temperature changes for higher order phonons, which occur due to resonance effects from incident photons having a larger energy than the band gap of GaN. Other studies have examined just the first phonon mode [42,43], however, the resonant modes display higher sensitivity to temperature and are thus central to this study.

Although it is not common to see the resonant modes, Raman spectra recorded from GaN material shows up to five resonant modes, as Figure 43 illustrates. Each of the peaks labeled above 700 cm^{-1} are $A_1(LO)$ resonant (higher order) phonon modes. The presence of resonance is reflective of strong polarization in the ionically bonded GaN lattice. The shaded area of the spectrum is the superposition of sharp Raman $A_1(LO)$ peaks upon a broad GaN photoluminescence peak.

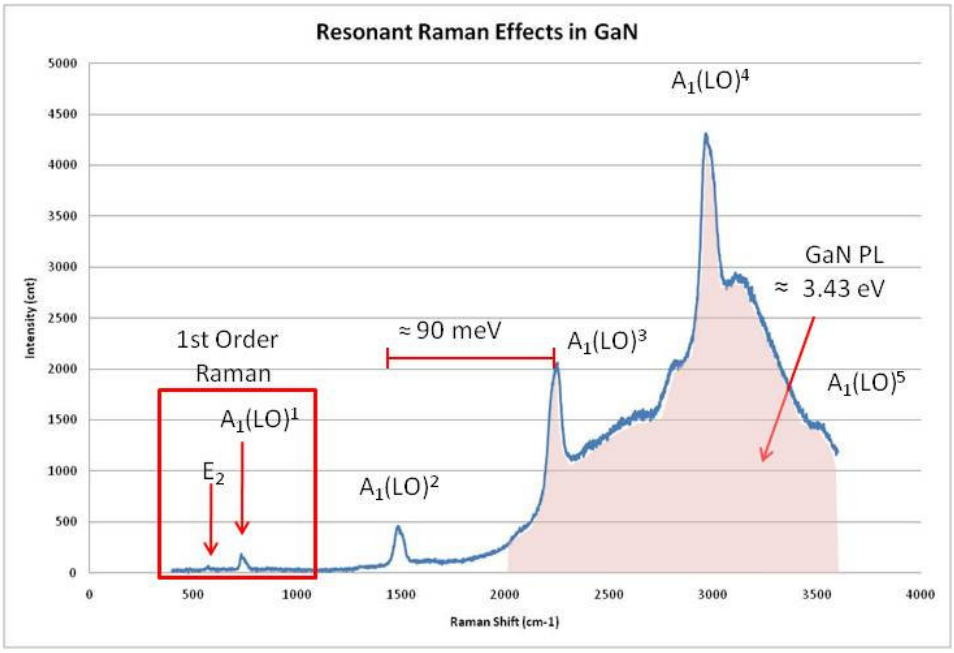

Figure 43. The Raman spectrum of GaN, depicting the Raman peaks associated with both the E_2 phonon mode and the $A_1(LO)$ mode and its related resonant modes.

Figure 44 (left) illustrates the experimental setup for Raman thermal measurements. First a laser irradiates the HEMT surface at a perpendicular angle to the surface. The photons in the monochromatic energy beam penetrate the sample to some extinction depth at which many photons are

absorbed and may cause Raman scattering. The extinction depth (or absorption length) is defined as the depth from the surface at which the intensity of the incident light decreases by a factor of 1/e. Since the Raman scattered light has a different wavelength, it also has an extinction depth beginning at the extinction depth of the incident light and extending toward the surface. Figure 44 (right) plots the extinction depths for 325 nm incident light passing through 25% AlGaN and GaN. The AlGaN extinction depth remains deeper than 50 nm despite an increase in temperature above 150 ℃ where $Al_{0.25}Ga_{0.75}N$ starts absorbing 325 nm light. This indicates that light always passes through the AlGaN layer and absorbs in the GaN. Since the photon energy of the laser is always above that of GaN, the extinction depth remains at 50 nm below the surface, which is the approximate depth at which the 2DEG exists. Since most heat generated due to current flow may originate from the high current density of the 2DEG, the 325 nm laser was chosen as an ideal source for surface-sensitive Raman thermal measurements.

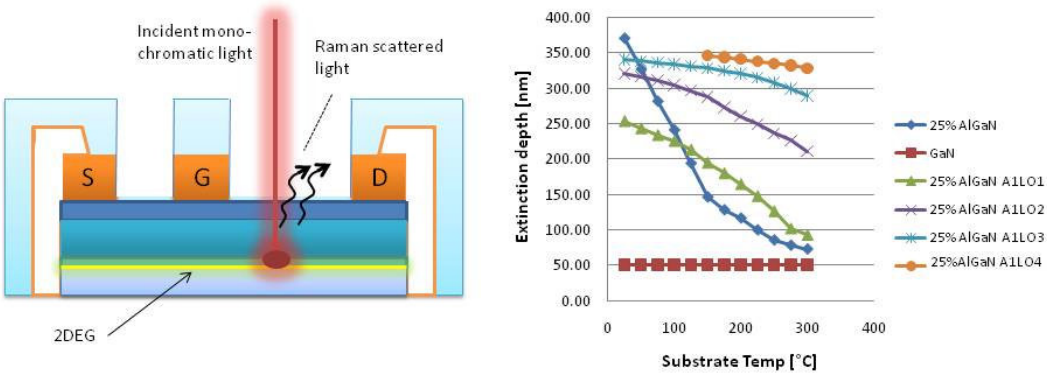

Figure 44. An illustration of the Raman scattering process near the 2DEG of an AlGaN/GaN HEMT (left), and extinction depths of both incident and scattered light from the various phonon modes.

The extinction depths for different resonant phonon modes are also plotted in Figure 44. The extinction depths become progressively higher for each order of increase in resonant mode for a given temperature, since the Raman scattered photons for higher order resonant modes are characterized by higher wavelengths. The lowest extinction depth occurs at the lowest order phonon mode, at a value barely below 100 nm. Since this is longer than the 50 nm required path length for the photons to exit at the device surface and reach the detector, Raman-scattered light for each resonant mode is detectable in the $Al_{0.25}Ga_{0.75}N$/GaN HEMT structure used for this experiment.

Experimental details

AlGaN/GaN HEMT layer structures were grown on 4H-SiC substrates via molecular beam epitaxy (MBE). Following growth, HEMT devices were fabricated with a 200 nm T gate and 2 µm source to drain spacing. Further details on device characteristics and performance are detailed in [44].

A Horiba LABRAM 325 nm laser micro-Raman setup was used to measure the devices. The wafer rested on a thermal chuck with 300 ℃ temperature capability and a motorized XY stage. DC probes contacted the surface during Raman measurements under biased conditions.

Raman peaks were recorded for the various A_1(LO) phonon modes from 100 to 4500 cm^{-1}. In the spectrum, higher order A_1(LO) resonant phonon peaks occurred at multiples of the $A_1(LO)^1$ peak frequency. Raman thermal measurements were taken by landing probes on the 4 finger, 200 µm periphery HEMT devices and biasing them from 0 to 15 W/mm and performing simultaneous Raman scans to see a peak shift.

Self-heating of the device under test was simulated with a quasi-2D finite element model of the active region cross-section to determine the distribution of power dissipation.

Results

Raising the base plate temperature shifted the peaks toward lower wavenumbers, decreased intensity, and increased broadening, as seen in Figure 45. It can be observed that the peaks are not symmetric and the peak position cannot be taken simply by measuring the location of the maximum, but rather it must be determined by deconvoluting the contributions from two individual subpeaks. The presence of an additional peak on the right after deconvolution is believed to be due to mixed polarization of light [43].

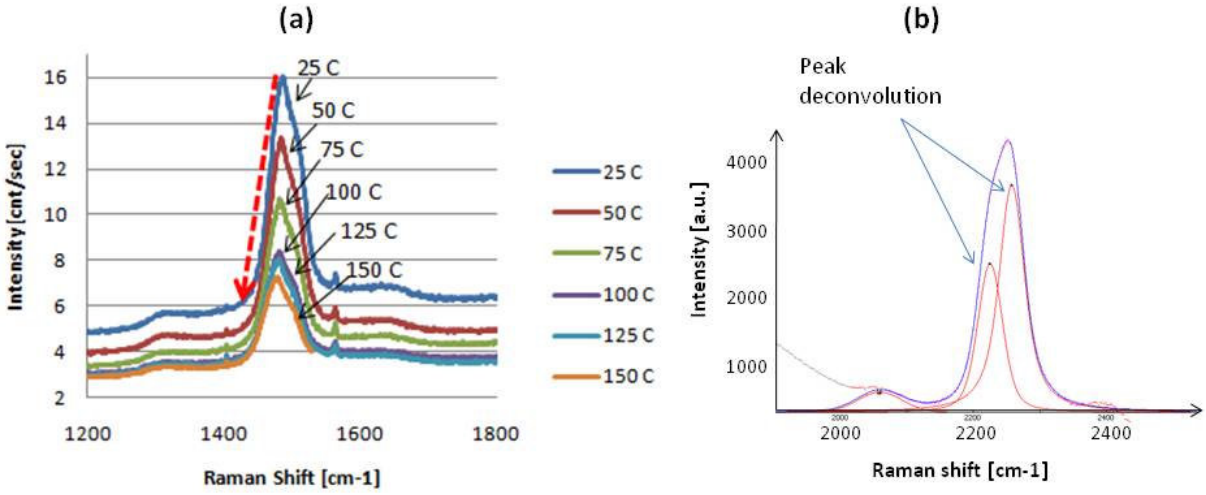

Figure 45. a) Change in position and intensity of the Raman peak associated with the second order A_1(LO) phonon mode, and b) An illustration of Raman peak asymmetry and the deconvolution into two symmetric peaks.

The shift of the left and right Raman peaks (after deconvolution of single asymmetric peaks in the Raman spectra) with temperature are

characterized for each $A_1(LO)$ phonon mode, from the base state ($A_1(LO)^1$) to the highest resonant mode ($A_1(LO)^5$) is depicted in Figure 46 (while the device was unbiased). As expected, both the left and right peaks decrease in wavenumber

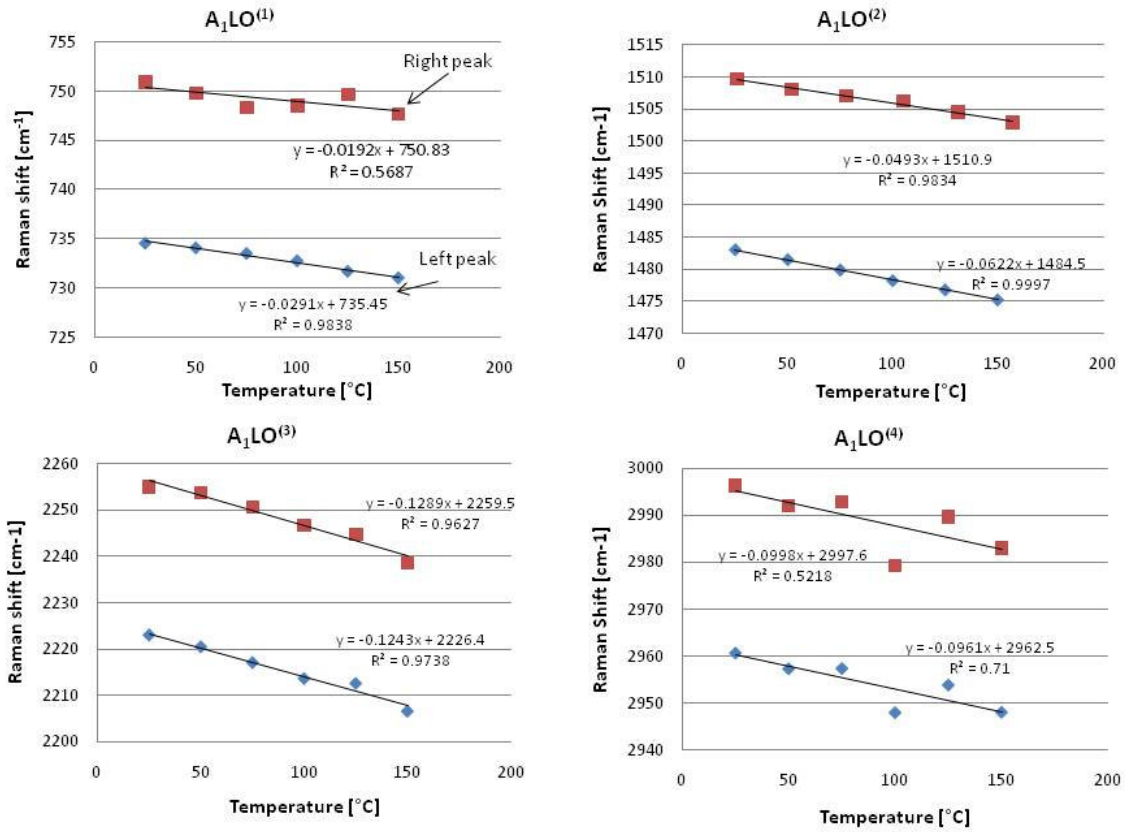

Figure 46. Raman shift vs. temperature for the left and right (deconvoluted) peaks for the first four $A_1(LO)$ phonon modes.

with increase in temperature, although the quality of correlation between temperature and peak shift, as well as the sensitivity varied across the different phonon modes. As Figure 43 shows, the intensity starts out minimal for the first order mode and increases to a maximum value for the fourth order mode, before decreasing for the fifth order mode. The correlation factor starts at 0.984 for the first order mode (left peak) and increases to a maximum of

0.999 for the second order mode, before decreasing again for subsequent modes.

The decrease in relative intensity and correlation factor could be linked to the presence of a broad photoluminescence peak at higher wavenumbers where the higher order phonon modes appear.

Figure 47 shows that the sensitivity tends to increase for each order peak of the A_1(LO) phonon until the third order, from which it starts to decrease again. Although lower order A_1(LO) peaks may display low sensitivity for temperature measurements due to their relatively low peak intensities, higher order A_1(LO) peaks are overshadowed by the broadband photoluminescence peak from 2000 to 4500 cm^{-1}, leading to a decrease in sensitivity from the maximum of 0.12 $cm^{-1}C^{-1}$.

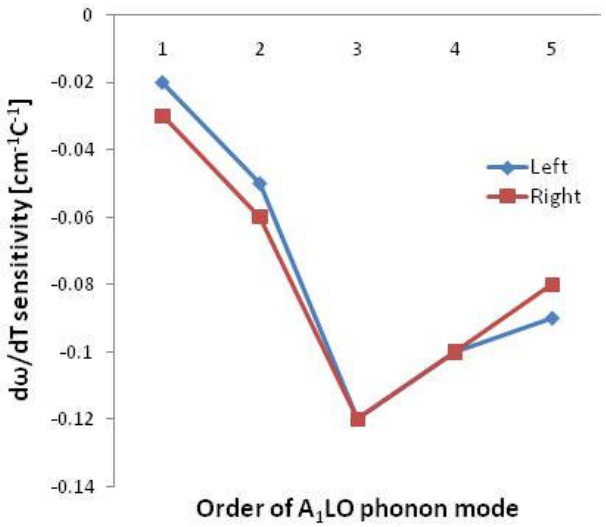

Figure 47. Thermal measurement sensitivity for various A_1(LO) resonant phonon modes.

By applying a bias across the source and drain of a HEMT device, increasing amounts of heat were generated. Figure 48a displays the relationship between measured substrate temperature and applied power density. The power density was calculated by multiplying the drain-source voltage with the drain-source current and dividing by the gate width. As expected, the measured device temperature increases as the applied power density increases.

Because the Raman measurement technique relies on the piezoelectric activity between atoms in the lattice, some skepticism has been voiced over the suitability of using the micro-Raman thermal measurement technique when the device is under operating conditions (i.e., an electric field is applied across the channel). To investigate the applicability of this measurement technique, two different current-voltage combinations (6.75 V x 259 mA and 25 V x 70 mA) amounting to the same power density (8.74 W/mm) were applied to the device. The base plate was held to a constant temperature of 50 °C to provide an isothermal boundary for comparison of the measured results to simulated results later on. The result is displayed in Figure 48b: the peak positions are approximately the same for the two isopower conditions, despite the stark difference in applied voltage, which would produce a large electric field across the lattice, which has piezoelectric properties.

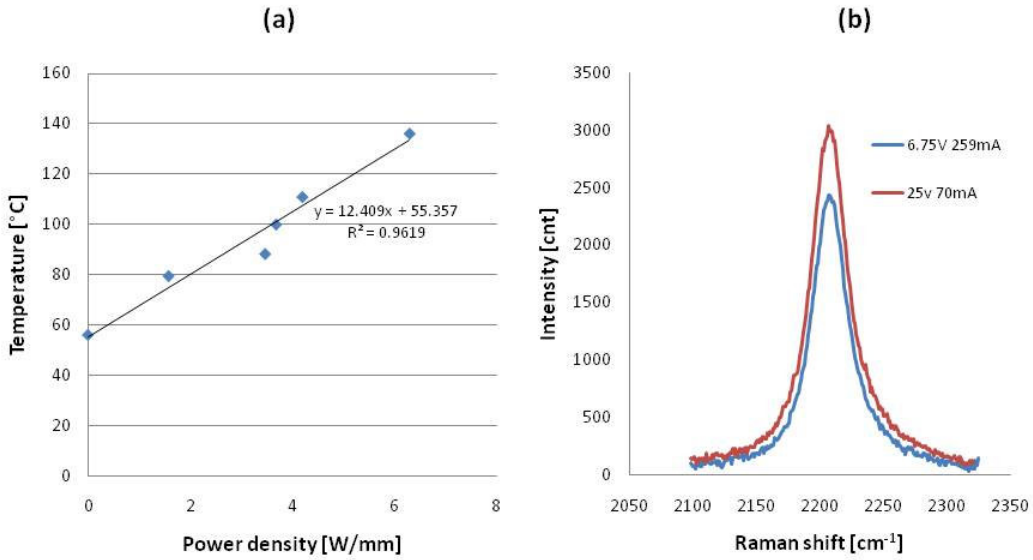

Figure 48. a) Temperature vs. power density calibration plot for a biased HEMT device, and b) Superposition of two $A_1(LO)^2$ Raman peaks with the same power densities but different current-voltage combinations.

The temperature profile resulting from a finite element analysis simulation of a similar HEMT layout using finite element analysis is shown in Figure 49a. At 11 W/mm, the temperature indicated by the profile near the left end of the channel (0.5 um from the left end as depicted in the inset) and at the extinction depth of the laser (50 nm) was 112 °C. This is consistent with the measured micro-Raman result of 113 ℃ at the sa me location using the $A_1(LO)^3$ phonon mode peak. Although the measurement result was very close to the simulated result, it is not the intention of this discussion to show that the Raman technique has an accuracy of +/- 1 ℃, but ra ther, that the simulated and empirical results are similar to some degree. This provides more evidence that the micro-Raman thermal characterization technique using a surface sensitive laser wavelength may be a viable, high throughput measurement technique to aid in HEMT device reliability efforts. It is important to address,

however, the limitations of this measurement technique. Because the active channel (dark grey in Figure 49a inset) consists of non-ion implanted semiconductor material, the microstructural material quality is actually higher than the non-active area surrounding the device. This higher material quality leads to a higher intensity photoluminescence signal, which decreases the relative intensity of the higher order Raman peaks that exist in the same range, making it difficult to resolve them and obtain temperature readings. For that reason, micro-Raman temperature measurements were taken just outside the ion implantation boundary (0.5 µm from the center of the laser spot to the

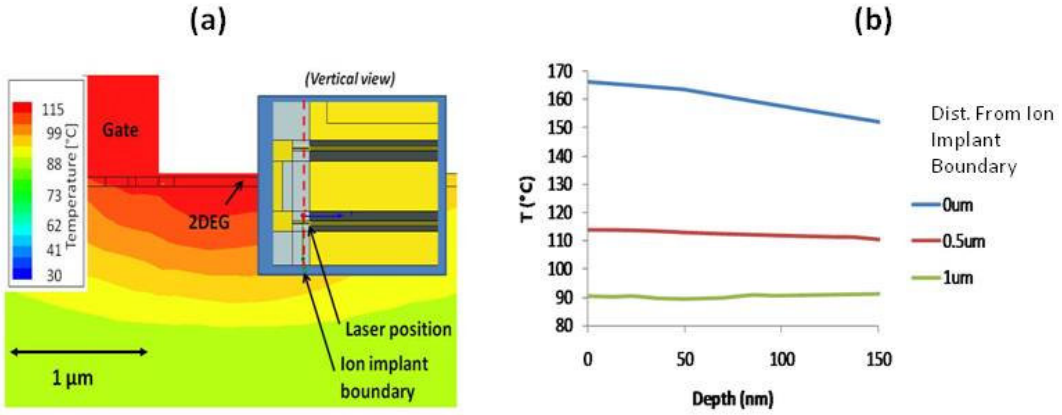

Figure 49. a) Simulated temperature distribution of the active channel region of a GaN HEMT. b) Temperature profile with depth at different distances from the ion implantation boundary (pictured in inset of (a)).

boundary). The measurement was highly sensitive to the distance that the center of the laser spot was from the active channel region. As can be seen in Figure 49b, the temperature dropped from 165 to 113 ℃ over a 0.5 µm distance. Fortunately, the micro-Raman test system used in this study had a translation tolerance of less than 0.1 µm.

Further tests were conducted to determine the reliability of using micro-Raman as a thermal mapping tool in HEMT devices. Figure 50a indicates the peak positions at different equally spaced locations along a 200 µm channel of the second order A_1(LO) phonon mode at two different baseplate temperatures while the device was left unbiased using a 10X objective for incident and Raman-scattered light to pass through. The standard deviation of the Raman peak positions along the width of the channel is 2.744 cm^{-1} at 150 ℃, while it is only 0.99 cm^{-1} when the device is at room temperature. The increased variation in measured temperature is more likely due to measurement error rather than actual physical variation in temperature. As the temperature rises, the Raman peaks broaden and decrease in intensity, reducing the accuracy of the measurement. The use of the higher magnification objective (40X), however, produced increased uniformity across the channel, with a standard deviation of 0.41 and 0.09 cm^{-1} for 150 ℃ and

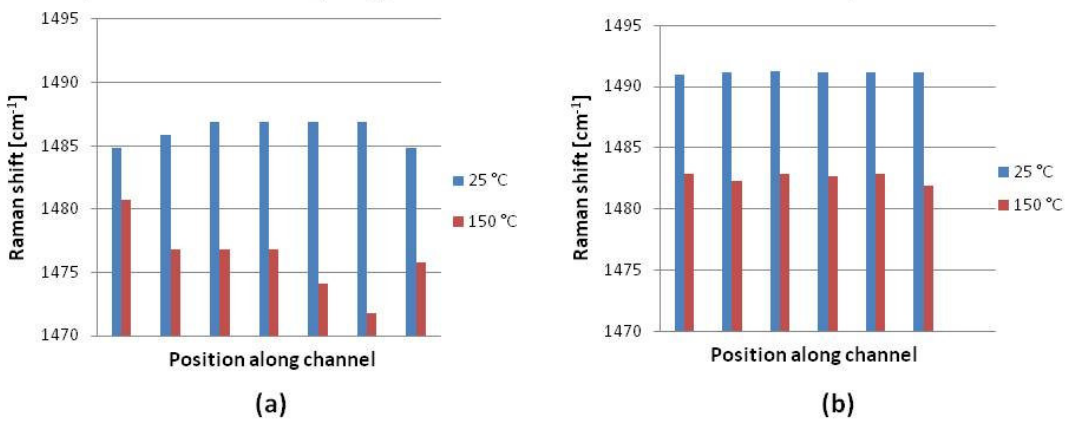

Figure 50. Raman shift vs. position along a channel between the gate and drain at low and high temperatures when a) using a 10x objective and b) a 40x objective.

25 ℃ baseplate temperature, respectively (Raman sh ift profile featured in Figure 50b). This translates to a thermal reading accuracy of +/- 6.5 ℃ at 150 ℃ and +/- 1.5 ℃ at room temperature.

Since the broad photoluminescence peak interfered with in-channel Raman measurements (particular for the more sensitive, higher order modes), the possibility of photoluminescence as a temperature measurement tool rather than Raman was investigated. Photoluminescence (PL) occurs when above band gap photons cause carriers to become excited to a higher energy state and then drop to a lower energy state by releasing a photon. One such common excitation in GaN is when an electron becomes excited from the valence band to some higher level in the conduction band and eventually drops from the conduction band to the valence band, producing photons characteristic of the band gap energy of GaN.

Since the band gap changes with temperature it was conceivable to use PL as a temperature measurement tool. However, because the luminescence may be affected by current flow through the HEMT junction (causing conduction band filling of carriers and thus a possible PL peak shift not due to temperature), in the past the tool has been believed to be an unreliable tool for temperature measurements. Despite this, an effort was made to separate out the PL peak shift due to the change in current so that a current independent temperature measurement could be made. Using the same 325 nm laser setup, the detector was adjusted to track only the extent of the PL peak. Figure 51 indicates the PL peak position change with increase in current (left) and with increase in base plate temperature (right). As expected, the PL peak position shifts to lower wavelengths with an increase in current flowing through

the channel because of conduction band filling of electrons, translating to a higher energy drop of the carriers from the conduction band during PL effects, and a likewise higher energy photon emission. Moreover, the PL peak shifts to longer wavelengths with increase in substrate temperature, reflecting the decrease in the band gap of GaN with temperature.

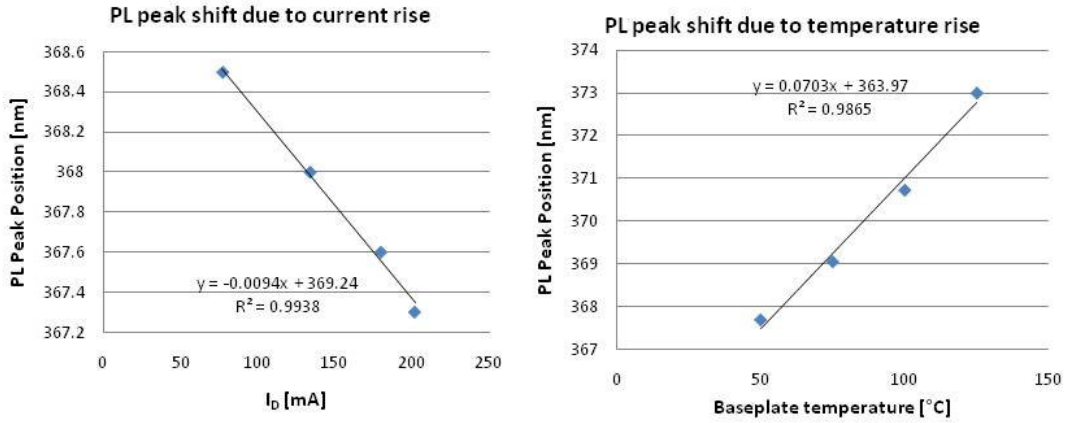

Figure 51. PL peak shift due to current rise at constant temperature (left) and due to temperature rise at constant current with 325 nm wavelength excitation.

Although the PL peak shift depends on both current and temperature, the latter has a 7 times greater peak shift sensitivity than the former (0.07 $nm \cdot ℃^{-1}$ vs 0.0094 $nm \cdot mA^{-1}$). Despite this accuracy, to determine a more accurate relationship between PL peak shift and temperature, a more extensive parameter space calibration could be carried out, in which the peak position as a function of both temperature and current, should be conducted. A further point to consider is that PL also measures an average temperature due to the surrounding luminescence instead of a highly localized spot, as is the case for micro-Raman measurements. If highly localized, high resolution thermal mapping is required, micro-Raman measurements may be more suitable. However, for coarser, high throughput measurements in which

measurement time is an issue, PL could prove to be a promising measurement tool.

Conclusion

The micro-Raman technique with a 325 nm wavelength, surface sensitive laser has proven to be a suitable tool for measuring local temperatures in an AlGaN/GaN HEMT device. The full spectrum of Raman and PL peaks for GaN were calibrated to changes in temperature and errors were characterized. A maximum sensitivity of 0.12 $cm^{-1} \cdot ℃^{-1}$ was recorded for measuring temperature with the $A_1(LO)^3$ resonant phonon mode peak. Lower order Raman peaks have a lower intensity and lower sensitivity to temperature change, whereas higher order peaks are overshadowed by the broad PL background. To verify that this peak is solely sensitive to temperature, the measurement was repeated under one power but at different current-voltage combinations and the peak remained in the same position. At a constant power, the Raman measurement indicated a temperature that matched that of a finite element simulation. The accuracy of the micro-Raman measurement technique was verified by taking measurements at various locations along a HEMT channel at various temperatures and indicated a measurement error of +/- of 6.5 ℃ and 1.5 ℃ at high temperatures and l ow temperatures, respectively.

Although the exact origin of the heating is unknown, it is believed to originate from phonon generation in the lattice surrounding the 2DEG, in which the high current density is likely to cause some electron scattering with the lattice despite confinement of the electrons to a sheet. The graphical results of the finite element method simulation seem to agree with the idea that the heat

is generated from the 2DEG, however, other measurement studies should be conducted to see if the heat generation originates from another source (such as the contacts), which would lead to a better understanding for HEMT reliability improvements.

III. GALLIUM NITRIDE TERAHERTZ EMITTERS

Background

Terahertz radiation, which consists of frequencies spanning from the upper edge of the microwave spectrum (300 GHz) to the beginning of the far infrared spectrum (3 THz), has the property of being able to penetrate several types of non-conductive matter, from ceramics and fabrics to water and clouds. For this reason, terahertz wave emitters have attracted increased interest due to their unique abilities in security, imaging, and communications applications [45,46]. Current sources include backward wave oscillators (based on vacuum tube technology), FIR lasers, and photomixers. Despite the variety of emission sources, no current terahertz generation technology produces high power emission, and efficiencies have been limited to sub-1% performance.

Gallium Nitride based terahertz emitters may be able to offer higher efficiency and higher power generation at room temperature and higher (ThZ black body radiation occurs in the 10 K range) because of the unique electrical properties of GaN. The material may be uniquely suitable because of its high breakdown field, wide bandgap, and unique band structure, which facilitates device operation at higher frequency and power compared to other compound semiconductors such as GaAs [47,48].

GaN terahertz emission is expected to result from acceleration and deceleration of carriers in the conduction band. The negative effective mass experienced by electrons due to the inflection point in the conduction band at high fields is expected to lead to the deceleration of ballistic electrons via

transfer of electrons to the upper valley of the conduction band and via phonon launching. Inflection point negative differential resistance (INDR) was proposed by Kromer [49] and further developed by Esaki and Tsu [50] and others [51]. Wraback *et al.* have found evidence through pulsed light experiments that the INDR effect is possible in GaN [52]. This study will focus on determining what material and process improvements are required for successful development of a GaN terahertz device.

The momentum relaxation of electrons which produce terahertz radiation can also be viewed from the perspective of the velocity-field curve of electrons in GaN. In würtzite GaN, as depicted in Figure 52, the electron drift velocity reaches a maximum of 2.5 x 10^7 cm/s before 200 kV/cm (Note that the data from the figure is recorded for uniform fields in thick channels, however analogous behavior can be expected in thin channel GaN terahertz devices).

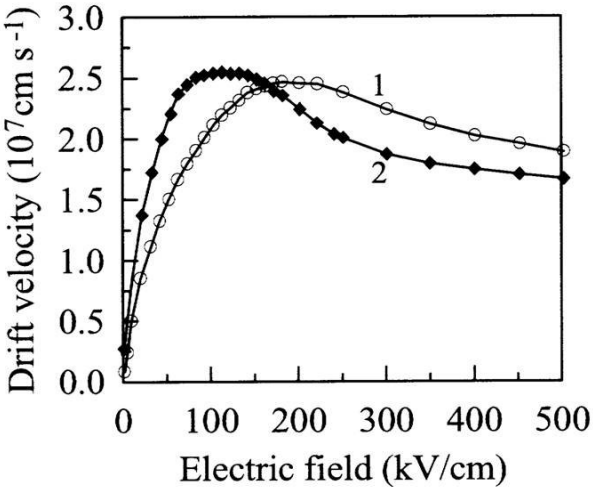

Figure 52. Velocity-field curve of GaN in the 1) würtzite [53] and 2) zinc-blende crystal structure [54].

This means that electrons will initially accelerate ballisticly in a channel (meaning they are not scattered by phonons) before reaching a maximum velocity and slowing down. Subsequent electrons will accelerate but be slowed down by the electrons ahead of them in the channel, which have already reached the maximum velocity.

The associated build up in density of electrons, referred to as an accumulation layer (as depicted in Figure 53), travels as a single layer of electrons through the short channel until finally reaching the contact at the other end of the channel, decreasing its energy to a ground state and releasing photons characteristic of terahertz frequency in the process.

Figure 53 displays the basic operation of a GaN-based INDR device. First, a voltage source applies an electric field across a low doped GaN channel that is connected to highly-doped GaN on both sides. The highly doped GaN aids in high quality ohmic contact formation so that series resistance at the contacts is sufficiently low to allow for high efficiency operation and minimal heat generation. Electrons entering at the top contact are launched ballisticly into the channel because of the high electric field, but begin to decelerate after some distance due to the INDR effect described above. The formation of the electron accumulation layer travels through to the other end of the channel and releases terahertz radiation due to the drop in energy to ground state. The resulting terahertz radiation is pulsed in nature because only one accumulation layer travels across the channel at a time.

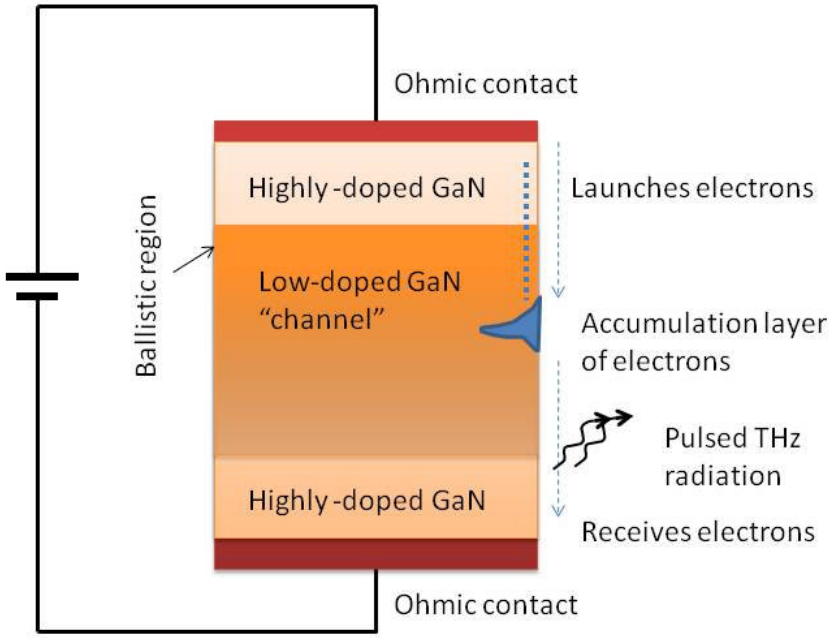

Figure 53. Basic operation of a vertical, thin-channel GaN terahertz emitter device.

MBE grown GaN material is potentially more advantageous than other technologies due to the ability to grow abrupt junctions and doping profiles. As will be expanded upon in a subsequent section, conditions for INDR strictly dictate what type of doping levels and thicknesses are required for terahertz oscillations to be produced. Furthermore, MBE grown samples typically have much less impurities due to the high vacuum environment, have higher doping levels are typically achievable for forming very low resistance ohmic contacts, and the ability to monitor crystal growth quality *in situ* allows for production of smooth layers necessary for very sensitive device processing with small feature lengths.

Despite the aforementioned advantages of using MBE-grown GaN for terahertz emitting devices, problems that have at this point in time prevented

the successful development of GaN terahertz emitters abound. Both excessive self heating due to current travel in the GaN lattice and resistive overheating from contacts have impeded successful terahertz device operation. Certain changes to the device geometry such as changing from vertical to planar structures (Figure 53 depicts a vertical structure, whereas Figure 54 displays a horizontal one) have been made to improve thermal dissipation [55]. Further problems include GaN material quality, which includes both surface morphology and electrical properties. Regarding the former, very smooth surfaces are required to process small feature length patterns necessary for terahertz devices. The challenges related to electrical properties mostly encompass being able to achieve high electron densities through degenerative doping in order to form low resistance contacts, as mentioned earlier. This study will investigate both the material- and device-related challenges for producing GaN THz emitters.

Layer structure and device physics

Figure 54 illustrates a device cross section for an MBE-grown, GaN THz structure utilized in this study. GaN material was grown on a 200 nm AlN buffer atop a sapphire substrate. A one micron unintentionally doped GaN buffer was was grown to reduce defect density and lattice strain. The active channel layer had a thickness of 40 nm and electron concentration of 1×10^{18} cm^{-3} (denoted as “n-“), and the degeneratively doped GaN layer had a thickness of 50 nm and an electron concentration of 3×10^{20} cm^{-3} (denoted as

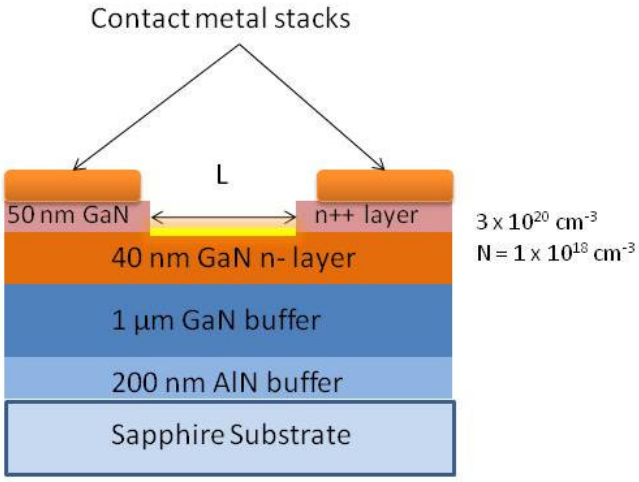

Figure 54. A cross section of a horizontal GaN terahertz device detailing the layer architecture and doping levels.

the “n++” layer). Several contact metal combinations with low work function were deposited on top of the n++ layer across different samples to explore low resistance contact regimes. The growth and process details are provided elsewhere [56]. The channel length, *L*, depends on what is known as the *nL* product, which determines whether transient effects leading to terahertz oscillation will occur or not, where *n* is the doping density. Typical *nL* products for mm wave emitters based on the INDR phenomenon lie between 1 x 10^{16} m^{-2} and 3 x 10^{16} m^{-2} [57]. Designing the device size and doping density in the layers then becomes an optimization problem, as a higher doping density in the channel will allow electron accumulation layers to nucleate and grow easier, however, too high of a density will cause current to become so high that the device could overheat and quickly burn out. Secondly the length of the high-field region must be great enough for electrons to reach beyond the inflection energy. Otherwise, electrons will not achieve negative effective mass and thus negative differential mobility, which facilitates the INDR effect. After

considering this device criterion, 0.25 μm became the designed length, *L*, in this study.

With these design and material growth criteria, attempts were made to produce GaN-based terahertz emitters based on the INDR effect. The following study will focus on terahertz device development through two principal areas: material improvements, consisting of such topics as doping and film growth, as well as device processing improvements, consisting of such topics as ohmic contact metal schemes and etching.

Materials studies

A deep understanding of the physical and electrical properties of GaN is important for successful fabrication of GaN devices. The high voltage operation of GaN Thz devices requires efficient performance to prevent overheating, which depends heavily on doping density and the ability to develop small feature-length devices on the film with tight tolerances, which requires smooth, homogeneous film morphology.

Effect of nitride-alloy stoichiometry on processing

The stoichiometry of GaN films during MBE growth is watched carefully during the growth process, for it can have effects on both the surface morphology and electrical properties of the material. To explore this effect further, three identical terahertz layer structures (as in Figure 54) were grown with different stoichiometries (highly gallium-rich, highly nitrogen-rich, and less nitrogen rich GaN). The stoichiometry was varied by altering the substrate temperature during film deposition. Lower temperatures increased the rate of gallium condensation on the surface, whereas higher temperatures prevented

gallium from sticking to the surface. The surface morphologies of the different conditions as viewed through a confocal microscope are presented in Figure 55. Notice that the metal rich (a.k.a. “gallium-rich”) sample contains black, circular features tens of microns in size. These circles are indicative of metal precipitates that condense on the surface of the film during growth due to supersaturation of gallium atoms. The nitrogen-rich sample seems to be void of the black circles, although fine features still remain on the surface, indicative of film roughness due to excessive etching due to ionized nitrogen atoms impacting the surface during growth. The “less N-rich” sample was still grown on the nitrogen-rich end of the stoichiometric range, but less so. The micrograph for this sample seemed to show a lack of fine features present in the extremely nitrogen-rich sample, indicating that less etching occurred on the surface, resulting in a much smoother morphology.

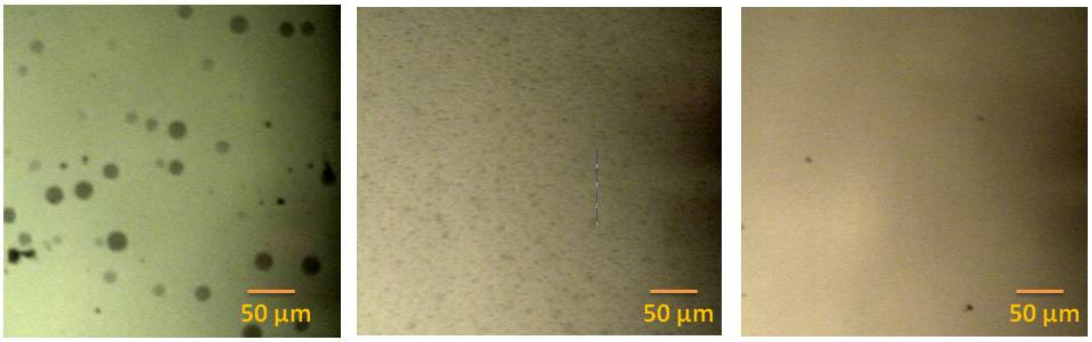

Figure 55. Confocal micrographs of GaN films grown by MBE under different GaN stoichiometries.

The stoichiometry and quality of the GaN film is monitored via RHEED. Figure 56a displays a RHEED picture taken during the metal-rich film growth. The smooth, long streaks of the former represent smooth, high quality film

growth and the medium brightness reflects an abundant presence of metal on the surface. In contrast, Figure 56b displays a RHEED picture from the nitrogen-rich growth. The disconnected, bright spots reflect the presence of several facets on the surface caused by nitrogen etching of the film. Furthermore, the intense brightness of the spots is indicative of excessive nitrogen and lack of gallium at the surface.

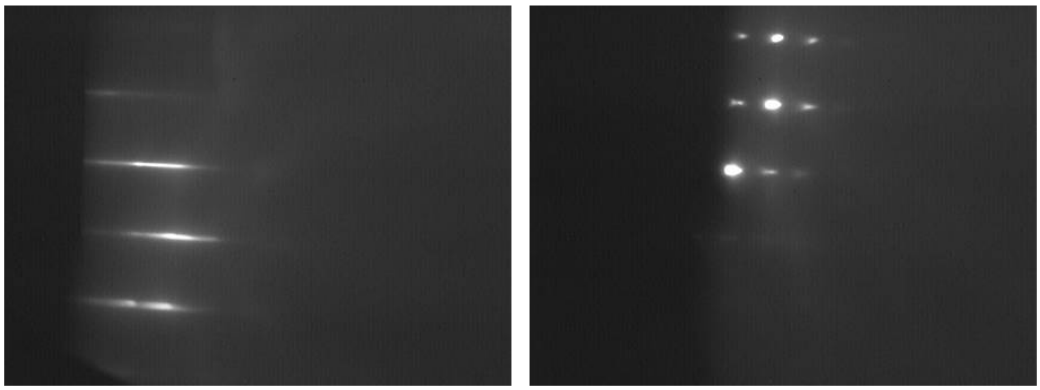

Figure 56. RHEED patterns during GaN MBE film growth under a) metal-rich and b) nitrogen-rich conditions.

A surprising finding is that the RHEED pattern appearing in the metal-rich condition is often reflective of a balanced stoichiometry. This could be misleading, since the RHEED pattern does not reveal the presence of the undesirable metal precipitates on the surface.

A more in-depth study of the surface morphology ensued, in an effort to better understand how the stoichiometry affected the surface. Figure 57 features atomic force microscopy (AFM) images of wafers with films of different stoichiometries (highly gallium-rich, highly nitrogen-rich, and less

nitrogen rich GaN). As expected by the smooth RHEED pattern, the metal-rich sample featured the lowest measured surface RMS roughness, at 7.5 nm, while the nitrogen-rich sample had a roughness of 19.8 nm. By making the stoichiometry slightly less-nitrogen rich, but nevertheless still on the nitrogen-rich end of the spectrum, the roughness decreases to 13.7 nm. Although this is still larger than that of the metal rich condition, it is still manageable, and more importantly the film is void of metal precipitations that make device patterning nearly impossible.

A closer observation of the AFM images in Figure 57 reveals further information. In the metal-rich film, several smooth, large grain boundaries exist. In the extremely nitrogen-rich film, the grain boundaries shrink and

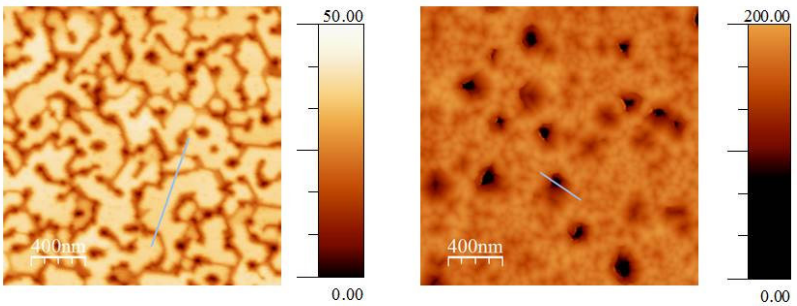

GaN film type	RMS [nm]
Metal-rich	7.5
N-rich	19.8
Less N-rich	13.7

Figure 57. AFM images of GaN films grown with different stoichiometries (clockwise from top left): metal-rich, extremely nitrogen-rich, and less nitrogen rich. The table indicates the corresponding RMS roughness values.

exhibit larger variation in height. In addition, the black spots indicate the presence of several deep pits that further contribute to roughness and make device processing difficult. Lastly, the less nitrogen-rich sample shows a decrease in height variation across the grains and is void of several large pits that were present in the extremely nitrogen-rich film.The results indicate that an improved surface quality can be obtained by deviating from “ideal” growth conditions. Despite the increased surface roughness resulting from slightly nitrogen-rich growth, the films do not contain metal precipitates or etched pits, both of which are detrimental to small feature-length device processing.

Doping

Because high efficiency devices with minimal heat generation are required for high performance terahertz emitters, minimal series resistance leading to heat generation at the ohmic contacts is desired. To facilitate lower contact resistance, degenerate doping at the surface is desired to lower the interfacial barrier to carriers traveling from the metal to the GaN channel [58]. In an attempt to characterize the doping range of donors in MBE grown GaN, several GaN films were grown while doped with Germanium donors and characterized by Hall Effect measurements. Although silicon is typically the donor dopant of choice in GaN film growth, germanium was used instead due to its larger atomic radius, which produces less stress on the GaN lattice.

Figure 58 depicts the electron density and mobility for each of the growths performed. The Ge cell temperature was varied from 880 to 1377 ℃, which results in a corresponding electron density range of $1.2x10^{18}$ to $8.8x10^{20}$ cm^{-3}. Mobility stably decreased from 115 to 39 $cm^2V^{-1}s^{-1}$ over the same Ge

doping temperature range. The 2002 data reflects conditions of an older MBE growth machine. The electron density for these samples seems to saturate with increased Ge incorporation. Observing the 2009 data, however, shows that the electron density continues to increase with increases in Ge cell temperature, with values well above the old results. The decrease in mobility with increase in doping is due to ionized donor scattering of electrons.

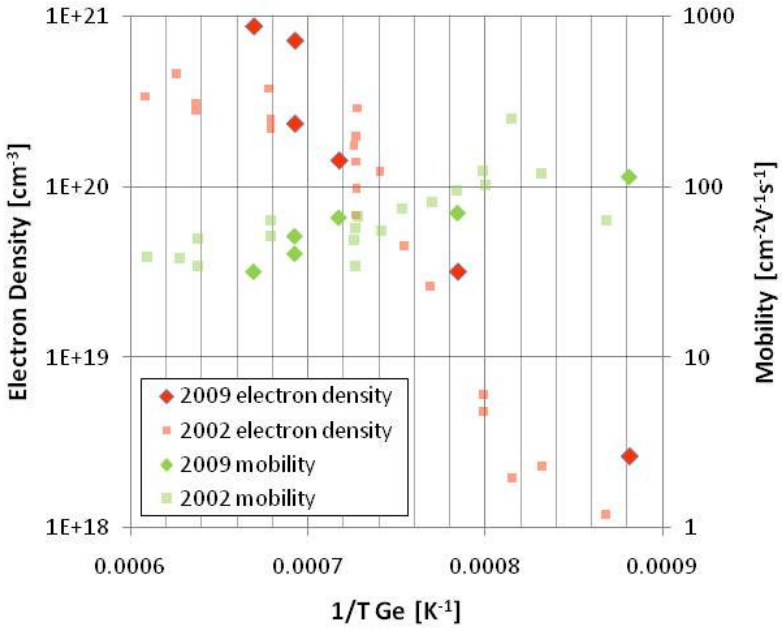

Figure 58. Measured electron densities and mobility values of GaN films doped at different germanium temperatures collected by Matthews *et al.* (diamond symbols) and by Hagemon *et al.* (square symbols) using the same MBE machine [59].

The doping study concluded that extremely high electron densities were achievable by growing GaN films by MBE with a Ge doping source. Germanium appeared to be a more desirable source for high doping levels,

because its similar atomic radius to Ga allowed for modest compression to occur, leading to a smoother surface morphology. In contrast, silicon atoms result in tensile strain that lead to surface rougness at high doping levels. The samples in this study were subsequently subject to contact metal evaporation to determine what metal combinations would yield minimal contact resistance, as the following study will detail.

Device studies

Fabrication of GaN terahertz emitters based on the INDR effect have been attempted in the past, although successful terahertz radiation from these devices has not yet been detected [60]. The results of these attempts, however, revealed what types of obstacles have stood in the way of successful device fabrication: namely, low resistance ohmic contact formation and achieving tight tolerance of etch depth during the lithography process.

Ohmic contacts

Low work functions of metals contacting n-type GaN are typically responsible for forming low resistance contacts. Changes in the work function of the metal may come from alloying of different metals within the stack and the GaN work function decreases with increasing electron density [58]; hence a high donor doping density at the interface without distorting or saturating the lattice is desired. Ti, Sc, V, and Nb represent low work function metals suitable for forming ohmic contacts to n-type GaN. These metals tend to form intermediate phases at the metal-semiconductor interface such as TiN, and ScN [61]. The formation of these phases involves the removal of nitrogen from

the GaN lattice, forming donor like states near the interface, which may aid in ohmic contact formation.

Further issues for ohmic contacts to GaN terahertz emitters include lifetime stability and high temperature reliability. Considering the large amount of heat dissipation for GaN terahertz devices, it is imperative to protect against contact degradation by employing metals in the contact stack that serve as diffusion barriers to low melting point metals such as Au and Al and can resist oxidation [62]. Mohammad *et al.* have documented detailed design principles for ohmic contact stacks [63] while Sun *et al.* have determined optimal thickness combinations of contact metals [64]. Others have reported performance of ohmic contacts to n-GaN as a function of anneal temperature and time [65,66]. The contacts appear to remain stable with time at low anneal temperatures (<500-600 ℃) but then degrade sharply in time or with temperature.

Table 2 lists the various metal combinations deposited onto degeneratively doped n-type GaN films. The metals were selected primarily due to their low work functions, since that would presumably lower the barrier energy for electrons to travel from the metal contacts to the n-type GaN. This study featured metal stacks with similar base metals but different combinations above in order to observe if a direct correlation between the base metal work function and contact resistance existed or if the contact resistance depended on the chemical interaction between the different metals in each combination.

Table 2. Metal stacks deposited on n++ GaN along with their layer thicknesses and work functions of the base layer in each stack.

Metal stack	Layer thicknesses (Å)	Work function of first metal (eV) [16]
Sc	1100	3.3
Sc/Au	500/600	3.3
Ti/Sc/Mo/Au	100/600/400/450	4.33
V/Al/V/Au	150/800/200/1000	4.12
Nb/Al/Nb/Au	150/800/200/890	3.97
Nb/Au	150/300	3.97
Ti/Al/Mo/Au	150/900/400/500	4.33

Figure 59 presents the specific contact resistances obtained from the TLM patterns vs. anneal temperature for an n++ concentration of $2x10^{20}$ cm^{-3} for six different ohmic metal stacks. Among the best performing ohmic contacts were the V/Al/V/Au and Nb/Al/Nb/Au stacks, whose resistance amounted to 1.59 and 1.76 x 10^{-7} $\Omega \cdot cm^2$, respectively, at 700 ℃. Among the

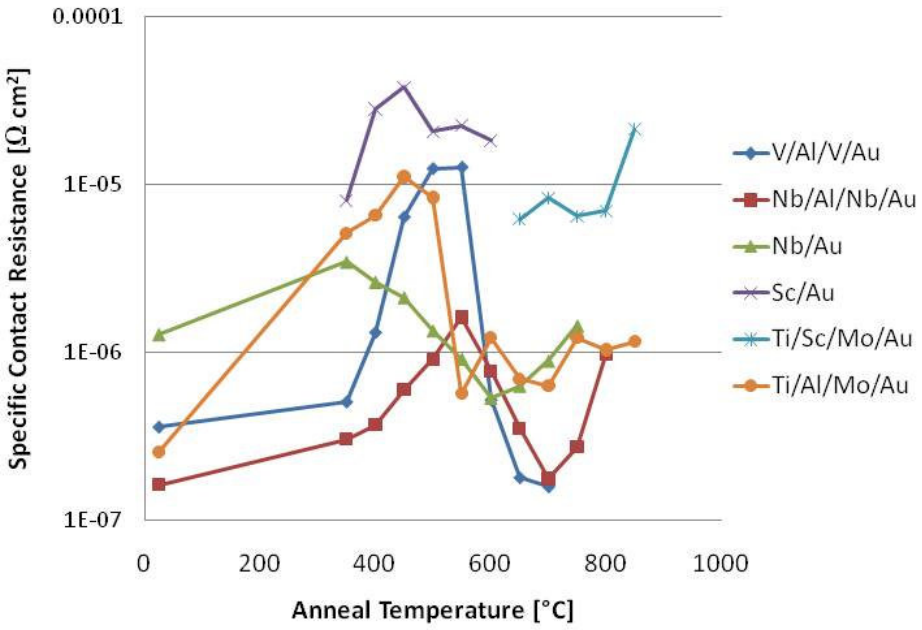

Figure 59. Ohmic contact performance as a function of anneal temperature for various metal stack combinations.

worst performers were Sc/Au and Ti/Sc/Mo/Au, each with best resistance values of 7.98 and 6.2 x10^{-6} Ω·cm^2 at 350 and 650 ℃, respectively. Absolutely no correlation between the work functions of the metals contacting the GaN surface and the contact resistance became evident. In fact, Sc, with a work function of 3.3 eV, actually displayed the highest resistance, while Nb, and V, among the highest of the group, displayed the lowest resistance, contrary to expectations.

Furthermore, metal stacks with the same metal in contact with GaN featured differences in contact resistance by more than an order in magnitude, indicating that interdiffusion between metals was responsible for differences in contact resistance. The anneal profiles tend to show a maximum between 450 and 550 ℃. The increase in resistance in this rang e, as well as a reduction in

fit quality of the resistance vs. TLM pad separation curves hint at a degradation in ohmic contact quality. The sheet resistivity remained largely unchanged at 40 Ω/□with increase in anneal temperature for all metals.

In addition to the evidence presented above that suggested some type of chemical interaction between different metal layers in the metal stacks occurred, a suspicision arose that an oxide layer may have also formed between certain base layer metals and GaN at the contact interface, thus affecting the contact resistance. For this reason, an experiment was conducted in which highly and lightly doped n-type GaN films had the Ti/Al/Mo/Au metal stack deposited upon them. Normally samples are immersed in buffered oxide etch (30:1) for 30 seconds following pattern exposure and development during photolithography, before being placed immediately under vacuum for contact metal deposition. In this study, however, the patterned GaN films were deliberately left in an air ambient environment for prolonged, but measured amounts of time before placed under vacuum to see if oxide layers formed and affected contact resistance.

Figure 60 presents the contact resistance results for both a highly doped n-type sample ($2.4x10^{20}$ cm^{-3}) and a lightly doped sample ($3.2x10^{19}$ cm^{-3}) deposited with the Ti/Al/Mo/Au metal stack for varying amounts of time exposed in an air between the oxide etch step and pump-down to vacuum in the evaporator chamber. It can be seen in both cases that contact resistance eventually increases with time. In a nearly 24 hour period of exposure to oxygen after the oxide etch, the highly doped GaN sample experienced an increase in contact resistance from $6.92x10^{-7}$ to $1.84x10^{-5}$ $\Omega \cdot cm^2$, while the

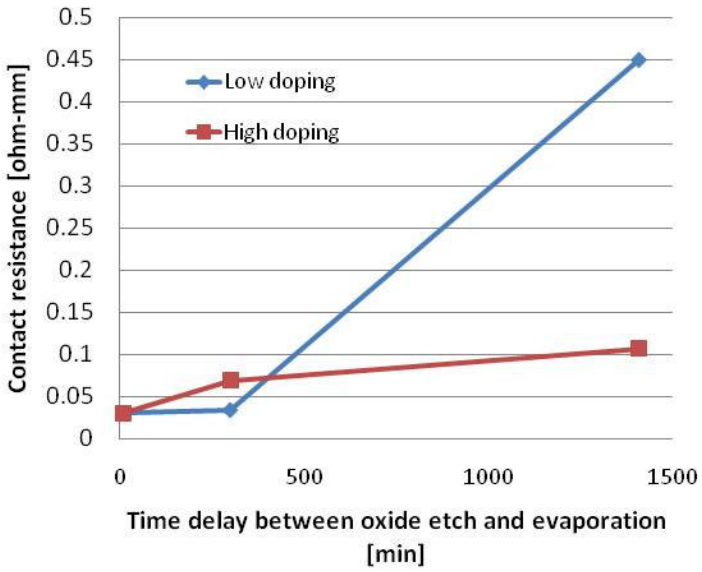

Figure 60. Relationship between contact transfer resistance of Ti/Al/Mo/Au metal stack and time elapsed between oxide etch and of wafer and placement in vacuum chamber for evaporation of metals.

resistance of the lightly doped GaN sample started at 2.46×10^{-6} $\Omega \cdot cm^2$ and increased to a much higher value of 1.8×10^{-5} $\Omega \cdot cm^2$. These relationships show that an oxide formation may indeed be taking place at the metal-GaN interface, between the time of the oxide etch and the evaporation. Although the lightly doped sample exhibited a higher resistance than that of the highly doped sample in the case for which the wafer was almost instantly placed under vacuum after the oxide etch, the highly doped sample seemed to degrade much faster than the lightly doped one.

Etching

To isolate current flow to the GaN n- channel, the n++ layer between the two contacts must be etched (see the recessed area between the contacts in Figure 54). Because catastrophic failure due to overheating is a major concern in GaN terahertz device fabrication, it is of major interest to precisely control etch depth through the n++ layer. Careful care must be executed to etch just a few nanometers into the n- layer, but no more. Because conventional methods of measuring depth such as profilometry did not provide the level of accuracy required for this tight tolerance, an electrical method for characterizing etch depths was developed.

A lithography process was developed to form mesa isolated TLM contact pad patterns (similar to those in the Appendix 2) with recessed rectangles between the rectangular contact pads. The recessed features were formed by ion mill etching with the intent of changing the resistance by decreasing the cross-sectional channel area. The relationship between conductance and etch time was then used to calibrate the process to reach the desired etch depth.

Figure 61a indicates the sheet conductance (measured by TLM) of an MBE grown GaN terahertz layer structure with a 4×10^{20} cm^{-3} electron density n++ GaN layer atop a 1×10^{18} cm^{-3} n- GaN layer etched with a Veeco Ion Mill for varying amounts of time (and thus varying depths). As the etching continued, the sheet conductance decreased from an initial value of 0.01 mhos to 2×10^{-5} mhos, since the decreased cross sectional area available from the decreasing thickness caused by etching led to increased resistance, or decreased

conductance. This agrees somewhat with the linearly decreasing profile that was calculated theoretically and is displayed in Figure 61b.

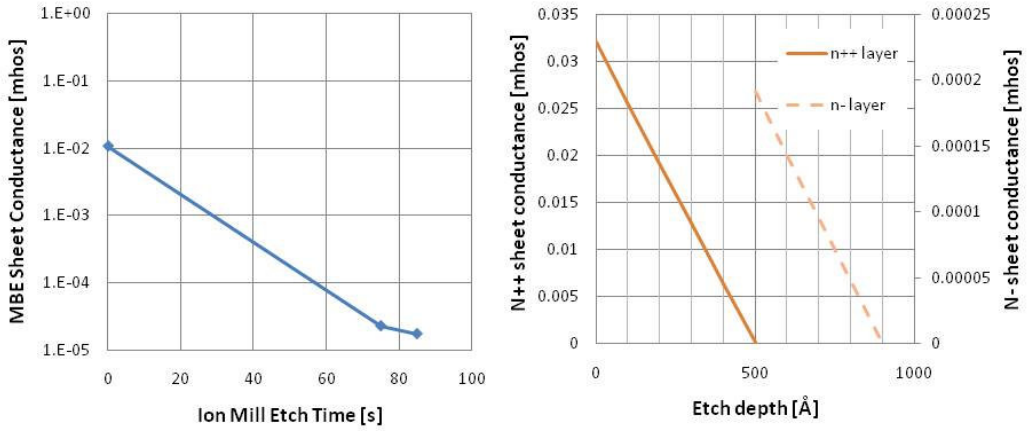

Figure 61. a) Measured sheet conductance through n-type GaN films as a function of etch depth and b) theoretical sheet conduction vs. etch depth profile through the n++ and n- layers in a corresponding terahertz structure (note that the n- sheet conduction is on a different scale).

The theoretical result shows a decrease to the 10^{-5} mhos range as the n++ layer becomes etched, and then a more gradual decrease in conductance for the remaining 40 nm of the film. The fact that the sheet conductance as measured through experiment began to decrease more gradually in the 10^{-5} mhos range following 75 seconds of etching, seems to indicate that the target depth has been reached and the etch process has been calibrated. Furthermore, previous device fabrication attempts involved ion mill etch times of well over 100 seconds, which would have etched away much of the n-channel, causing too much current to flow through too small of a channel cross section, which would explain the catastrophic failure experienced by devices due to overheating, before terahertz emission could be detected.

Summary

The study featuring GaN terahertz structures included both materials- and process-level improvements. Materials studies included exploration of the achievable n-type doping levels in GaN, as well as optimal GaN stoichiometries for high quality surface morphology. It was found that the maximum incorporation level of Ge yielded an electron density of $8.8x10^{20}$ cm^{-3} and mobility of 32 $cm^2V^{-1}s^{-1}$. Ge, due to its similar atomic radius to Ga, proved to be a suitable donor dopant, as higher electron densities than that of many MOCVD systems (in which silicon is typically used as a donor source instead) has been achieved. The study also unexpectedly revealed that slightly nitrogen-rich GaN stoichiometries during film growth is desirable because the surface contains no metal precipitates and few pits, both of which are disastrous to small feature-length devices such as terahertz emitters.

The process-level exploration encompassed both ohmic contact metal selection and etch process control. The lowest non annealed contact resistivity achieved on $2x10^{20}$ cm^{-3}, 50 nm n++ GaN material was 1.59×10^{-7} $\Omega \cdot cm^2$on V/Al/V/Au. As expected, the increasing carrier concentrations resulted in lower contact resistance values due to the lowering of the GaN work function with increased doping. It was found that chemical interactions occurred between the metals, GaN, and oxygen, resulting in oxide layer formation at the GaN-metal interface, and metal alloy formations occurring within the metal stacks upon annealing. Lastly, the etch process was calibrated by fabricating TLM patterns with recessed regions to measure changes in sheet conductivity with depth, and thus achieve precise control of etching through the n++ layer so that excessive heat generation would not occur during device operation.

Although a successful GaN terahertz emitter has not yet been created at the time of writing, several improvements to both the material and the process problems that have inhibited successful device formation have been made, and it is anticipated that a working device can be achieved soon.

CONCLUSION

The studies detailed in this thesis feature the exploration of the capabilities and limitations of devices based on MBE grown III-nitride materials under three principal applications: photovoltaics, high electron mobility transistors, and terahertz emitters. The experiments focused on addressing problems in each of these areas through both material- and device-level improvements.

III-nitride based photovoltaic cells have, despite their benefits, proved to be a challenging technology. Through material growth and characterization as well as device fabrication and testing, major obstacles preventing exceptional performance (notably leakage phenomena) were well characterized and modeled for future development. The empirical as well as the theoretical results indicated that better material quality (rather than device innovations) is required to achieve the spectacular theoretical potential of PV cells made using the III-nitride material system.

The design optimization of AlGaN/GaN HEMTs for higher power and efficiency operation resulted in successful improvements, namely increased sheet density (for higher current performance) and negligible gate leakage. Moreover, a novel characterization technique of using a resonant mode, surface-sensitive Raman laser technique to map HEMT temperature distributions during device operation was developed. The measurement technique has been fully characterized for measurement during HEMT operation. It is hoped that the method will be further developed and employed widely for analyzing HEMT reliability.

Terahertz devices based on GaN films have proven immense potential due to the ability for devices to operate at high power and high efficiency, but working devices have not yet been developed. The main identified process- and material-level problems that have inhibited successful GaN THz device operation have been addressed, so it is now anticipated that a clear path to achieving INDR-based terahertz emission in GaN devices may exist.

APPENDIX

1. III-Nitride material properties

Table 3 lists measured electronic properties of the three primary III-nitride binary materials: GaN, AlN and InN. E_g represents the band gap, E_{br} represents the breakdown field, m_e represents the electron effective mass, and P_{SP} is the spontaneous polarization.

Table 3. Electronic properties of würtzite GaN, AlN and InN.

	GaN (Wz)	**AlN (Wz)**	**InN (Wz)**
Eg [eV] [67]	3.43	6.2	0.77
E_{br} [MV/cm] [68,69,70]	3.3	8.4	1.2
m_e [71,72,73]	0.2	0.48	0.11
P_{SP} [C/m^2] [74]	-0.029	-0.081	-0.032

Table 4 lists the energy levels above the valence band (for acceptors) and below the conduction band (for donors) for various defects and atomic dopants in würtzite GaN as reported by experimental results. The dopants without labels are reported to be electronic traps such as nitrogen vacancies (E_c-0.44 eV) and often result in Fermi level pinning at about mid-gap in GaN.

Table 4. Energy levels of selected acceptors and donors in GaN.

Dopant (type)	Energy level in GaN (Wz) [eV]
- (n) [75]	E_c-0.44
- (n) [76]	E_c-0.5
Si (n) [77]	E_c-0.005
Mg (p) [78]	E_v+0.22
C (p) [78]	E_v+0.23
Be (p) [78]	E_v+0.25

Table 5 lists thermal parameters for common III-nitride binary compounds (GaN, AlN, and InN) as well as selected substrates for III-nitride epitaxy for comparison. κ_{300} represents the thermal conductivity and α_a and α_c represent the thermal expansion coefficients in the lateral and perpendicular directions of the crystal, respectively.

Table 5. Thermal properties of binary III-nitride materials and selected substrates.

Thermal parameter	GaN (Wz)	AlN (Wz)	InN (Wz)	Si	Sapphire
κ_{300} [$WK^{-1}m^{-1}$] [79,80,81,82]	130	285	38.5	148	42
α_a, α_c [10^{-6} K^{-1}] [83,81,84]	3.1, 2.8	2.9, 3.4	3.6, 2.6	2.6, 2.6	4.3, 3.2

2. TLM measurement

Transmission line measurement (TLM) is a technique used to determine the contact resistance between a metal and a semiconductor as well as the sheet resistance by forming an array of metal contacts separated from each other by varying distances (see Figure 62). The contacts are mesa isolated such that current only flows directly between the two contacts and not around them.

A four point probe setup is used in which two probes drive current through the spacing while another set of probes measure the associated voltage. Since the current travels from the first metal contact through the semiconductor-metal interface, through the sheet of semiconductor, through the second interface, and finally to the other contact metal, the total resistance measured

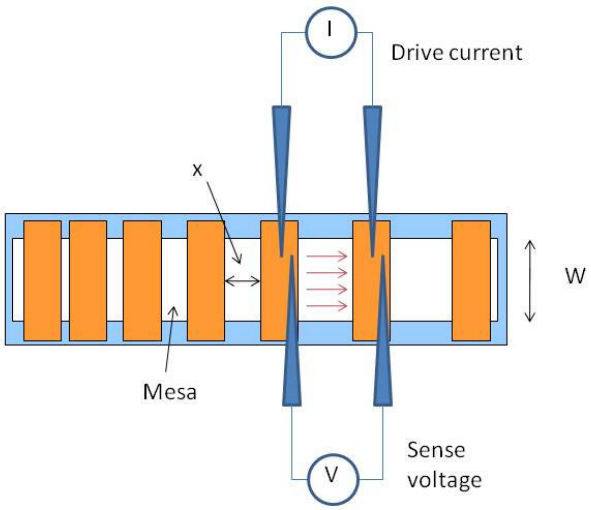

Figure 62. A TLM measurement setup including mesa isolated contact pads and a four point probe.

is a sum of the resistances through each of these media and is defined as the derivative of voltage with respect to current near 0 V. Since too many unknowns exist, the four point probe must be applied across several different contact pad spacing values (*x*) and the resistance values for each spacing must be plotted as in Figure 63. Since resistance varies linearly with distance, a linear fit can be applied to the resulting data points.

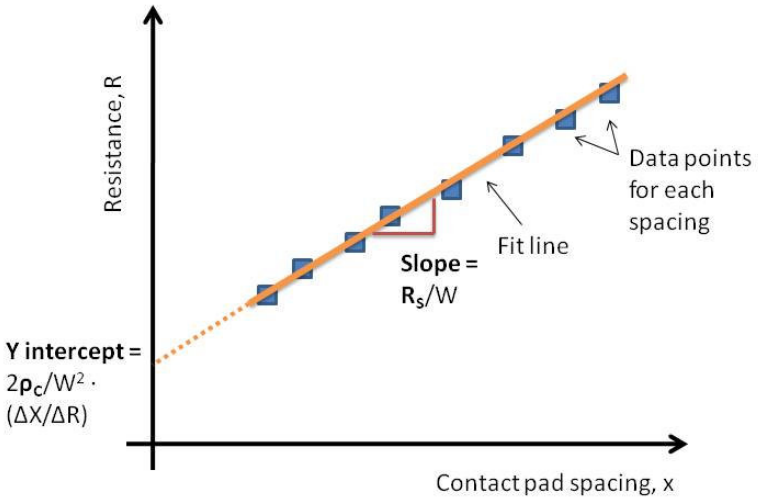

Figure 63. Resistance vs. contact pad spacing scatter plot for TLM measurements.

The slope of the resulting line is related to the sheet resistance by the following equation:

$$R_S = \frac{\Delta R}{\Delta X} W$$

Where W is the width of the mesa and the preceding term is the slope of the linearly fitted line. Furthermore, the transfer contact resistance can be obtained by finding the y-intercept of the fitted line, as follows:

$$R_C = \frac{Y_0}{2} W$$

Where Y_0 is the y-intercept of the fitted line. Lastly, the specific contact resistance is calculated by the following.

$$\rho_C = \frac{{R_C}^2}{L_t}$$

where L_t is the transfer length, taken by dividing the Y intercept by twice the slope of the fitted line.

3. Lattice relaxation, critical thickness, and dislocations

In situations where one material of a certain lattice constant ("*a*") must be grown on a material with a different lattice constant ("a_0"), a so-called lattice mismatch exists (See Figure 64). The in-plane lattice mismatch results in the presence of strain energy as the lattice of the epitaxial layer must expand or contract in the perpendicular direction in response to lateral stresses. For the case of $a>a_0$, the lattice constant perpendicular to the plane expands due to in-plane compressive stress. For the case of $a<a_0$, it contracts due to in-plane tensile stress.

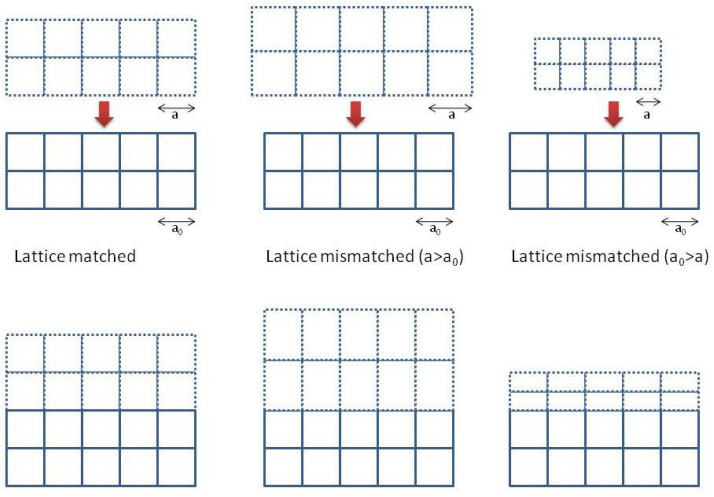

Figure 64. Resulting lattice formations for epitaxial growth of lattice-matched and mismatched materials.

When the strained film becomes thicker, the strain energy increases. Eventually, misfit dislocations form at the interface to reduce strain energy. The lattice then becomes “relaxed” by lowering the energy of the lattice by formation of dislocations or cracks. At this point, the “critical thickness,” h_c, is reached. Since dislocations and cracks can be detrimental to electrical performance, it is desirable to identify and to limit the growth thickness to below the critical thickness. The following formula allows for calculation of the critical thickness at a heterostructure:

$$h_c = \frac{a_0\left(1-\frac{\nu_{PR}}{4}\right)\left[\ln\left(\frac{h_c\sqrt{2}}{a_0}\right)+1\right]}{2\sqrt{2}\pi|f|(1+\nu_{PR})}$$

where f = (a_0-a)/a and v_{PR} is the Poisson ratio, which may be approximated to 1/3.

LIST OF SELECTED PUBLICATIONS

K. D. Matthews, X. Chen, D. Hao, W. J. Schaff, L. F. Eastman, " MBE growth and characterization of Mg-doped InGaN and InAlN," physica status solidi (c) **5**, 6 (2008) 1863-1865

X. Chen, K. D. Matthews, D. Hao, W. J. Schaff, L. F. Eastman, "Growth, fabrication, and characterization of InGaN solar cells,"physica status solidi (a) **205**, 5, (2008) 1103-1105

K. D. Matthews, M. G. Lamaitre, T. Kim, H. Chen, M. Shim, and J. Zuo, "Growth modes of carbon nanotubes on metal substrates" *J.Appl. Phys.* **200**, 100 (2006) 044309

K. Matthews, B. A. Cruden, B. Chen, M. Meyyappan, and L. Delzeit, "Plasma-Enhanced Chemical Vapor Deposition of Multiwalled Carbon Nanofibers" *J. Nanosci. Nanotech* **2**, 5 (2002)

C. V. Nguyen, L. Delzeit, K. Matthews, B. Chen, M. Meyyappan,"Purification Process for Vertically Aligned

Carbon Nanofibers" *J. Nanosci. Nanotech* **3**, 121 (2003)

K. D. Matthews, X. Chen, D. Hao, W. J. Schaff, L. F. Eastman, "A statistical leakage study of GaN solar cells and correlation of performance to grain size" *J. Appl. Phys* **108**, 7 (2010)

K. D. Matthews, J. Felbinger, Q. E. Diduck, I. Walsh, A. Conner, W. J. Schaff, L. F. Eastman, “Contacts to MBE Grown Ge Doped N-GaN” (pending publication)

K. D. Matthews*, J. Shi, D. Hao, W. J. Schaff, L.F. Eastman. “MBE Growth of GaN/Al_xGa_{1-x}N/AlN/GaN HEMTs on Sapphire for Higher Power Switching,” *Proceedings to the 2009 annual Workshop on Compound Semiconductors and Integrated Circuits*

X. Chen, K. D. Matthews, D. Hao, W. J. Schaff, L. F. Eastman, W. Walukiewicz, J. W. Ager, and K. M. Yu, “Growth and Characterization of Mg-doped III-Nitrides on Sapphire” *Proceedings to the 2008 Biannual Lester Eastman Conference*

REFERENCES

1. Robert Juza, Harry Hahn, *Zeitschrift fur anorganische und allgemeine Chemie* 239 282 (1938).
2. J. B. Parsons, *The preparation and study of the halides and a nitride of gallium* 16 (1931).
3. O. Ambacher, J. Smart, J.R. Shealy, N.G. Weimann, K. Chu, M. Murphy, W.J. Schaff, L.F. Eastman, R. Dimitrov, L. Wittmer, M. Stutzmann, W. Rieger, and J. Hilsenbeck, *J. Appl. Phys.,* **85**, 3222 (1999).
4. U.K. Mishra, P. Prikh, Y.F. Wu, *AlGaN/GaN HEMTs: An overview of device operation and applications,* (2002).
5. R. Quay, *Gallium Nitride Electronics,* pp. 10 (2008).
6. S. Bloom, G. Harbeke, E. Meier, I.B. Ortenburger, *Phys. Stat. Solidi,* **66**, 161-168 (1974).
7. R. Quay, *Gallium Nitride Electronics,* pp. 114 (2008).
8. W. Guter, J. Schöne, S. Philipps, M. Steiner, G. Siefer, A. Wekkeli, E. Welser, E. Oliva, A. Bett, F. Dimroth, *Appl. Phys. Lett.,* **94**, 223504 (2009).
9. C. Honsberg, O. Jani, A. Doolittle, E. Trybus, G. Namkoong, i. Ferguson, D. Nicole, A. Payne, *Proc. 19th Euro PV Sci. Eng. Conf.,* p. 15-20 (2004).
10. J. Wu, W. Walukiewicz, K.M. Yu, W. Shan, J.W. Ager, E.E. Haller, H. Lu, W. J. Schaff, W. K. Metzger, S. Kurtz, *J. Appl. Phys.* **94**, 6477 (2003).

11. K. D. Matthews, X. Chen, D. Hao, W.J. Schaff, and L.F. Eastman, *J. Appl. Phys.* **108**, 073105 (2010).
12. O. Jani, C. Honsberg, Y. Huang, J. Song, I. Ferguson, G. Namkoong, E. Trybus, A. Doolittle, S. Kurtz, *Conf. Record of the 2006 IEEE 4th World Conf. on PV Energy Conversion,* p.20-25.
13. I. Mahboob, T.D. Veal, C.F. McConville, H. Lu, W.J. Schaff, *Phys. Rev. Lett.,* **92**, 3, (2004).
14. P. Kozodoy, J.P. Ibbetson, H. Marchand, P.T. Fini, S. Keller, J.S. Speck, S.P. DenBaars, U.K. Mishra, *Appl. Phys. Lett.,* **73**, 975 (1998).
15. K. Leung, A.F. Wright, E.B. Stechel, *Appl. Phys. Lett.* **74,** 17, (1999).
16. S. M. Sze, *Physics of Semiconductor Devices,* J. Wiley and Sons, pp. 366, (1969).
17. C.H. Kuo, S.J. Chang, Y.K. Su, J.F. Chen, L.W. Wu, J.K. Sheu, C.H. Chen, G.C. Chi, *IEEE Elec. Dev. Lett.,* **23**, 5, (2002).
18. E. J. Miller, D. M. Schaadt, and E. T. Yu, P. Waltereit, C. Poblenz, and J. S. Speck, *Appl. Phys. Lett.* **82**, 8, 1293-1295 (2003)
19. E.F. Schubert, *Light-Emitting Diodes,* Cambridge Univ. Press (date unknown).
20. R. Quay, *Gallium Nitride Electronics,* pp. 56 (2008).
21. Y. Ando, Y. Okamoto, H. Miyamoto, N. Hayama, T. Nakayama, K. Kasahara, M. Kuzuhura, in *IEDM Technical Digest,* Washington DC, pp. 381-384, (2001).
22. P.Asbeck, E. Yu, S. Lau, G. Sullivan, J.V. Hove, J. Redwing, *Electron. Lett.* **33**, 1230 (1997).
23. S. Arulkumaran, M. Miyoschi, T. Egawa, H. Ishikawa, T. Jimbo, *IEEE Electron Dev. Lett.* **24**, 497 (2003).

24. P. Asbeck, E. Yu, S. Lau, W. Sun, X. Dang, C. Shi, *Sol. State Electron.* **44**, 211 (2000).
25. M. Aust, A. Sharma, A. Chau, A. Gutierrez-Aitken, *IEEE Intl. Microwave Symp. Digest,* Honolulu, pp. 809-812 (2007).
26. C. Bae, C. Krug, G. Lucovsky, A. Chakraborty, U. Mishra, *J. Appl. Phys.* **96**, 2674 (2003).
27. J. Shi, 1, Y. C. Choi, 1, M. Pophristic, M. Spencer, and L. F. Eastman, "High breakdown voltage AlGaN/GaN heterojunction field effect transistors on sapphire" *Phys. Stat. Sol. (c)* **5**, 6, pp. 2013–2015, (2008).
28. B. J. Baliga, *IEEE Trans. Electron Devices*, **43**, 11, pp. 1717–1731, (1996).
29. D. Visalli, M. Van Hove, J. Derluyn1, K. Cheng, S. Degroote, M. Leys, M. Germain, and G. Borghs, *Phys Stat. Sol. (c),* pp. 1– 4, (2009).
30. W. Saito*,* M. Kuraguchi, Y. Takada, K. Tsuda, I. Omura*,* and Tsuneo Ogura*, IEEE Trans. Elec. Dev,* **52**, pp. 106-111 1, (2005).
31. C. Poblenz, P. Waltereit, S. Rajan, S. Heikman, U.K. Mishra, J.S. Speck, *J. Vac. Sci. Technol. B* **22**, 1145 (2004).
32. R. Quay, *Gallium Nitride Electronics,* pp. 39 (2008).
33. G. Koley, M.G. Spencer, *Appl. Phys. Lett.,* **86,** 042107 (2005).
34. A. J. Sierakowski and L. F. Eastman, *J. Appl. Phys.* vol. 86, pp. 3398, 1999.
35. A. Sarua, Hangeng Ji, M. Kuball, M.J. Uren, T. Martin, K. P. Hilton, and R. S. Balmer, *CS MANTECH Conference,* Vancouver, British Columbia, Canada, pp. 179-182, (2006).

36. T. Beechem, S. Graham, S. P. Kearney, L. M. Phinney, and J. R. Serrano, *Rev. Sci. Instl,* **78,** 061301, pp. 1-9, (2007).
37. J. G. Felbinger, M.V.S. Chandra, Y. Sun, L. F. Estman, J. Wasserbauer, F. Faili, D. Babic, D. Francis, F. Ejeckam, *Electron Device Letters, IEEE*, **28,** 11, pp. 948-950, (2007).
38. W. Roesch, *Proc. IEEE GaAs IC Symp.,* pp. 61-64, (1988).
39. Y. Ohno, M. Akita, S. Kishimoto, K. Maezawa and T. Mizutani,, *Jpn. J. Appl. Phys.,* **41,** pp. L452-454, (2002).
40. V. Yu. Davydov, N. S. Averkiev, I. N. Goncharuk, D. K. Nelson, I. P. Nikitina, A. S. Polkovnikov, A. N. Smirnov, M. A. Jacobson, and O. K. Semchinova, *J. Appl. Phys.* **82,** pp. 5097-5102, (1997).
41. T. Ruf, J. Serrano, M. Cardona, P. Pavone, M. Pabst, M. Krisch, M. D'Astuto, T. Susuki, I. Grzegory, M. Leszczynski, *Phys. Rev. Lett.* **86**, 5, (2001).
42. H. Harima, H. Sakashita, S. Nakashima, *Mater. Sci. Forum 1998,* 1363, pp. 264-268.
43. L. Shi, F.A. Ponce, J. Menendez, *Appl. Phys. Lett.* **84**, 18 (2004).
44. Y. Chen, R. Coffie, Wen-Ben Luo, M. Wojtowicz, J. Smorchkova, B. Heying, *IEEE MTT-S,* pp-307-310, (2007).
45. K.W. Kim, V.V. Korotyeyev, V.A. Kochelap, A.A. Klimov, and D.L. Woolard*, J. Appl. Phys.,* 96, 11, pp. 6488-6491, (2004).
46. M. Tonouchi, *N. Photon.,* 1, pp. 97-105, (2007).
47. D. Pavlidis*, 12th GAAS Symp., Amsterdam* pp.551-554, 2004.
48. A. Dyson and B.K. Ridley, *J. Appl. Phys.,* 104, 113709, pp. 1-6, (2008).

49. H,. Kromer, *Phys. Rev.,* **109**, 1856 (1958).

50. L. Esaki and R. Tsu, *IBM J. Res Dev,* **14**, 61 (1970).

51. B.K. Ridley, W.J. Schaff, and L.F. Eastman, *J. Appl. Phys.,* **97**, pp. 094503-094509, (2005).

52. M. Wraback, H. Shen, J.C. Carrano, C.J. Collins, J.C. Campbell, R.D. Dupuis, M.J. Schurman, and I.T. Ferguson, *Appl. Phys. Lett.,* **79**, 9, pp. 1303-1305, (2001).

53. J. Kolnik, I.H. Oguzman, K.F. Brennan, R. Wang, P.P. Ruden, Y. Wang, *J. Appl. Phys.* **78(2)**, 1033-1038 (1995).

54. J.D. Albrecht, R.P. Wang, P.P. Ruden, M. Farahmand, K.F. Brennan, *J. Appl. Phys.* **83(9)** 4777-4781, (1998).

55. B. Aslan and L.F. Eastman, “Dynamics of GaN based ballistic electron acceleration negative conductivity (BEAN) diodes at THz frequencies,” (submitted for publication).

56. K.D. Matthews, I. Walsh, Q. Diduck, A. Conner, J. Felbinger, W.J. Schaff, L.F. Eastman, “N-type Ohmic Contacts to MBE Grown Ge Doped GaN for Terahertz Emitters,” (submitted for publication)

57. S.M. Sze, *Modern Semiconductor Device Physics,* New York: Wiley, (1998).

58. K. Köhler, J. Wiegert, H.P. Menner, M. Maier, and L. Kirste, *J. Appl. Phys.,* **103**, 023706, pp. 1-5, (2008).

59. P.R. Hageman, W.J. Schaff, J. Janinski, Z. Liliental-Weber, *J. Cryst. Growth,* **267**, 123-128 (2004).

60. B. Aslan, L.F. Eastman, Q. Diduck, *Int. J. High Speed Electron. Sys.,* **19**, 1, pp. 1-6 (2009).

61. L. Wang, F. M. Mohammed, I. Adesida, *J. Appl. Phys.,* **101**, 013702, pp. 1-11, (2007).
62. J. Jeon, T. Seong, H. Kim, K. Kim*, Appl. Phys. Lett.,* **94**, 0242102, pp. 1-3, (2009).
63. S. Mohammad, *J. Appl. Phys.,* **95**, 12, pp. 7940-7953, (2004).
64. Y. Sun, X. Chen, L.F. Eastman*, J. Appl. Phys.,* **98**, 053701, pp. 1-5, (2005).
65. V. Kumar, L. Zhou, D. Selvanathan, and I. Adesida*, J. Appl. Phys.,* **92**, 3, pp. 1712-1714, (2002).
66. D. Selvanathan, L. Zhou, V. Kumar, I. Adesida, and N. Finnegan*, J. Elec. Mat.,* **32**, 5, pp. 335-340, (2003).
67. B. Foutz, S. O'Leary, M. Shur, L. Eastman, *J. Appl. Phys.,* **85**, 7727 (1999).
68. A. Chakraborty, B. Haskell, S. Keller, J. Speck, S. Denbaars, S. Nakamura, U. Mishra, *Jpn. J. Appl. Phys.,* **44**, L173 (2005).
69. T. Ruemenapp, D. Peier, in *11th Int. Symp. High-Voltage Engin.,* London, pp. 4.373-4.376, (1999)
70. M. Levinshtein, S. Rumyantsev, M. Shur (eds.), *GaN, AlN, InN, BN, SiC, SiGe: Properties of Advanced Semiconductor Materials* (Wiley, New York, 2001).
71. M. Drechsler, D. Hofmann, B. Meyer, T. Detchprohm, H. Amano, I. Akasaki, *Jpn. J. Appl. Phys.,* **34**, L1178 (1995).
72. S. O'Leary, B. Foutz, M. Shur, U. Bhapkar, L. Eastman, *Solid-State Comm.,* **105**, 21 (1998).
73. S. Fu, Y. Chen, *Appl. Phys. Lett.* **85**, 1523, (2004).

74. F. Bernardini, V. Fiorentini, D. Vanderbilt, *Phys. Rev. B* **56**, R10024 (1997).
75. K. Brennan, E. Bellotti, M. Farahmand, J. Haralson, P. Ruden, J. Albrecht, A. Sutandi, *Sol. State Electron.,***44**, 195, (2000).
76. Y. Lin, Q. Ker, C. Ho, H. Chang, F. Chien, *J. Appl. Phys.,* **94**, 1819 (2003).
77. J. Orton, C. Foxon, in *Properties, Processing and Applications of GaN Nitride and Related Semiconductors,* No. 23 in EMIS Data reviews Series, ed. By J. Edgar et al. (IEE INSPEC, London, 1999), Sect. 8.4, pp.294-299.
78. J. Orton, C. Foxon, in *Properties, Processing and Applications of GaN Nitride and Related Semiconductors,* No. 23 in EMIS Data reviews Series, ed. By J. Edgar et al. (IEE INSPEC, London, 1999), Sect. 8.5, pp. 300-305.
79. D. Florescu, V. Asnin, F. Pollack, *Comp. Semicond.* **7**, 62, (2001).
80. G. Slack, R. Tanzilli, R. Phol, J. Vandersand, *J. Phys. Chem. Solids,* **48**, 641, (1987).
81. S. Krukowski, M. Leszczynski, S. Porowski, in *Properties, Processing and Applications of GaN Nitride and Related Semiconductors,* No. 23 in EMIS Data reviews series, ed. By J. Edgar et al. (IEE INSPEC, London, 1999), Sect. 1.4, pp.21-28.
82. S. Selberherr, *Analysis and Simulation of Semiconductor Devices* (Springer, Wien New York, 1984).
83. J. Edgar, in *Properties of Group III Nitrides,* No. 11 in EMIS Data reviews Series, ed. By J. Edgar (IEE INSPEC, London, 1994), Sect. 1.2, pp. 7-21.

84. M. Leszczynski, T. Suski, H. Teisseyre, P. Perlin, I. Grzegory, J. Jun, S. Porowski, T. Moustakas, J. Appl. Phys., **76**, 4909, (1994).